Imperial College London

Royal School of Mines

Department of Earth Science and Engineering

The behavior of rising bubbles covered by particles

by

Peipei Wang

A Thesis Submitted for the Degree of

Doctor of Philosophy and Diploma of Imperial College London

October 2019

Abstract

Bubble-particle aggregates play a dominant role in separation processes such as froth flotation. Previous studies on individual rising bubble motion have mainly focused on gas-liquid two-phase systems and there has been no systematic investigation on the influence of particles on the rising behavior of particle-laden bubbles.

In this project, clear visualization of the behavior of bubble-particle aggregates is achieved by using capillaries to generate bubbles of controlled size in a transparent experimental rig, which are released after attachment of particles is achieved. The pendant drop model was used and fitted to the edge points of the bubbles to calculate their particle surface coverage. High-speed photography and image analysis techniques were used to record and analyze the hydrodynamics of rising bubbles in terms of velocity and aspect ratio. The influence of particle coverage and particle size on the behavior of rising bubbles was studied. In addition, the buoyancy force, drag force as well as the mass force on the particles and bubbles were calculated and interpreted.

Results show that with the increase of particle coverage or attached particle size, the aspect ratio oscillation patterns of the rising bubbles are similar and the high frequency oscillation periods do not change significantly. This indicates that the capillary wave caused by surface tension does not change, it is the hydrodynamic force that differentiates bubble motion. With the increase of particle size or coverage, the rising bubbles show a lower velocity as well as a damped aspect ratio oscillation. Particles attached on the bubbles decrease the bubble acceleration, and this acceleration is

inversely correlated to the bubble aspect ratio and its change. The highest rising velocities correspond to the lowest aspect ratios and vice versa, independently of the particle size or coverage. A particle drag modification factor, which quantifies the drag influence of particles on bubble velocity, was identified from force analysis. A modified drag coefficient for uncoated and particle-laden bubbles was introduced, which allows, for the first time, to predict the behavior of rising particle-laden bubbles in gas-liquid-solid systems.

The results and interpretation produced a quantitative description of the behavior of rising particle-laden bubbles and the development of correlations that can be used to inform the modelling of industrial applications such as pulp phase phenomena in froth flotation.

Declaration of Originality

The work submitted in this thesis is my own, and that all else has been appropriately referenced.

Peipei Wang

Copyright Declaration

Peipei Wang

Acknowledgements

First of all, I would like to express my sincere appreciation to both of my supervisors, Dr. Pablo Brito-Parada and Prof. Jan Cilliers, who took me on as their student four years ago and opened a new world for me.

My gratitude goes to Pablo, who creates an intellectually stimulating and relaxed atmosphere for research and discussions, and continuously encourages me to take every chance to learn and improve. When I was harassed by setbacks of my research, he was always there to give firm support and invaluable feedback. He is always kind to discuss and advice, and contributes greatly to the quality of this work.

I want to express my deepest thanks to Jan, who always willing to guide me despite his busy schedule, inspire me, encourage me and help me to explore my potential. I admire his positive values, rigorous attitude and analytical mind, and treasure what I learnt from him.

Thanks are due to Prof. Stephen Neethling, who gives valuable comments on my research and carefully reviews my progress during the PhD, and most importantly, his insights and rigorous thinking helped me obtain a better understanding of modelling and fluid dynamics.

I can still recall clearly when Pablo, Jan and Stephen discussed with me together about my paper for every tiny bit of improvement and tried their best to help me polish it. I regard this as a priceless treasure that will continue inspire my passion in academia, and I sincerely grateful to have such kind of mentors who always encourage younger generations and nurture their love of research.

I appreciate the assistance and support from Dr. Kathryn Hadler, who gives me kind advice and useful suggestions for my research. Moreover, her enthusiasm always inspires me deeply.

I would like to express my gratitude to Graham Nash and Gary Jones for their contributions to the experimental setup, who always willing to discuss with me and provide solutions for the improvement of the facilities.

In particular, I would like to thank Francisco Reyes for his help to extend my knowledge on programming, who always patiently answering my questions. Thanks are also due to my other group members, who are currently or were previously studying or working together with me: Dr. Dennis Vega-Garcia, Dr. Alexander Norori-McCormac, Dr. Liping Cai, Dr. Angus Morrison, Dr. Gaurav Bhutani, Isobel Mackay, Hao Wang, Joshua N Rasera, etc. for their constant spiritual encouragement. I am very happy to be part of this diverse and harmonious group, and I have also been inspired by their cool research.

I appreciate the help from Chinese friends at Imperial College London past and present: Dr. Pan Yang, Dr. Bowen Song, Dr. Wenzhuo Cao, Dr. Jinyue Liu, Chenyang Wu, Kailing Ng, etc. I cherish our friendship and the time we spent together.

I would like to thank the President's PhD Scholarship from Imperial College London for funding my PhD study. I also thank IOM3 (The Institute of Materials, Minerals and Mining) for their financial support for the purchase of some of the equipment and also the travel grant to attend a conference in Saint Petersburg. Thanks are also due to SCI-RSC Rideal Trust for the travel grant.

Finally, my deepest gratitude are due to my family for years of continuous love, support and sacrifices.

Table of Contents

Abstract ..... **i**

Declaration of Originality ..... **iii**

Copyright Declaration ..... **iv**

Acknowledgements ..... **v**

Table of Contents ..... **vii**

List of Figures ..... **x**

List of Tables ..... **xiv**

Chapter 1 Introduction **1**

1.1 Motivation 1

1.2 Thesis overview 3

Chapter 2 Literature review **6**

2.1 Froth flotation 6

2.1.1 Background of froth flotation 6

2.1.2 Influence of particles and bubbles on flotation performance 10

2.2 The use of capillary pinned bubbles 17

2.2.1 Capillary pinned bubbles to study coalescence 17

2.2.2 Capillary pinned bubbles to study induction/attachment time 24

2.2.3 Capillary pinned bubbles to study attachment and detachment 26

2.3 Motion of rising individual bubbles 29

2.3.1 Characterization of rising air bubbles 29

2.3.2 Influence of reagents and temperature on bubble motion 31

2.3.3 Influence of bubble size and particles on bubble motion 33

2.4 Force analysis and prediction of rising bubbles 36

2.4.1 Forces and drag coefficient 36

2.4.2 Prediction of bubble motion 39

2.5 Summary 44

Chapter 3 Methodology 46

3.1 Materials 46

3.2 Setup 48

3.3 Experimental procedure 48

3.3.1 Assessing the influence of particle coverage 49

3.3.2 Assessing the influence of particle size 51

Chapter 4 Image processing method for uncoated bubbles and particle-laden bubbles 52

4.1 Pendant drop method to calculate the particle coverage 52

4.2 Sessile drop method to calculate the particle coverage 55

4.3 Bubble velocity and aspect ratio calculation 59

4.4 Comparing the behavior of uncoated bubbles with particle-laden bubbles 61

4.4.1 Velocity and aspect ratio (change) of uncoated bubbles and particle-laden bubbles 61

4.4.2 Comparing the acceleration of uncoated bubbles with particle-laden bubbles 64

4.5 Summary 68

Chapter 5 Influence of surface coverage of particles on rising particle-laden bubbles 70

5.1 The reliability of experimental data 70

5.2 Influence of particle coverage on the velocity and aspect ratio change of rising particle-laden bubbles 73

5.3 Oscillation period analysis 76

5.4 Force calculation and analysis 78

5.5 The drag modification factor and modified drag coefficient 82

5.6 Summary 85

Chapter 6 Influence of particle size on rising particle-laden bubbles 87

6.1 Particle coverage as a function of time in the attachment experiments 87

6.2 The influence of particle size on the velocity and aspect ratio change of rising particle-laden bubbles 87

6.3 Oscillation period analysis 92

6.4 The drag modification factor analysis 94

6.5 The modified drag coefficient and forces analysis of particle-laden bubbles 97

6.6 Summary 101

Chapter 7 Conclusions and recommendations for future research 102

7.1 Conclusions 102

7.2 Recommendations for future research 103

References 105

Appendices 125

Appendix A Influence of TTAB concentration on the rising behavior of particle-laden bubbles 125

Appendix B Evaluating the performance of chalcopyrite collectors using the sessile drop method on individual bubbles 126

Appendix C List of Publications 135

List of Figures

Figure 2.1. Schematic diagram of a mechanical flotation cell. The impeller is shown to agitate the pulp and generate bubbles from air injected from the top. Hydrophobic particles attach to bubbles in the pulp phase and the particle-bubble aggregates ascend to the top froth zone, which finally overflows as concentrate, while gangue particles go to the tailings at the bottom [11]. 7

Figure 2.2. Fitting of calculation results to the experimental data points for the oscillation of the projected area of a coalesced bubble [82]. 20

Figure 2.3. Photo sequences of coalescence for (a) both uncoated bubbles, (b) coated and uncoated bubbles, and (c) both coated bubbles. Time interval between frames was about 0.5ms [70]. 22

Figure 2.4. Schematic of the CSIRO Milli-Timer device [97]. 25

Figure 2.5. Schematic view of the integrated thin film drainage apparatus: (a) chamber configuration; (b) a piezoelectric bimorph used to measure the charge generated on the bimorph cantilever under an external force [98]. 26

Figure 2.6. A schematic diagram of the apparatus using loudspeaker to investigate the detachment of particles from bubbles [71]. 29

Figure 3.1. (a) Particle size distribution and (b) cumulative volume fractions of the samples used in the experiments. The legends correspond to the $d90$ of each sample. 48

Figure 3.2. Experimental configuration to investigate the behavior of a rising air bubble, showing the setup including the cameras and light arrangement. 49

Figure 4.1. Schematic for the derivation of the Young-Laplace equation to obtain a fit to a bubble edge. 53

Figure 4.2. Images rotated for edge detection of a bubble (a) before and (b) after being coated with particles. The red line shows the detected edge points. 55

Figure 4.3. Curve fitting to the uncoated and coated bubble edge points: (a) detection of the point where particles begin to coat the bubble, marked here with a blue circle; (b) fitting after the particle diameter is reduced. 56

Figure 4.4. Schematic for the derivation of the Young-Laplace equation to obtain a fit to a bubble edge. 57

Figure 4.5. Images for edge detection of a bubble (a) before and (b) after being coated with particles. The red line shows the detected edge points. 58

Figure 4.6. Curve fitting to the uncoated and coated bubble edge points; the solid lines correspond to the uncoated bubble edge from the image (red) and the model (black) and the dotted lines to the coated bubble edge from the image (red) and the model (black). 59

Figure 4.7. Image analysis procedure: (a) bubble image, (b) image after threshold applied, (c) edge detected and diameters a and b that are used to determine the aspect ratio. 60

Figure 4.8. Evaluation of the aspect ratio of (a) uncoated bubble and (b) coated bubble with time. 63

Figure 4.9. Evaluation of the velocity of uncoated bubble and coated bubble with time. 64

Figure 4.10. Velocity vs. Aspect ratio of the uncoated bubble and coated bubble. .. 65

Figure 4.11. Acceleration of the uncoated and coated bubbles: (a) raw data, (b) data processed with a moving-average filter (window size 6). 66

Figure 4.12. Acceleration and aspect ratio of the (a) uncoated bubble and (b) coated bubble. Original data of acceleration processed with a moving-average filter (window size 6). 67

Figure 4.13. Acceleration and aspect ratio change of the (a) uncoated bubble and (b) coated bubble. Original data processed with a moving-average filter (window size 6). 69

Figure 5.1. (a) Aspect ratio and (b) velocity of uncoated bubbles after release (from three measurements). 71

Figure 5.2. (a) Aspect ratio and (b) velocity of coated bubbles after release (from three measurements). 72

Figure 5.3. Different fractions of bubbles covered by particles. 73

Figure 5.4. Aspect ratio as a function of different fractions of bubbles covered by particles. 74

Figure 5.5. Velocity as a function of different fractions of bubbles covered by particles. 76

Figure 5.6. Particle influence on the drag coefficient according to different fractions of bubbles covered by particles. 83

Figure 5.7. Modified drag coefficient compared with the drag coefficient calculated from the experimental data for an uncoated bubble as a function of the time. 84

Figure 5.8. (a) Modified drag coefficient compared with the drag coefficient predicted from Schiller-Naumann for an uncoated bubble as a function of the Reynolds number. (b) Modified drag coefficients of the uncoated bubble and bubbles loaded at different levels of particle coverage as a function of the Reynolds number. 86

Figure 6.1. Particle coverage on capillary pinned bubbles as a function of time for particles of size $d90$=156 μm. The data are shown with 95% confidence intervals. 88

Figure 6.2. Aspect ratio of rising bubbles (initially half coated) as a function of particle size. 90

Figure 6.3. Velocity of rising bubbles (initially half coated) as a function of particle size. 90

Figure 6.4. Aspect ratio of rising bubbles (initially fully coated) as a function of particle size. 91

Figure 6.5. Velocity of rising bubbles (initially fully coated) as a function of particle size. 92

Figure 6.6. Times when aspect ratio peaks occur for rising bubbles (initially half coated). 93

Figure 6.7. Times when aspect ratio peaks occur for rising bubbles (initially fully coated). 94

Figure 6.8. The particle drag modification factors for rising particle-laden bubbles as a function of particle size. For initially half and fully coated bubbles, 95% confidence intervals are shown. 97

Figure 6.9. The modified drag coefficient of particle-laden bubbles with different sizes of particles as a function of the Reynolds number (initially fully coated). 98

Figure 6.10. Forces acting on rising particle-laden bubbles which are initially fully coated (a) Particle size d_{90}=64μm. (b) Particle size d_{90}=266μm. 100

List of Tables

Table 2.1. The influence of particles properties on the performance of froth flotation. 13

Table 3.1. The Sauter-mean diameter ($d32$), $d50$ and $d90$ for the samples used in the experiments. 46

Table 5.1. Average oscillation period of bubbles with different levels of particle coverage over the first five oscillations (95% confidence interval included). 77

Table 6.1. Average time needed for the bubbles to be fully coated with particles (95% confidence interval included). 89

Table 6.2. Particles drag modification factors for initially half coated bubbles (95% confidence interval included). 96

Table 6.3. Particle drag modification factors for initially fully coated bubbles (95% confidence interval included). 96

Chapter 1 Introduction

1.1 Motivation

With ever-increasing demand from modern society and exhaustion of rich mineral deposits, the mining industry is facing many challenges. At the same time, the requirements of social and environmental responsibility increase, which compels mining companies and engineers to seek innovative ways to enhance the mineral production and minimize the environmental impacts to maintain sustainable development. To meet these demands, understanding minerals properties and their processing is of paramount importance.

Mineral processing is a major division in the science of extractive metallurgy, aiming to extract metals from their ores, refine them and prepare them for use. As of today, the recovery of minerals is subjected to severe conditions due to the difficult-to-treat ores, which means low grade and finely dissemination of valuable minerals in the ores. It is therefore of crucial importance to develop innovative approaches to better understand fundamental aspects of the processes used to concentrate minerals in order to increase recoveries. There are a number of ways to recover valuable minerals, and the method chosen depends on the physical and surface properties of the valuable mineral and the gangue.

As a widely used physicochemical method in mineral processing, froth flotation has contributed largely to the expansion of the raw materials industry. The principle of froth flotation is to separate minerals from ore by taking advantage of differences in the wetting properties of different minerals. Nonpolar molecules in the substances that

repel the water molecules are said to be hydrophobic; molecules forming ionic or a hydrogen bond with the water molecule are said to be hydrophilic. Differences in hydrophobicity between valuable minerals and gangue are increased with the aid of surfactants. Air bubbles are generated in the flotation cell, collecting particles while ascending from the pulp phase to the top, the bubble-particle aggregates form a froth phase, which finally overflows as a mineral-rich concentrate. The behavior of bubble-particle aggregates plays a dominant role in this separation process.

In gas-liquid-solid flotation systems, the presence of particles influences the behavior of a rising bubble, particularly if the particles are attached to the bubble's surface. Due to the opaque and highly dynamic nature of the three-phase slurries, it is impossible to directly visualize the behavior of a rising particle-laden bubble. Capillaries can be used to generate bubbles of controlled bubble size in a transparent experimental rig, which allows clear visualization of bubble behavior. Such an experimental setup can therefore provide valuable information on the rising behavior of particle-laden bubbles.

Apart from froth flotation, the behavior of rising air bubbles is a critical factor in determining the efficiency of a wide range of industrial applications such as oil and gas extraction [1,2], wastewater treatment [3], plastic recycling [4] as well as microalgae harvest [5]. Studies on individual bubble behavior are mainly focused on two-phase liquid-gas systems. The behavior of particle-laden bubbles, however, has been only studied for fully coated bubbles [6] or bubbles partially coated with particles focusing on their bounce back from the liquid-air interface [7]. Little work has been done to systematically investigate the influence of different surface coverages of particles on bubbles, let alone the influence of the size of the particles attached to the bubbles. In froth flotation, the velocity, size and shape changes of bubbles can directly

influence the interaction of the particles attached to their surface and thus determine the final flotation performance. Investigations into bubble loading and bubble-particle aggregate behavior are of great importance ─ these are factors that strongly influence flotation recovery but for which very little fundamental work has been carried out.

This work will develop a novel setup to observe the initial behavior of bubbles after they are detached from a capillary tip. A micro syringe pump will be used to generate bubbles of controlled sizes. High-speed photography will be introduced to track bubble motion. The pendant drop method will be used to fit the equation model to the edge points of the bubbles to calculate their particle surface coverage. The influential factors on the behavior of particle-laden bubbles, including the particle coverage and particle size, will then be investigated. In addition, the forces exerted on these bubbles will be calculated and the relationship between the velocity of a particle-laden bubble and its aspect ratio will be analyzed. A modified drag coefficient model will be obtained for rising particle-laden bubbles. These findings will provide valuable insight into the behavior of particle-laden bubbles, which is essential to inform the modeling of industrially relevant processes where these bubble-particle aggregates play a key role. The contribution of such studies to, in turn, improve flotation technology, presents an economic incentive for this type of research.

1.2 Thesis overview

This thesis is laid out as follows:

Chapter 1 provides a general introduction of the background of mineral processing and froth flotation, and outlines the importance of the motion of bubble-particle aggregates.

Chapter 2 presents an extensive literature review, from froth flotation to individual bubble scale phenomena. Capillary pinned bubbles and then released bubble behavior are reviewed, followed by a summary of the force analysis and different models that developed to predict bubble motion. Knowledge gaps, which are to be addressed in the main body of the thesis, are identified.

Chapter 3 outlines the experimental methodology used in this study. The materials, the experimental setup as well as the experimental procedure associated with different particle coverages and particles sizes are introduced.

Chapter 4 focuses on the techniques involved in characterizing the bubble behavior and compares the results of rising bubbles with and without particles. The experimental results of bubble velocity and aspect ratio with different TTAB concentrations are outlined in Appendix A. The pendant drop method is developed for the calculation of the particle coverage. The sessile drop method, on the other hand, is also applied for the characterization of the chalcopyrite particle coverage on capillary pinned bubbles, the result of which is presented in Appendix B. The velocity, acceleration, aspect ratio as well as its change are compared with regard to uncoated bubbles and particle-laden bubbles.

Chapter 5 is devoted to investigating the influence of surface coverage of particles on the behavior of rising bubbles. Based on the results of aspect ratio, the oscillation periods are analyzed and the main difference, i.e., the hydrodynamic force, is identified. The traditional Schiller-Naumann drag coefficient model has been modified to fit the calculated bubble velocity to the experimental results. A drag modification factor is identified to quantify the drag influence of particles on bubble velocity, and a modified drag coefficient for uncoated and particle-laden bubbles is introduced for the first time.

In Chapter 6, the rising behavior of bubbles, initially half and fully coated with glass beads of various sizes, is investigated. Particle attachment tests are conducted based on different stirring times and particle sizes. In addition, the oscillation period, the acting forces, the particle drag modification factor and the modified drag coefficient are calculated and interpreted.

Finally, Chapter 7 summarizes the main findings from the research presented and makes recommendations for future work. Two published papers based on this work are presented in Appendix C.

Chapter 2 Literature review

2.1 Froth flotation

Froth flotation was commercially introduced in the early 20th century and now it has been widely applied to extract valuable minerals from ores. Apart from mineral processing [8], the froth flotation process keeps being adapted to more industrial applications like deinking of wastepaper [9], microalgae harvest [5] as well as industrial wastewater treatment [10].

2.1.1 Background of froth flotation

Froth flotation is a process for selectively separating hydrophobic material from hydrophilic one. Therefore, the basics of froth flotation rely on natural or acquired hydrophobicity of particles by adding flotation reagents such as fatty acids and oils, making particles easily aggregate together at the air-liquid interface.

To achieve a successful separation, a series of sub-processes in the pulp phase need to be guaranteed. Firstly, a chemical environment should be met to ensure that at least one kind of minerals is more prone to adhere to the air bubble. Secondly, adequate turbulence is required for minerals and bubbles to frequently and vigorously collide so that attachment is obtained.

After the bubble-particle aggregates are formed, they ascend from the pulp phase to the top and then form a mineralized froth (froth phase) above, which eventually overflows as concentrate. A schematic diagram of a mechanical flotation cell is shown in Figure 2.1.

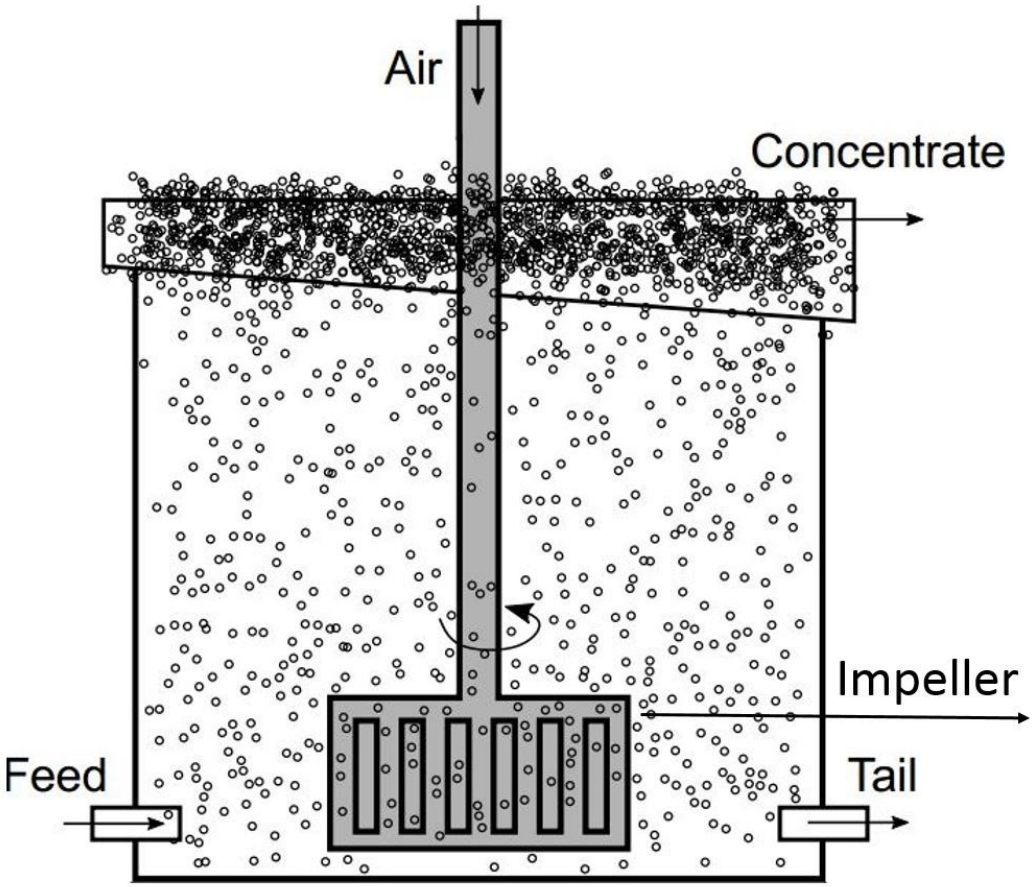

Figure 2.1. Schematic diagram of a mechanical flotation cell. The impeller agitates the pulp and generates bubbles from air injected from the top. Hydrophobic particles are attached to bubbles in the pulp phase and the particle-bubble aggregates ascend to the top, forming a froth zone, which finally overflows to the concentrate, while gangue particles go to the tailings at the bottom [11].

In the froth phase, a meta-stable condition is necessary to obtain maximum recovery. An unstable froth continuously breaks down due to rapid liquid drainage within the Plateau border channels or due to high superficial gas velocities; such a froth is therefore not able to efficiently transport particles to the concentrate. An over-stable froth, on the other hand, leads to a low-grade product due to a high liquid content and the subsequent mechanical entrainment and entrapment of gangue minerals [12]. Entrainment and physical entrapment always occur in addition to true flotation (i.e.

attachment). Entrainment is the process by which particles enter the froth at the interface via the liquid channels between bubbles and are then transported with the froth to the concentrate [13]. Physical entrapment refers to particles that are trapped in the Plateau border vertices (due to their larger size in comparison to the thinning liquid channels) and that report to the froth phase [8].

Bubble-particle aggregates play a dominant role in the flotation performance. The bubble-particle collection or capture efficiency E [14] can be defined as:

$$E = E_C \times E_A \times E_S \,, \tag{2.1}$$

where E_C is the bubble-particle collision efficiency, E_A is the attachment efficiency and $E_S$is the stability efficiency, every one of which is independent of each other.

In the process of bubble-particle attachment, three fundamental steps [15–18] are normally considered: first of all, the approach of bubble and particle towards each other and the liquid film between them drains to a critical thickness. Secondly, the rupture of the film rendering a three phase contact (TPC) between air, solid and liquid. Finally, the propagation of the three-phase contact line and formation of a stable attachment between the air bubble and the particle. The time required for these sub-processes is known as induction time t_{ind} or attachment time t_{att}, which is the time required for the film thinning between particle and bubble and can be expressed as:

$$t_{ind} = t_{att} = t_d + t_r + t_{tpc} \,, \tag{2.2}$$

where t_d represents the time for liquid drainage to the critical thickness, t_r denotes the time for the film rupture to establish the TPC, and t_{tpc} is the time for the TPC expansion to form a stable wetting line. To ensure a successful attachment of a particle

to an air bubble, the prerequisite is that the contact time between the bubble and the particle has to be longer than the induction time [19].

Flotation efficiency can be enhanced by increasing particle attachment and decreasing its detachment. After the attachment occurred, the bubble-particle aggregate goes through regions of different turbulences, and particles have to overcome these barriers so as to be carried by the bubbles to the top and finally overflow to the concentrate. Bubble-particle detachment measurement and models are decomposed into three categories: force balance analysis [20,21]; energy balance analysis [14,22,23] and empirical analysis of particle size compared to the maximum floatable particle size [24,25].

In flotation, hydrodynamics works in different ways according to different particle sizes; particles either too coarse or too fine are often not recovered during the flotation process or are recovered poorly. Initially, the flotation recovery increases with particle size monotonically and then it reaches a plateau, afterwards, the recovery decreases with a further increase in particle size [26,27]. For fine particles, the flotation limitation is dictated by the energy that required to rupture the intervening thin liquid film between the particle and bubble, which also means low collision rates between fine particles and bubbles are the key reasons for the low recovery [28]. Although all the collision models predict that the particle bubble collision efficiency increases with particle size [29], it is not always beneficial to float with coarse particles. Since for coarse particles [27], their detachment rate from bubbles increases. The turbulent motion of the liquid is the main reason for the low recovery of coarse particles, hence the stability of the bubble-particle aggregates control the maximum floatable particle size.

2.1.2 Influence of particles and bubbles on flotation performance

The separation of valuable minerals by froth flotation is strongly dependent on the particle size. Bubbles coated with particles are quite sensitive to the surrounding fluid environment, and detachment occurs when the attachment of particles is not strong enough to avoid the interruption force of the fluid flow, which becomes more noticeable for larger particles. Flotation recovery of both fine and coarse particles is usually remarkably low, and the effective particle size varies with the mineral properties, as well as the chemical and physical environment of the system.

For typical particle size and contact angle encountered in flotation, the bubble size exerts minor influence on the detachment, while the turbulent eddies have a strong impact on the bubble-particle collision and the detachment process [25]. The mean centrifugal acceleration of turbulent eddies was found to be a controlling parameter of the upper size limit of particles to be recovered by flotation in the mechanical cells [25]. Koh and Smith [30] have investigated the effect of both stirring speed and induction time on flotation, they have found that for a given particle size, an optimum stirring speed could yield a good compromise between attachment and detachment rates in the flotation cell; while for less hydrophobic particles, a lower stirring speed was beneficial in having a longer contact time due to the longer induction time needed for attachment.

Rahman et al. [31] have investigated the influence of collector concentration, froth depth, air flow rate, as well as the ratio of fine to coarse particles in the feed on both the collection and the froth zone. Results have shown that the froth was destabilized at high collector concentrations, leading to a significant reduction in the recovery of coarse particles in the froth zone; the froth zone acted as a significant barrier to recover

coarse particles in the concentrate. They also found that the fine particle obtained much higher overall recovery than that for coarser particles since even less favorable conditions were enough to obtain optimum flotation performance.

Other studies have investigated the effect of particle properties on froth stability. A measure of froth stability, the dynamic froth stability, is the proportionality rate of the height of the froth to the gas flow rate in the system and it has been used as an important parameter to describe the average lifetime of a bubble in the froth [32,33]. It has been found that when flotation was operated at coarser particle size distributions, the presence of fine particles in the system could, to some extent, improve both the dynamic froth stability and the flotation performance [34]. However, findings showed that if the ratio of fines was too high, even the improvement in dynamic froth stability would not necessarily guarantee the enhancement of the flotation performance.

Another measure of froth stability is the air recovery, or the fraction of air fed into a flotation cell that overflows as unburst bubbles. The effects of particle size distribution on the air recovery were studied by Norori-McCormac et al. in a silica system using a continuous steady-state laboratory flotation cell [35]. It was demonstrated that there was an optimal air flow rate for each particle size distribution, therefore the change in particle size distribution in the feed to flotation cells required a correspondingly variation in air flow rate in order to maximize mineral recovery. Air recovery has also been proposed to be a good indicator to optimize mineral flotation [36].

Apart from particle size, flotation is also very sensitive to particle shape characteristics since these parameters will influence both the physical and surface properties of particles which will finally influence the recovery of valuable minerals [37]. The influence of roughness and shape of particles has been reported in several

studies [38,39], it was shown that particles with higher roughness and sharp edge were easier to be collected.

The hydrophobic characteristic of mineral surfaces is paramount for the extraction of valuable minerals and this wetting characteristic can be reflected by the contact angle value, therefore, there is a close relationship between contact angle and the floatability of minerals [40,41]. The influence of both particle size and contact angle on the chalcopyrite flotation has been studied by Muganda et al. [42]. It was found that within any particle size fraction, both the maximum recovery and rate constant were increased with an increase in the advancing contact angle. The flotation rate increased rapidly with an increase in the contact angle for particles in intermediate size fractions; while for very coarse particles, only modest increases in rate constant were achieved. One key criterion for particles being collected to the concentrate is a contact angle higher than the critical angle required for a stable bubble-particle attachment [26], whereas non-floating particles were found to have advancing contact angle values lower than the critical contact angle. Moreover, the critical contact angle for flotation is influenced by particle size, and it increases as the particle size decreases, which means finer particles have a higher critical contact angle to achieve floatability than coarser particles [43].

Particle properties have an overriding influence on froth stability. It is in the interest of flotation modeling and optimization to find correlations between particle properties and froth stability, in order to predict the flotation performance. The effect of particle properties on froth stability has been studied [34], and it was found that a large increase in froth stability occurred for feed particles of an average size less than 50 μm. Additionally, froth stability increased with increasing particle hydrophobicity up to an optimum value from 66° to 69° and after which it decreased. Particle size was found

to exert a more profound impact on froth stability than particle hydrophobicity; both particle size and hydrophobicity were shown to define the amount of particles that entered the froth phase. It was also found that once particles entered the top froth phase, the surface area of the particles would take a dominant role to define the froth stability.

Particles properties have great influence on the performance of froth flotation, to summarize, Table 2.1 lists the effect of the aforementioned influential factors on the performance of froth flotation.

Table 2.1. The influence of particles properties on the performance of froth flotation.

Properties	**Influence**
Size	Flotation recovery of both too fine and too coarse particles is usually remarkably low, and the effective particle size changes with mineral properties, as well as the chemical and physical environment of the system
Size distribution	When flotation is operated at coarser particle size distributions, the presence of fines in the system could, to some extent, improve the flotation performance
Contact angle	One criterion for particles being collected to the concentrate is a contact angle higher than the critical angle required for a stable bubble-particle attachment. Finer particles require a higher critical contact angle to achieve floatability than coarser particles
Shape	Particles with higher roughness and sharp edge are easier to be collected

Bubble size plays an important role in flotation kinetics along with particle properties and the hydrodynamic conditions of the cell. For the velocity of multiple bubbles in a swarm without particles [44], a velocity-size relationship has been found:

faster moving bubbles can speed up slower moving ones regardless of their size; a large group of slow moving fine bubbles can slow all bubbles; moreover, surfactant type also affected bubble velocity. Single bubble velocity profile has enabled observations in gas holdup [45], and it was shown that frothers added reduced bubble size and this would finally increase gas holdup. As the size of a bubble decreases, its velocity also decreases, which means an increased bubble retention time and therefore increased gas (air) holdup. At smaller bubble size, the liquid content in the froth phase is higher due to larger size of the Plateau borders. Different frothers produced about the similar minimum bubble size, although not the same maximum gas holdup [45]. The minimum velocity of different bubble size was therefore shown to be independent of the frother type.

Bubble size distribution in a mechanical flotation cell is considered to be influenced by at least two prime factors: frother concentration [46] and impeller speed [30,47]. Salt concentration [48], air flow rate [49] and other factors, such as the effect of solids concentration [50] and pH [51] also influence bubble size. The role of frother concentration is often summarized through the critical coalescence concentration (CCC) [48,52], the concentration above which bubble size in a swarm no longer decreases; or the related CCC95 [53], the concentration at which the bubble size reduces by 95% from that in pure water to the constant bubble size at high salt concentration.

Apart from bubble size, foam stability or froth stability can be used to characterize the influence of frothers and electrolyte solutions on bubble coalescence [46,54,55]. It was suggested by Tan et al. that mixed frothers could produce closely-packed and molecular cohesive films at the air-water interface which increased surface elasticity; in addition, a froth stabilizing mechanism based on a blend of frothers was proposed

[56]. The advantage of mix to provide independent control over two frother functions ─ bubble size and froth stability has been investigated, alcohols were added to provide a target bubble size with additions of polyglycol to provide the froth control [46]. It was found that below the alcohol CCC, even adding a small amount of polyglycol would decrease bubble size, while on the contrary, above the alcohol CCC, bubble size was found to increase with the addition of polyglycol [46]. Castro et al. have found that inorganic salts, similar to frothers, were able to prevent bubble coalescence although showed a CCC at a higher concentration than that of frothers [55].

Froth stability is known to play a significant role in determining the mineral grade and recovery obtained in a flotation operation. It depends not only on the frother types and concentrations, but also on the nature and amount of the particles present in the system [57]. It was found that maximal froth stability was reached with moderate particle hydrophobicity; the existence of a certain amount of entrained particles in the froth considerably reduced bubble coalescence, probably due to the increased slurry viscosity between bubble films which reduced the drainage speed of liquid films [58].

The dynamic stability factor is the ratio of the maximum volume of foam or froth generated to the air flowrate, it was also used to measure froth stability at industrial scale and link this froth stability to flotation performance [59]. For copper flotation tailings, it was found that for the same feed particle size distribution, there was an increase in dynamic froth stability with increased superficial gas velocity [33], and a local peak in dynamic froth stability corresponded to a clear increase in copper recovery.

The extraction of minerals in the froth phase is also strongly affected by the structure of the froth and the bubble size, since a froth with small bubbles is more likely to

enhance the entrainment of minerals [60]. The effect of bubble size on both bubble-particle attachment and film drainage was studied by Xing et al. [61]. They found that due to the high Laplace pressure on the film formed between a small bubble and the silica surface, its drainage kinetics was always faster compared to that formed between a big bubble and the silica surface; small bubbles were found to be beneficial to recover particles with relatively weak or moderate floatability, which mainly due to the high Laplace pressure formed that can drive the film to the range of hydrophobic force or even overcome the disjoining pressure barrier, leading to a final successful attachment [61].

Ren et al. [62] have studied the matching range between particles and bubbles, using electro-flotation to generate H_2 bubbles in a modified Hallimond tube and investigate the interaction between bubbles and cassiterite particles. Current density, cathode aperture, reagent and electrolyte concentrations were all found to be important factors that could control bubble size, and ultimately contributed to the control of fine particle flotation [62]. Bubble-particle interaction has been found to be affected by bubble size and particle size, since these two parameters influenced both the collision and attachment behavior of the particles and bubbles, which eventually impacted the final flotation recovery of fine minerals [63]. Besides, findings showed that there was an optimum matching range between particle size and bubble size, and within this range the optimal capture rate and highest recovery of the cassiterite were obtained [64]. It was found that cassiterite size of -10 μm, 10-20 μm, and 20-38 μm matched with 45, 59, and 68 μm bubble sizes, respectively [63], which indicated an advantage of utilizing small bubbles to improve the recovery of fine particles.

Both particles and bubbles have dominant roles in froth flotation, as far as the mechanism of flotation is concerned, turbulence is one of the decisive roles in

controlling the flotation performance. Turbulence effect has been classified into three main processes: particles suspension, air dispersion and particle-bubble collision, attachment and detachment [65]. Due to the three-phase opaque and highly dynamic environment present in the pulp phase of a flotation cell, it is impossible to directly visualize the behavior of a particle-bubble aggregate. Capillaries have been introduced to generate bubbles in a transparent rig, where it is possible to obtain insight into the behavior of rising bubbles, which can be linked to that of bubbles in the flotation pulp phase.

2.2 The use of capillary pinned bubbles

The use of capillary pinned bubbles allows the study of interfacial properties, which can provide a valuable insight into the fundamental operating mechanisms [22,66–68]. This technique has been used to generate bubbles that remain attached to the capillaries in a transparent experimental rig, where clear visualization of the bubble behavior can be obtained through high speed photography. Extensive studies have been conducted on induction time [69], coalescence of bubbles [68,70], and attachment and detachment of particles to bubbles [71].

2.2.1 Capillary pinned bubbles to study coalescence

In froth phase, particles are either attached to the bubble surface or entrained within the plateau border channels (the channels of the foams) [72]. A high rate of bubble coalescence may eventually render the froth reaching the top loading capacity (overloading) point of particles, after which further transportation of hydrophobic particles to the concentrate becomes challenging [73]. Therefore, the stability of the froth phase plays a crucial role to guarantee maximal recovery of particles.

The coalescence of bubble pairs is a common phenomenon in multiphase flow [74]. In froth phase, when two bubbles approach each other, a thin liquid film is formed between them. This film gradually becomes thinner due to the liquid drainage. The coalescence of bubbles leads to a decrease of the overall interfacial area, which is often regarded as the reason for particles being detached from the bubble. In this manner, the increase in the interfacial area of bubbles covered by particles causes an increased resistance to bubble coalescence, which simultaneously improves both the froth stability and recovery [75]. During this coalescence process, it is assumed that bubbles were coated with a monolayer of particles.

For monolayer particles in the foam, it has been found that foam stability decreased quickly after the particle contact angle exceeded 90°, due to particles bridging the film and causing the film to fail immediately [76]. However, apart from particle contact angle, the film loading(the particle packing density) also has great influence on the stability of a thin liquid film [77]. For the cases of two or more layers of particles, particles could stabilize a film at a contact angle higher than 90° (e.g. 129°), providing these particles are still closely packed [78].

Morris, et al. have investigated the effect of particles on the stability of a thin film and also predicted the failure of a thin liquid film covered with particles. It was found that with the change of contact angle, particles could either resist the coalescence or enhance the coalescence [78]. They have proposed that in a film supported by a double layer of spherical particles, there are three possible mechanisms of film failure: particle bridging and de-wetting, capillary pressure driven failure and film inversion [79]. The first mode occurred when the contact angle of the particle was larger than 90°, the film failed immediately when it contacted with a particle regardless of the double layer particles closely packed or spread out; The second case happened when the particle

contact angle was less than 90°, the film would not necessarily fail immediately, while the pressure and inter particle separation distances played a more dominant role. Finally, film inversion is similar to the bridging of a pore.

The relationship between particle contact angle, packing density and film stability has also been investigated [77,80]. The pressure at which the film thickness turned zero is taken as the critical capillary pressure P^*_{crit} and it increased abruptly with the increase of the particle packing density [80]. When particle contact angle was close to 90°, the P^*_{crit} was very low regardless of the separation distance, which showed that the capillary pressure exerted minor influence on film stability when single particles with a high hydrophobicity bridge both sides of a thin film [81].

Apart from the particle influence on the stability of the film, the coalescence between two capillary pinned bubbles with and without particles has also been studied intensively. The bubble oscillation patterns experienced during the coalescence process was illustrated by the change in the projected area [68]. The amplitude of the projected area decreased over a period of time and this could be used to indicate the dissipation of energy. A dampened oscillatory motion of the projected area is interpreted by:

$$A(t) = A_0 \exp(-\beta t) \sin(\omega t + \Psi)\,, \tag{2.3}$$

where $A(t)$ represents the displacement at time t, A_0 denotes the initial amplitude, ω is the angular frequency, ψ represents the phase shift and β is the damping coefficient. The damping coefficient serves as an indication of how fast the oscillation energy is dissipated. The fitting of the Equation (2.3) to experimental data points for the oscillation of a coalesced bubble is shown in Figure 2.2.

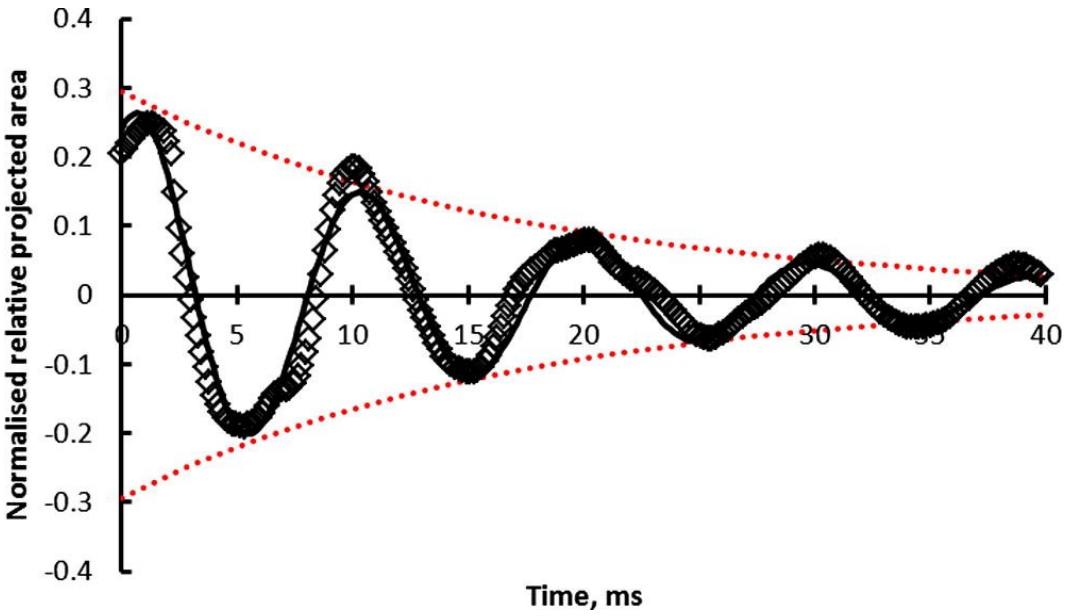

Figure 2.2. Fitting the calculated results to the experimental data points for the projected area oscillation of a coalesced bubble [82].

The time scale for the coalescence process can be closely linked to the stability of the film [70]. It was found that, particles present added resistance to impede the film drainage, the coalescence time became longer when more particles attached on the bubble surface [70]. Image sequences of coalescence of two capillary pinned bubbles with different surface coverages of particles are shown in Figure 2.3. For particle-laden bubbles, the initial resistance was found to originate from the lateral capillary interactions between particles loaded on the interface, which held the particles firmly together. The attached particles and, to some extent the presence of surfactants also exert a damping influence on the bubble oscillation, which plays a decisive role in the particle detachment phenomena [68].

Equation (2.3) only applies to the under damped oscillation or vibration, however, when the vibration is critically damped, or over damped, this equation becomes more complex and it is difficult to interpret the vibration. The damping coefficient β is

correlated with the attached particles on the bubbles [83], and Equation (2.3) can be described as:

$$A(t) = A_0 \exp(-\zeta \omega_n) \sin(\omega_d t + \Psi), \quad (2.4)$$

where ζ is the damping ratio that can be calculated as:

$$\zeta = \frac{c}{2M\omega_n}, \quad (2.5)$$

ω_n is the natural frequency of the vibration, ω_d is the damped frequency of the vibration, c is the damping constant which is correlated with the mass of particles attached on the bubble surface, and M represents the overall mass of the bubble, which includes the mass of the gas inside the bubble and the added mass of the bubble. The added mass characterizes the additional force required to accelerate a body when immersed in an ideal fluid [84]. With more particles attached on the bubble surface, the damping ratio becomes higher, resulting in a decreased vibration amplitude.

The bubble coalescence time with different surfactants has also been studied [82]. With the increase of surfactant concentration, the coalescence time was found to increase until it appeared a plateau. It was concluded that the increased coalescence time with surfactant concentration could not be attributed only to surface elasticity, though a minimum elasticity was required to achieve increased damping.

More in-depth research on two capillary pinned bubbles coated with particles have been studied to give insight into the coalescence of bubbles and its effect on the detachment of particles. It was found by Ata that the damping coefficient of coarser particles tended to be smaller than that for finer particles, leading to a higher detachment of coarser particles [68]; particles with higher hydrophobicity were shown to be less likely to detach from the bubble surface. Particle density is also an important

parameter in the flotation process [85], it was found that less dense particles tended to form a higher coating resistance against coalescence, so they were more effective to stabilize bubble interfaces; while for denser particles, they were seen to be dislodged during the contact of two bubbles, which might have contributed to the coalescence.

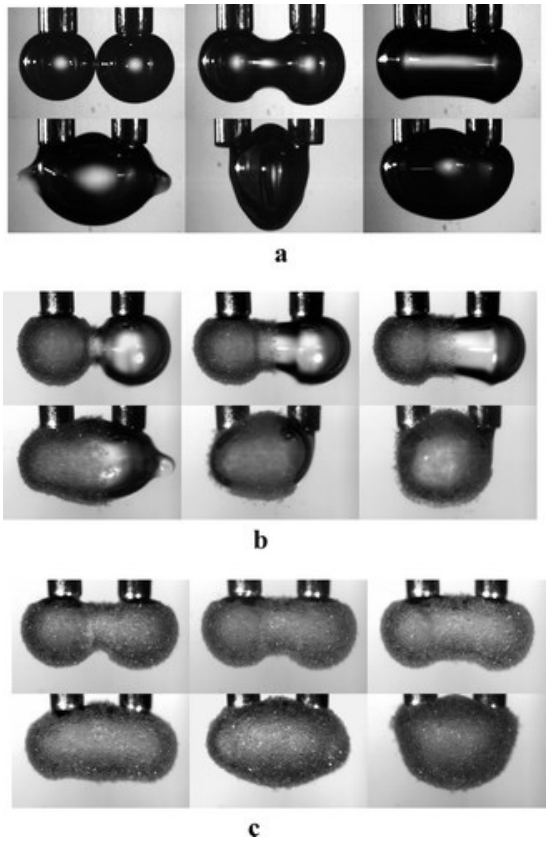

Figure 2.3. Photo sequences of coalescence for (a) both uncoated bubbles, (b) coated and uncoated bubbles, and (c) both coated bubbles. Time interval between frames was about 0.5ms [70].

In terms of the influence of pH on the bubble stability [86]: at pH 10, the air bubbles were found to be highly stable when coated with latex compared to those equilibrated at pH 2, and this difference was attributed to a close-packed latex layer at higher pH value; when comparing different particles, compression of the latex layer on bubble surface induced a stronger elastic behavior during coalescence, which rendered the bubble more stable than those coated with spherical glass beads.

The energy released by coalesced bubbles triggers a violent change of the bubble surface area, which is sufficient to dispel some of the attached particles from the bubble surface, however, the frothers and attached particles hinder the bubble vibration and therefore reduce the detachment of particles during bubble coalescence [87]. This reveals that in the flotation process, the role of frothers is more than simply controlling bubble size or forming a stable froth as commonly believed [88]. The selectivity in the detachment of particles during coalescence and the characterization of methyl isobutyl carbinol (MIBC) action on coalesced bubbles have been investigated [67,75]. The presence of MIBC and particles was found to noticeably dampen the oscillation coalescence of bubbles, although their effects on bubble stability decoupled. The oscillation was strongly damped in the presence of MIBC at high concentrations, whereas, this was not the case in NaCl solutions [66].

Apart from air bubbles, dynamic behaviors of CO_2 bubbles coalescing at two parallel capillary orifices were also investigated in a microalgae suspension [89], which has implications in mass transport and biomass production. It was found that the adsorption of microalgae on the bubble surface increased the time needed for the coalescence of bubbles, and the coalesced bubbles were more easily detached from the capillary tip than that in pure water.

Similarly, the mechanism of coalescence of bubbles has been adapted to other applications, relevant studies include liquid marble (drop coated with polystyrene particles) and droplet interaction and stability [90], colloidosomes interaction dynamics and stability [91], as well as the influence of the interfacial ageing and temperature on the coalescence of oil droplets [92].

2.2.2 Capillary pinned bubbles to study induction/attachment time

Induction time, i.e., attachment time, is normally adapted as a very important parameter related to flotation recovery. The influence of liberation of copper sulfide ore on bubble-particle attachment time in flotation has been studied by Albijanic et al. [93]. It was found that attachment time was reduced when the amount of highly and moderately liberated copper minerals were increased. It has also been recognized that some particle shapes exhibited better floatability than others, which is usually attributed to the influence of particle shape and roughness on the induction time required for the attachment to occur [39,93]. Induction time is way lower for rough particles compared to spherical ones [38] and also has a close relationship with collector adsorption, pH, zeta potential of minerals and flotation recovery [94]. It was found that by Albijanic et al. that when the concentration of the collector exceeded its critical micelle concentration (CMC), a bilayer of surfactant molecules could be formed at both the particle and bubble surface, prohibiting the contact between particles and bubbles, therefore, the induction time sharply increased and flotation recovery reduced [95]. It was also indicated by other studies that induction time increased with increasing particle size and decreasing particle surface hydrophobicity [28].

Apart from the influential factors mentioned above, the physical environment would also influence induction time [96]. The initial distance between the particle and the bubble, displacement and bubble size, as well as the velocities of the air bubble approached and then retracted from the particle were found to have decisive influence on induction time [69]. Other operational parameters, such as stirring speed, would influence the turbulence within the pulp and froth phases, therefore triggering different induction times [30].

One representative device for measuring induction time is the CSIRO Milli-Timer [97], the schematic diagram of which is shown in Figure 2.4. It consists of a submerged bubble generating from a capillary tip, onto the surface of which particles are dropped, and a high-speed camera was applied so as to capture the induction time, attachment and detachment of particles.

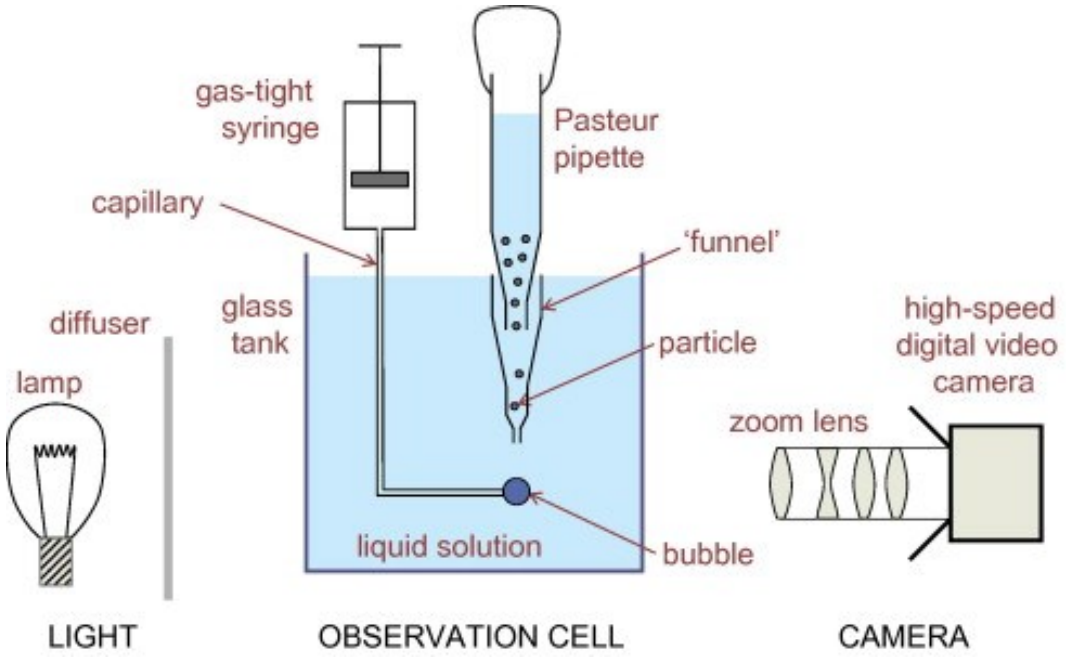

Figure 2.4. Schematic of the CSIRO Milli-Timer device [97].

Figure 2.5 shows another device that used to determine the induction time, the integrated thin film drainage apparatus (ITFDA) [98,99], which combines the function of the induction timer and the AFM (Atomic-force microscopy). This apparatus is equipped with speaker diaphragm which can push the air bubble toward or retract from the lower particle surface, meanwhile, a mineral particle connects to a force sensor, within which both the time and the hydrodynamic force can be detected simultaneously.

Overall, with the aid of capillary pinned bubbles, induction time can be tested and influential factors can be determined, which could provide valuable information for froth flotation.

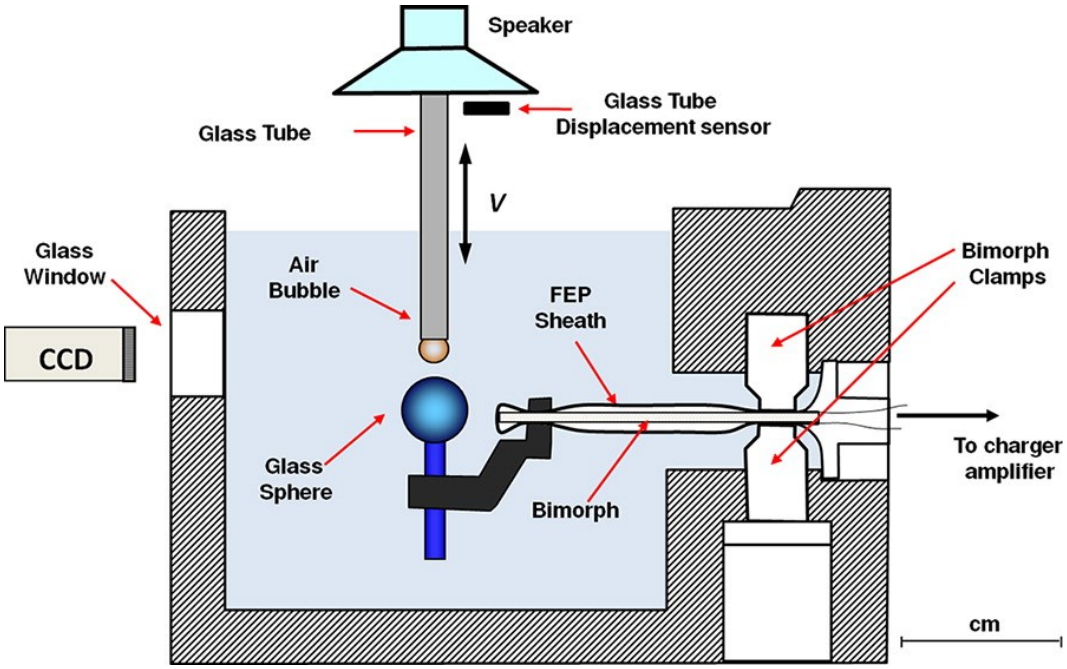

Figure 2.5. Schematic view of the integrated thin film drainage apparatus: (a) chamber configuration; (b) a piezoelectric bimorph used to measure the charge generated on the bimorph cantilever under an external force [98].

2.2.3 Capillary pinned bubbles to study attachment and detachment

In froth flotation, bubble-particle attachment occurs when the contact time exceeds the induction time. Another way to describe the attachment is using the method of energy barrier, where the kinetic energy of a particle has to exceed the energy barrier between the particle and the bubble surface [28]. Once a stable particle-bubble aggregate is formed, the particle may only be dislodged from this state on condition that it is supplied with sufficient kinetic energy to exceed the detachment energy [14].

However, some gangue minerals, which normally occupy a large proportion in the ores, can easily be collected and then transferred to the concentrate due to mechanical entrainment and entrapment. To visualize and analyze the real attachment and detachment between particles and bubbles and at the same time exclude the impact of mechanical entrainment and entrapment, capillary pinned bubbles [97] or bubble pairs

[75] covered with hydrophobic particles have been introduced and the interaction between particles and bubble has been analyzed. Experimental design can be divided into three groups: one bubble contact with one particle, one bubble coated with several particles and two bubbles covered with particles.

(1) One bubble contact with one particle

The effect of solvent addition for the bitumen-air bubble attachment has been investigated [69]. It was shown that attachment can be facilitated by increasing the zeta potential (electro kinetic potential) and hydrophobicity of bitumen, together with reducing bitumen viscosity.

The interaction between an air bubble and a solid surface under dynamic conditions has been studied [98,99]. It was found that salt concentration, solution pH and surfactant all exerted great impact on the hydrophobicity of solids, and these together with force barrier and approaching speed of bubble to solid surface all had great influence on their interaction.

Recent studies have introduced a closed single bubble-particle (steel ball) aggregate to better understand the influence of real turbulent environment in flotation on particle detachment [22,100,101]. The dynamic contact angle of a bubble detaching from a particle showed an asymmetric distribution along the three-phase contact line. It was found that to initiate the detachment of a particle from a bubble, either the maximum advancing contact angle or the minimum receding contact angle should be reached, after which the length of the three-phase contact line decreased, which led to a smaller capillary force; the detachment happened only on condition that the buoyancy force was higher than the capillary force, regardless of the turbulence of liquid flow. Three different detachment modes have been identified [100], including: (1) bubble pulled

off the particle, (2) bubble sheared off the particle, and (3) bubble entrained into an eddy and followed its movement, and these three modes together give in-depth insight into the real flotation environment.

(2) One bubble coated with several particles

The detachment of coarse particles from oscillating bubbles was explored as a function of particle hydrophobicity and shape, as well as medium viscosity [71]. The schematic diagram of the apparatus with electro-acoustic technique is shown in Figure 2.6. The results showed that the detachment force was increased with an increase in the contact angle of particles and viscosity of the suspending medium. It was also shown that with the same size and similar contact angle value, ground particles required larger forces in order to detach from the interface than spherical ones; high liquid viscosity reduced the rate of movement of the three-phase contact line, rendering a more stable bubble-particle aggregate.

Another method that has been used involves using a nozzle to drop several particles onto a stationary bubble [38,39], similar to the device shown in Figure 2.4. The effect of both roughness and shape factor of particles on surface properties and flotation characteristics of particles have been studied. Grazing trajectory and attachment efficiency of both smooth spherical and ground particles before and after etches have been explored. It was found that an increase in surface roughness by etching could improve flotation recovery, increase the contact angle as well as bubble attachment. Moreover, when a particle moved towards the bubble, multi-body interactions from other particles nearby could be sufficient to initiate the attachment.

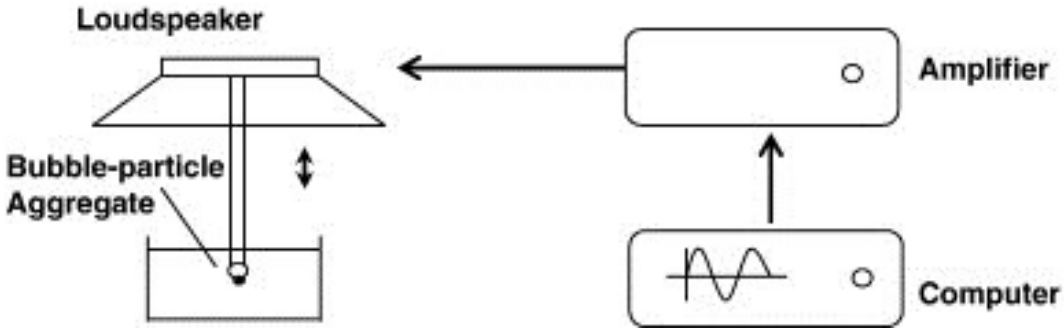

Figure 2.6. A schematic diagram of the apparatus using loudspeaker to investigate the detachment of particles from bubbles [71].

(3) Two bubbles covered with particles.

Research on two capillary pinned bubbles coated with particles has been applied to give insight into the coalescence of bubbles and the post-rapture influence on the detachment of particles [68]. This has already been given in details in Section 2.2.1.

Capillaries have also been used to continuously generate bubbles in order to study the velocity and shape change of rising bubbles [102,103], and these will be discussed in detail in the next section.

2.3 Motion of rising individual bubbles

2.3.1 Characterization of rising air bubbles

The formation of bubbles at a submerged capillary and their subsequent rise due to buoyancy force are one of the most common gas-liquid flow phenomena [104–107]. Understanding the dynamic interaction between the gas and liquid phases is of great value for a wide range of industrial applications including bubble column reactors [2,108,109], gas-solid fluidized beds [110], froth flotation in mineral processing [35,63] and plastic recycling [4], wastewater treatment [111,112], as well as de-inking in paper industry [9].

The bubble characteristics include equivalent diameter, rising velocity, elongation (deformation or aspect ratio), as well as bubble rising path [113].The process of bubble formation determines the original bubble size in a system. The dynamics of bubble formation and its pinch off process have been classified into three stages [114]: expansion stage, elongation stage as well as pinch-off stage. In the first expansion stage, with continue air injection, the bubble grows although it still connects to the capillary tip. As gas continues injected, the spherical bubble becomes elongated when the upward overal force is lower than downward one. Once the length of the bubble neck exceeds a certain value, the bubble steps into the final pinch off stage. It was observed that a higher concentration of surfactant gave smaller bubbles with lower rising velocity [98].

The rising velocity of bubbles determines the contact time between the liquid gas phases which impacts the interfacial transport phenomena as well as mixing [115]. Different parameters have been used to characterize the behavior of a single rising bubble [113]. Bubble dynamics, especially its shape and rising velocity, are decisive parameters that affect the behavior of the gas-liquid two-phase flow, including gas residence time, void fraction, and gas-liquid interface transferring properties [105,116]. To accurately predict bubble velocity is challenging since its rising velocity is influenced by many factors such as fluid physical properties, liquid purity, bubble size, bubble shape, bubble trajectory and air injection mode, etc.

As a key parameter in bubbly flows, bubble shape is determined by the physical properties of the fluid, the bubble size and its velocity [117]. In a low turbulence environment, however, the interpretation is normally appropriately simplified, and the bubble is usually assumed symmetric ellipsoid with shape defined only by its major and minor axis [118]. In such flows, apart from the bubble size, only the aspect ratio

is needed to describe the shape [1,118–120]. It was found that with an increase in the concentration of MIBC, the aspect ratio of the bubble increased, making it more spherical [120,121], moreover, oscillations in aspect ratio and velocity were seen to be inversely related.

Oscillatory movement is a common behavior of a moving body with respect to its surrounding fluid environment. When the bubble size was sufficiently small, its rise path was almost rectilinear; with the increase of bubble size, its rise path began to oscillate and it became zigzag or spiral [122]. It was found that in pure water, rising bubbles, with a diameter range of 1-2 mm, had two steady shapes ─ a sphere and an ellipsoid, and this difference is mainly determined by the size of the capillary where bubbles were generated and detached [123]. It was also found that bubbles with a diameter of less than 1.5 mm rose rectilinearly; spherical bubbles followed a zigzag path, while ellipsoidal bubbles followed a spiral path. For an isolated air bubble (diameter of 2.5 mm) rising in still water [124], it was observed that after a initial acceleration period, the bubble started oscillating on an almost plane zigzag. Eventually, it progressively stepped into a final stable helix stage.

The bubble characteristics are used to reflect different liquid conditions, and the influential factors will be discussed in the next section.

2.3.2 Influence of reagents and temperature on bubble motion

Frothers can be used to aid the generation of small bubbles, and they also influence how bubbles move in a liquid [120,125,126], more specifically, affect bubble rise velocity through control bubble shape.

It has been found that frothers and certain inorganic salts not only inhibit bubble coalescence but also reduce bubble rise velocity [48]. Increasing concentration, on

average, creates more spherical bubbles rising at lower velocities [113]. Bubbles accelerate and reach their maximum velocity at a given period of time depending on frother type and concentration, after that, bubbles decelerate and then oscillate about a mean velocity [120]. A relationship between bubble shape and its velocity was observed: the more spherical the bubble, the slower the rise. Moreover, this relationship was independent of solute types [48,121].

Apart from frother or solute type and condition, frother structure is another influential factor. For instance, the alkyl chain length [125,127], the position of the methyl branch and hydroxyl group in alcohols [127,128], and the number of ethylene oxide groups [126]. It was found that different frother structures influenced the concentration for bubbles to reach minimum velocity (CMV), and a lower CMV represented a structure that was more effective to reduce bubble rise velocity [128].

Chemical adsorption [129,130] on the initial bubble formation influences the bubble motion after they detach from the capillary. It was found that with a longer adsorption time, the maximal velocity were lower, and less time required for the bubble to reach terminal velocities. The adsorption coverage of surface active reagent caused the partial immobilization of the bubble surface, which led to the reduction of the bubble terminal velocity when compared to the one in pure water. At low solution concentrations, three distinct stages in the bubble motion was identified [130]: (1) a rapid acceleration, (2) a maximum velocity value followed by its monotonic decrease, and (3) establishment of the terminal velocity. While in pure water or at high concentrations with longer adsorption time, stage (2) was skipped and the bubble terminal velocity was established immediately after the acceleration period.

Ionic liquids constitute a new group of substances that are considered as potential substitutions for many traditional organic reagents in reaction and separation systems.

They have been found to have a similar effect as frothers to change bubble motion [102,121]. In an ionic liquid, the bubble shape and velocity oscillated in a similar linked pattern: higher concentration creating more spherical bubbles with lower rising velocity. Compared to pure water, the addition of inorganic salts or frothers generated a lower bubble surface area which was found to contribute to a higher gas holdup.

Temperature also influences the behavior of rising bubbles. It was found that in different ionic liquids, as the temperature increased, the bubble terminal velocity increased and its equivalent diameter decreased [131]. The reason for that is higher temperature caused a lower viscosity and surface tension, which changed the bubble formation and its rising velocity indirectly. With different temperatures, spherical and ellipsoidal bubbles were compared in distilled water, it was shown that at high-temperature, the measured results of the rise velocity of a single bubble and its rising path oscillation roughly agreed with the correlations for the bubbles in contaminated liquid [122]. The bubble velocity was impacted by the air injection mode in room temperature water. At high temperature, the way of injection also affected the bubble velocity, but the influence of the initial deformation to the bubble velocity was decreased when compared to the bubble generated in water at a room temperature [122].

2.3.3 Influence of bubble size and particles on bubble motion

Bubble size exerts influence on the bubble velocity as well as bubble shape, the latter also indirectly change bubble velocity. The rising behavior of single bubbles with a diameters range of 0.5 to 4.0 mm have been investigated in both turpentine and pine resin [132]. Results showed that bubbles with a diameter of less than 1mm rose rectilinearly; the increase of the solution concentration reduced the amplitude of the

bubble trajectory oscillation. Moreover, this trajectory was influenced by both the liquid viscosity and the bubble diameter. When the bubble size increased, its rise velocity was observed to firstly increase to a peak value, after which it decreased slowly.

Liu et al. have studied the bubble dynamics in both stagnant water and glycerol aqueous solution [133]. Results have shown that bubble shape, rising path and terminal velocity in water, which were closely related and strongly influenced by each other, were also found to be determined by the size of the bubble. When bubble sizes were small enough, they remained spherical and rose rectilinearly; with bubble size increased, the bubbles began to deform to ellipsoidal, oblate ellipsoidal, or cap shape, with strong shape oscillation, and finally proceeded in a zigzagging, helical or nearly helical motion. The reason for this is because in water, the bubble shape is mainly dominated by the surface tension and the inertial force, while the influence from the viscous force can be negligible. Bubble motion changes from surface tension force dominated to inertial force dominated and the terminal velocity increases gradually with the bubble size increases. The gravity force should be considered if the bubble diameter is large enough. In contrast, in a glycerol solution, bubble shape was dominated by all the three forces: the viscous force, surface tension and inertial force; the bubble shape, rising path and velocity were stable under a certain bubble diameter.

The bubble terminal velocity has also been studied by Liu et al. [116]. They have found that in water, when the bubble diameter was less than 0.83 mm, its terminal velocity increased while aspect ratio (minor axis divided by the major axis) decreased. With bubble diameter in the range 0.83-6 mm. there was a wide distribution of both the bubble terminal velocity and its aspect ratio. When bubble size exceeded 6 mm, the level of scattering distribution was reduced, and the terminal velocity increased

gradually with a relatively stable aspect ratio. In the surface-tension-dominated regime, the bubble parameters was found to vary significantly. In the inertia-dominated regime, the terminal velocity increased gradually with increased bubble diameter while their aspect ratios varied in a narrower range than that in the surface-tension-dominated case. In glycerine aqueous solution, the terminal velocity increased with increasing bubble size and there was a more centralized bubble velocity.

Hydrophobic colloidal particles, as a bubble stabilizing agent, was reported to have potential applications in froth flotation. The influence of particles on the formation of bubbles from a submerged capillary has been investigated by Ata et al. [103]. Particles were found to be able to prevent the spreading of the triple line on the capillary, leading to the formation of small bubbles. Bubble size reduced almost linearly with the number of particles in the solution, and this reduction in the bubble size over the concentration range studied appeared to be higher than that in the frother solutions. Additionally, it was found that bubbles formed in a mixture of frothers and particles are smaller than those generated in the frothers and particles alone. It was also noticed that bubbles rising in the presence of a silica suspension always exhibited irregular shapes.

Vafaei and Wen have studied the behavior of a bubble generated from a nozzle (micrometer size) immersed in a quiescent pool of aqueous gold nanofluid, and this has been compared with a bubble generated in deionized water [134,135]. They have found that both the bubble departure volume and growth time reduced considerably when particles were added in the solution, which was attributed to the reduction of the radius of the contact line of the air bubble as well as its interfacial energy. During bubble formation, nanofluids were found to prevent the spreading of the triple line, meanwhile, the triple line was pinned around the middle of the tube wall during the rapid bubble growing stage, whereas it spread to the outside of the tube for the bubble

generated in the pure water. They have also found that the variation of surface tensions and the resultant force balance at the triple line were believed to be responsible for the modified dynamics of the triple line and final bubble formation.

Eskanlou, et al. have investigated the trajectory and rise velocity of loaded and bare bubbles [6]. It was found that bare bubbles tended to follow a zigzag path, while for the particle-laden bubbles, the presence of particles stabilized the bubble motion and its path was more centralized ─ close to a straight vertical trajectory. In addition, with bubble size increased, the rise velocity and the deviation from the straight rising trajectory increased.

The processes of a particle-loaded bubble arriving at the top of the air-liquid interface and bouncing back afterwards have been investigated [7]. It is known that abrupt variation of bubble velocity might dislodge the particles attached on its surface. However, this study has shown that, rather than detaching from the bubble surfaces, the particles moved around the surface of the bubble and hindered the vibration of the bubble motion. It was found that the bubble kinetic energy dissipated by two mechanisms: the pulsation of bubble shape and the motion of particles on bubble surface.

2.4 Force analysis and prediction of rising bubbles

2.4.1 Forces and drag coefficient

For a capillary pinned bubble which is easy to control its size, the bubble is usually assumed to be an oblate spheroid which is symmetrical along its minor axis [120]. This shape is due to the influence of both the buoyancy force and the capillary force [22]. For a rising bubble detached from the capillary, its behavior, including velocity and

aspect ratio, is determined by several acting forces. A bubble rises mainly because of the buoyancy force, which acts against the drag force. The density and viscosity of the gas in a bubble also influence the bubble behavior, but these effects are not as significant as the drag force and buoyancy force exerted on the rising bubbles [105,106]. On the basis of energy balances obtained for the system consisting of a bubble freely rising in a viscous liquid, in steady-state conditions, the constant (terminal) velocity of the bubble was a result of the balance between the buoyancy force and drag force [118].

The buoyancy force [136] is given by:

$$F_B = \frac{4}{3}\pi \mathrm{R}_b^3 \Delta\rho g\ , \tag{2.6}$$

where R_b^3 represents the bubble radius, g is the gravity acceleration constant and $\Delta\rho$ is the density difference between liquid and air. Since the density of the air is way smaller than that of water, $\Delta\rho$ is usually regarded as equal to the density of the water ρ.

The drag force [130] can be written as:

$$F_D = -\frac{C_D \rho u^2 A}{2}, \tag{2.7}$$

where C_D is the drag coefficient, u is the velocity of the free stream of fluid relative to the bubble, here we use it as the velocity of the rising bubble. A is the projected frontal area of the bubble and it is perpendicular to the bubble vertical moving direction. For spherical objects, A equals $\frac{\pi d^2}{4}$, and d is the bubble diameter.

The drag coefficient is a dimensionless quantity and is strongly influenced by factors such as the fluid properties and bubble size [137]. It is usually modified from classical

models in order to better predict the velocity of the rising bubbles [138] or to improve the accuracy of CFD simulations [109,139].

The Schiller-Naumann drag coefficient [140] is one of the widely used models and it is expressed in terms of Reynolds number (Re):

$$C_D = \begin{cases} \frac{24}{Re}(1 + 0.15Re^{0.687}) & if\ Re < 1000 \\ 0.44 & otherwise \end{cases}, \tag{2.8}$$

Reynolds number is a dimensionless quantity to identify similar flow patterns in different fluid flow environment. It is the ratio between inertial force and viscous force [141], and is defined as:

$$\mathrm{R}e = \frac{\rho d u}{\mu}, \tag{2.9}$$

where μ is the dynamic viscosity of the fluid. In the Schiller-Naumann drag coefficient, bubbles are regarded as spheres. However, the deformability of a bubble may lead to different shapes and flow regimes, which finally exerted impact on the mass and heat transfer of these processes [138]. With regard to the bubble deformation, modified models are normally derived in terms of some dimensionless numbers [118,142,143] including Eötvös (Eo), Morton (Mo), Weber (We), and Galilei (Ga) numbers et al. These are given as follows:

$$\mathrm{E}o = \frac{\Delta\rho g R_{eq}^2}{\sigma};\ Mo = \frac{g\mu^4\Delta\rho}{\rho^2\sigma^2};\ We = \frac{2\rho u^2 R_{eq}}{\sigma};$$
$$Ga = \frac{\rho\sqrt{gR_{eq}}R_{eq}}{\mu}, \tag{2.10}$$

where σ is water/air interfacial tension, R_{eq} is the equivalent radius of the bubble.

Some studies have also been conducted to predict the terminal velocity of a rising bubble [105,144], while these studies are out of the scope of this work. The drag coefficient is a fundamental parameter for predicting the velocity of a rising bubble and thus for modeling bubbly flows , it is influenced by the property of the liquid as well as the aspect ratio [1,117]. Different models have been proposed for the prediction of bubble motion, and this will be the subject of the next section.

2.4.2 Prediction of bubble motion

The bubble motion has a direct influence on the interfacial heat and mass transfer, and different drag coefficient models have been developed under different Reynolds number values so as to predict bubble motion [130]. Knowledge of the shapes of bubbles has also been developed and is of great importance in modeling the drag force acting on a bubble.

The adsorption of reagents on the bubble surface can exert a significant effect on the surface forces, on the drag coefficient as well as on the bubble velocity. Tomiyama et al. [137] have proposed the drag coefficient of bubbles under different contamination of liquid systems. The corresponding drag coefficient in pure, slightly contaminated, and contaminated gas-liquid systems are concluded as follows:

For a pure system

$$\mathrm{C_D} = \max\left\{\min\left[\frac{16}{Re}(1+0.15Re^{0.687}), \frac{48}{Re}\right], \frac{8E_o}{3(E_o+4)}\right\}; \qquad (2.11)$$

For a slightly contaminated system

$$\mathrm{C_D} = \max\left\{\min\left[\frac{24}{Re}(1+0.15Re^{0.687}), \frac{72}{Re}\right], \frac{8E_o}{3(E_o+4)}\right\}; \qquad (2.12)$$

For a contaminated system

$$C_D = \max\left\{\frac{24}{Re}(1 + 0.15Re^{0.687}), \frac{8E_o}{3(E_o + 4)}\right\}. \quad (2.13)$$

These drag coefficients apply to the liquid conditions when Re values are within a range of 10^{-3} to 10^5.

The drag coefficient fluctuation of a single bubble in deionized water has been studied and predicted [145]. It was found that the terminal velocity pulsated periodically, indicating a variation of the drag coefficient. Based on the experimental data analysis, an improved drag model that combined Reynolds number, Eötvös number and Weber number was derived and given as:

$$C_D = \max\left\{\begin{matrix} min\left(\frac{24}{Re}(1 + 0.15Re^{0.678}), \frac{72}{Re}\right), \\ \frac{24}{Re}(1 + 0.15Re^{0.687})\frac{Re^{0.55}Eo^{0.95}We^{-1.10}}{12.6} \end{matrix}\right\}. \quad (2.14)$$

This model is valid for both spherical and non-spherical bubbles within a Reynolds numbers range of 550 to 1700. However, it is not possible to apply to bubble rising in other liquids or solutions.

Proceeding the study of rising bubbles in deionized water, the motion of single bubbles rising in three aqueous solutions including 2-octanol, MIBC and OP-10 ($C_{32}H_{58}O_{10}$) has also been investigated [146] and the added mass force and history force were also considered. The added mass characterizes the additional force required to accelerate a body when immersed in an ideal fluid [84]. The history force, also known as Basset force, is caused by the unsteady motion that characterized by a time-varying velocity, it is dependent on the acceleration [147]. A new correlation was proposed to predict the drag coefficient from the fluctuated bubble motion, and this correlation is shown as:

$$\mathrm{C_D} = \max\left\{min\left(\frac{24}{Re}(1+0.15Re^{0.678}), \frac{72}{Re}\right), \right. \\ \left. \frac{24}{Re}(1+0.15Re^{0.687})\frac{Re^{0.55}Eo^{0.95}We^{-1.10}}{12.6}\left(\frac{Mo}{Mo^*}\right)^{0.048}\right\}, \tag{2.15}$$

where Mo^* is the Mo of water at 293K (value 2.6×10^{-11}). This new model could successfully give prediction to the periodically fluctuated drag coefficient of bubbles in both pure and contaminated liquids. It also represented well the experimental data which covered more than 20 pure liquids and contaminated liquids in a very wide range of Reynolds numbers (value from 10^{-3} to 10^{5}).

Based on the experimental data of a single bubble rising in ionic liquids, two new empirical correlations were proposed — one was to correlate the drag coefficient as a function of Reynolds number, and the other one was to correlate the aspect ratio as a function of a new dimensionless parameter IL, which represents experimental data for gas bubbles [131].

$$\mathrm{C_D} = \mathrm{aRe^b}Mo^c\,. \tag{2.16}$$

The parameter $a, b,$ and c can be calculated by a least square method. This correlation was valid in a low Re range of 0.5 to 50.

The expression of IL was proposed as:

$$\mathrm{IL} = \mathrm{Re}\cdot\mathrm{Eo} = \frac{\rho \mathrm{V_T} g d^3 \Delta\rho}{\mu\sigma}, \tag{2.17}$$

where V_T denotes the bubble terminal velocity. The aspect ratio AR can be represented as:

$$\mathrm{AR} = \frac{\mathrm{a}}{b + c \cdot IL^{d}} \ , \tag{2.18}$$

the parameter of $a, b, c,$ and d can be obtained using a nonlinear fitting.

Li et al. have investigated the motion of hydrate-film-covered methane bubbles in water [1]. They have found that the total mass of the bubbles was increased due to the presence of hydrate film, the bubble was less likely to deform, and its aspect ratio remained relatively constant during ascent and decreased as the equivalent diameter increased. The presence of hydrate film was also found to impede the bubble rising velocity.

The aspect ratio of the bubble is proposed as:

$$\mathrm{AR} = 1.10128 - 0.20352 \cdot \ln(Eo + 2.85626). \tag{2.19}$$

The drag coefficient of the bubble is described as:

$$\mathrm{C_D} = min\left\{ f\left(\frac{a}{R}\right)^{2}, max\left\{\frac{24}{Re}(1 + 0.15Re^{0.687}), \frac{2}{3}\sqrt{Eo}\right\}\right\}, \tag{2.20}$$

where

$$f = \frac{48}{Re}\left(\frac{1 + 12Mo^{\frac{1}{3}}}{1 + 36Mo^{\frac{1}{3}}}\right) + \frac{0.9Eo^{\frac{3}{2}}}{1.4\left(1 + 30Mo^{\frac{1}{6}}\right) + Eo^{\frac{3}{2}}} \ , \tag{2.21}$$

$$\left(\frac{a}{R}\right)^{2} \cong \frac{10\left(1 + 1.3Mo^{\frac{1}{6}}\right) + 3.1Eo}{10\left(1 + 1.3Mo^{\frac{1}{6}}\right) + Eo} \ . \tag{2.22}$$

Aoyama et al. have studied the aspect ratios of single ellipsoidal bubbles in glycerol-water solutions contaminated with surfactant [148]. The bubble diameters ranged from 0.80 to 5.8 mm and the Reynolds number value ranged from 0.36 to 170. For a clean bubble without surfactant, all the relevant forces, i.e. the viscous, inertial, buoyant and surface tension forces, have been considered to correlate bubble shapes. The proposed correlation of aspect ratio for a clean bubble is:

$$\mathrm{AR} = \frac{1}{[1 + Eo^{1.12}Re]^{0.388}}, \tag{2.23}$$

while for contaminated bubbles, the coefficient is modified with a correlation shown as:

$$\mathrm{AR} = \frac{1}{[1 + pEo^{a}Re^{b}]^{q}}, \tag{2.24}$$

where p, q, a and b are constant and can be yielded by applying least-square fitting to the experimental data. It was applicable to fully-contaminated bubbles in Triton X-100, SDS, 1-octanol and 1-decanol solutions.

A single bubble (diameter range 0.54-10.21 mm) dynamic was studied in water and glycerin [133]. It was found that in water with low viscosity, the Weber number gave the best prediction for the correlation substitution IL in Equation (2.25).

$$\mathrm{AR} = \frac{1}{a + b \cdot IL^{c}}. \tag{2.25}$$

In glycerine aqueous solution with high viscosity and when the bubble diameter was large enough, the bubble shape was influenced by viscosity dramatically, therefore, it was not appropriate to use any dimensionless number Eo, We or Re alone to predict the bubble deformation. Correlations [133] combining Weber number with Eötvös

number and Weber number with Reynolds number have been proposed to give satisfactory predictions for aspect ratios, which are shown as follows:

$$\mathrm{AR} = \frac{1}{a + b \cdot We^{c} Eo^{e}}\ , \tag{2.26}$$

$$\mathrm{AR} = \frac{1}{a + b \cdot \mathrm{We}^{c} Re^{e}}\ . \tag{2.27}$$

2.5 Summary

This chapter reviews the relevant studies for the work developed as part of this thesis, ranging from the background of froth flotation to the research focused on individual bubbles. The previous applications of capillary pinned bubbles have been reviewed. Moreover, the motion of a bubble after it detaches from the capillary as well as different influential factors on rising bubbles have been discussed. Finally, the force analysis and the model of bubble motion including the prediction of drag coefficient and aspect ratio have been introduced.

The stability imparted by solid particles was shown to be much more effective than for the case of surfactants [149]. A better understanding of the hydrodynamics in these systems has important implications for processes such as froth flotation, where particle-bubble aggregates play a key role in determining its performance [42]. Research at the bubble-particle scale has considered different aspects of particle-stabilized bubbles, such as coalescence, but has only dealt with bubbles that are fixed to a capillary. Bubble loading is a very important factor which strongly influences flotation recovery yet very little fundamental work has been done. In terms of a bubble coated with particles while ascending in the fluid, not as many studies have been conducted and, therefore, the phenomena are less understood.

The aim of this research is to explore the effect of the level and the size of attached particles on the behavior of rising bubble-particle aggregates. The main research objectives include:

1. Investigating the influence of particles on the velocity, acceleration, and aspect ratio of particle-laden bubbles. Moreover, the relationship between these three parameters will also be discussed.
2. Analyzing the oscillation periods of bubbles with different particle coverage and particle size.
3. Calculating the forces on bubbles and particles, and quantifying the effect exerted by particles on rising bubbles. This will allow, for the first time, the generation of a modified drag coefficient model for particle-laden bubbles.

These findings will provide valuable insight into the behavior of particle-laden bubbles, which can be used to inform the modeling of pulp phase flotation phenomena and other relevant processes that rely on particle-laden bubbles.

Chapter 3 Methodology

This chapter introduces the main techniques involved in the experiments, including material and reagent preparation and property characterization, the setup of the experiment and experimental procedure in this work.

3.1 Materials

Five sizes of spherical soda lime glass beads particles were supplied by SiLi Sigmund Lindner GmbH (Germany), with a mass density of 2.5 g/cm^3. Myristyltrimethylammonium bromide (TTAB) of analytical grade was obtained from Sigma-Aldrich Chemical Co. (U.K.) and used as a collector. The Sauter-mean diameter, d_{32}, as well as d_{50} and d_{90}, which were determined using a Malvern Mastersizer 3000, are shown in Table 3.1. The sample size distribution and cumulative volume fractions are shown in Figure 3.1 (a) and Figure 3.1 (b), respectively. All of the samples used are in a narrow size distribution range. The experiments were performed at a room temperature of 15 °C under natural pH condition.

Table 3.1. The Sauter-mean diameter (d_{32}), d_{50} and d_{90} for the samples used in the experiments.

Sample	d_{32} (μm)	d_{50} (μm)	d_{90} (μm)
Size 1	19	39	64
Size 2	65	67	91
Size 3	88	91	124
Size 4	119	121	156
Size 5	217	219	266

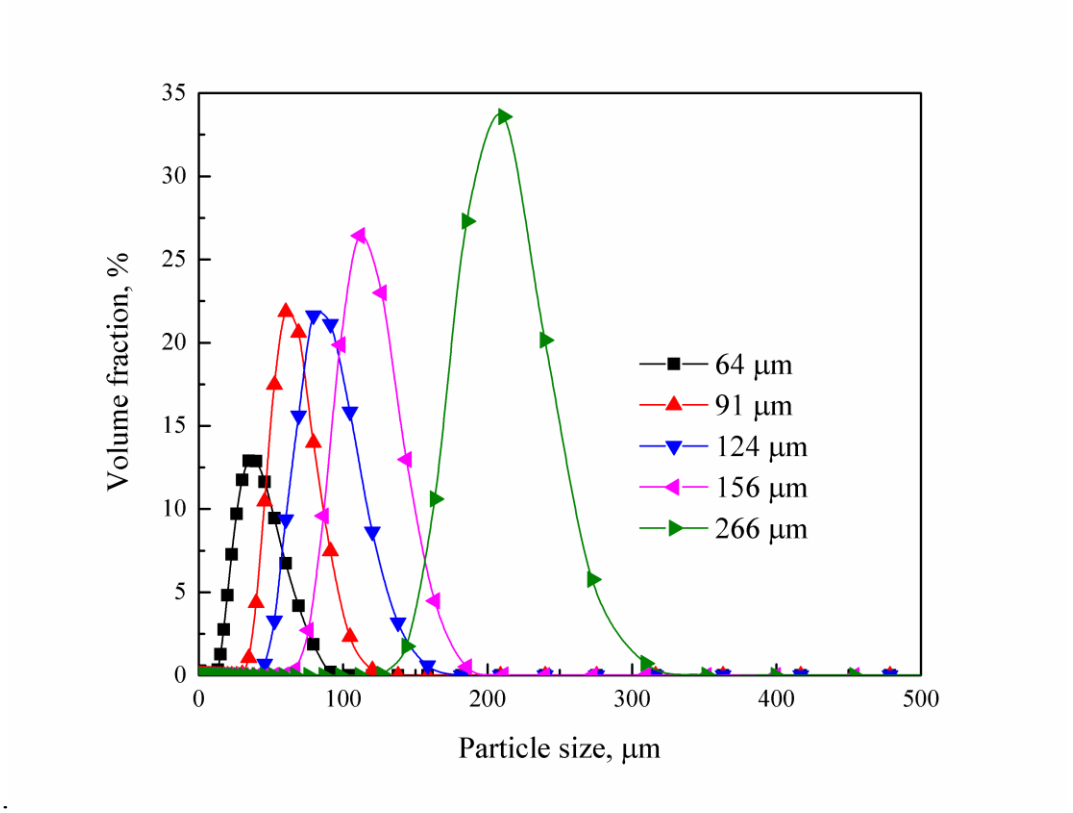
Volume fraction, %
Particle size, μm
64 μm
91 μm
124 μm
156 μm
266 μm
0
5
10
15
20
25
30
35
0
100
200
300
400
500

(a)

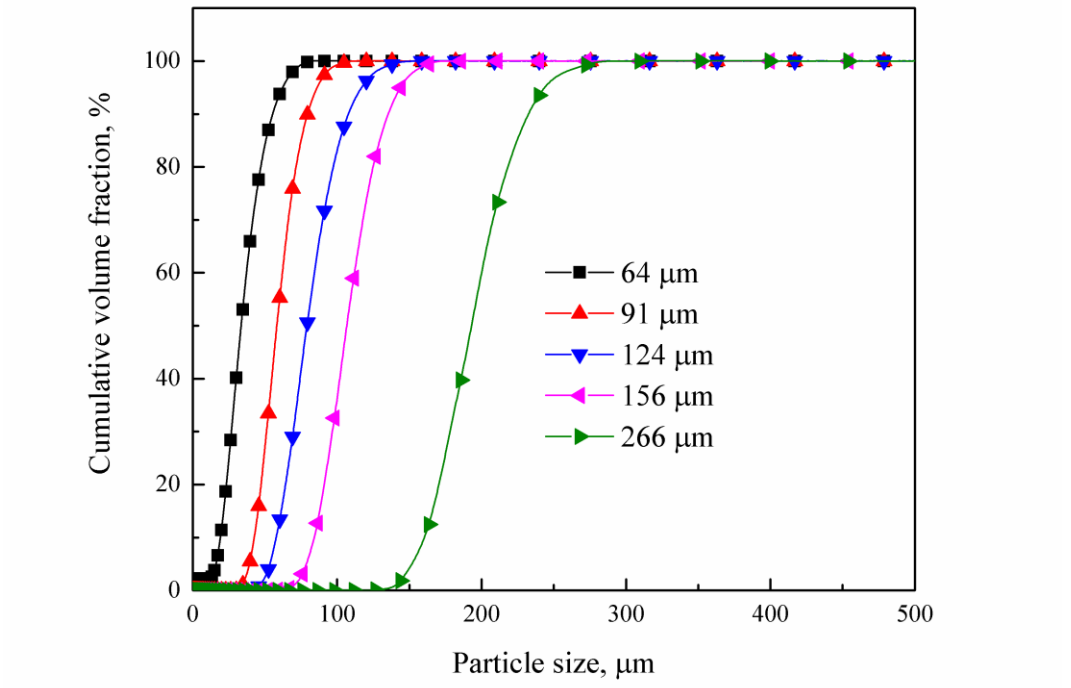
Cumulative volume fraction, %
Particle size, μm
64 μm
91 μm
124 μm
156 μm
266 μm
0
20
40
60
80
100
0
100
200
300
400
500

(b)

Figure 3.1. (a) Particle size distribution and (b) cumulative volume fractions of the samples used in the experiments. The legends correspond to the d_{90} of each sample.

3.2 Setup

A schematic illustration of the setup is shown in Figure 3.2. A capillary placed in a transparent rectangular perspex chamber (50 mm × 50 mm × 125 mm) is connected to a programmable micro-syringe pump. This pump is used to achieve fine control of air injection into the capillary, which is essential for repeatable bubble generation. To minimize disturbances, the entire setup was placed on a vibration-free table. The behavior of rising bubbles was recorded by a high speed camera, an Olympus i-speed LT with photographic objective and magnification lenses, at a capture rate of 1000 frames per second and a pixel resolution of 0.050mm/pixel. In addition, to analyze the coverage of particles on the bubbles, a second camera, a Canon EOS 600D, was set perpendicular to the Olympus camera; this camera gave a pixel resolution of 0.004mm/pixel and it guaranteed a close view and a clear image of the bubbles generated in the capillary. In both cases, LED back-lighting was used for illumination.

3.3 Experimental procedure

The experiments are divided into two parts: first, the influence of different particle coverages on the behavior of rising bubbles is investigated; the influence of particle size on the behavior of rising bubbles is then explored.

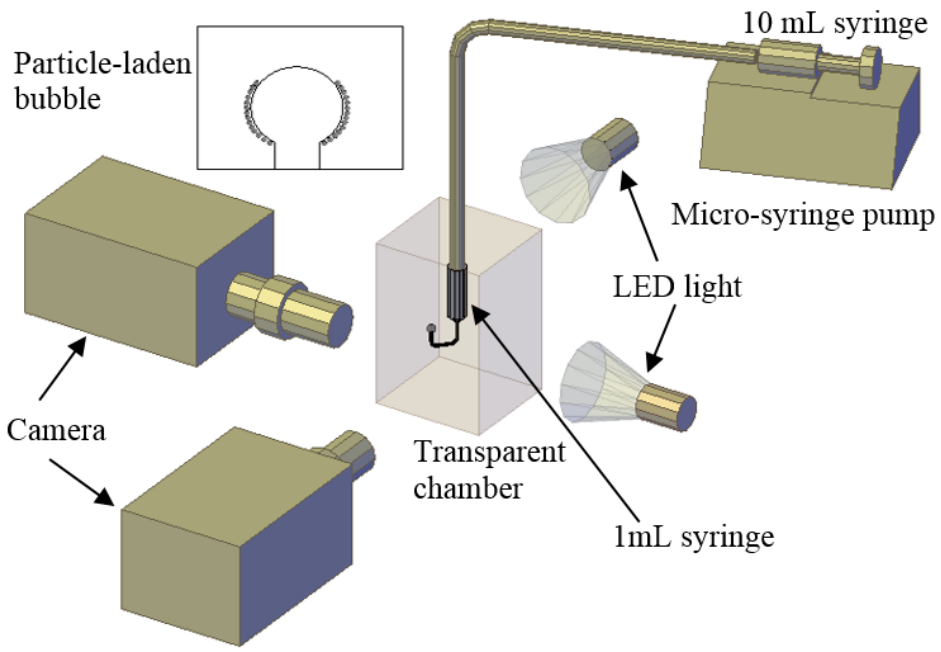

Figure 3.2. Experimental configuration to investigate the behavior of a rising air bubble, showing the setup including the cameras and light arrangement.

3.3.1 Assessing the influence of particle coverage

Two grams of glass beads particles were added into the transparent chamber, which was filled with 250 mL of deionized water (resistivity larger than 15 MΩ cm). TTAB, at a concentration of 1×10^{-6} M, was added and then mixed for 15 min with a magnetic stirrer at a speed of 700 rpm. Here the particles were always conditioned with the same concentration of collector, so the surface properties of particles are the same when they were attached to the bubbles. After the suspended particles settled down to the bottom of the chamber, a single bubble was formed at the tip of a stainless steel capillary needle (an inner diameter of 0.84 mm and an outer diameter of 1.27 mm) using a programmable syringe pump to control the air injection with high precision. The uncoated bubble was generated under the same liquid conditions (with solids settled down at the bottom).

For the uncoated bubble, the air injection rate was kept at 0.72 mL h^{-1} until the bubble was released. The diameter of the released uncoated bubbles was 2.8-2.9 mm. For the coated bubble, after the bubble grew up to a diameter of approximately 2.4-2.5 mm (with the grids on the camera used as a guide), the magnetic stirrer was turned on at a speed of 350 rpm so the bubble could be covered by particles. A stainless wire mesh (750 μm) was inserted below the capillary in order to guarantee that particles were evenly dispersed during the stirring process and also to decrease the chance of bubbles detaching from the capillaries due to excessive turbulence. Surface coverage was initially estimated visually and assessed at regular agitation time intervals. For reference, it took approximately 30s for the capillary pinned bubbles to be fully covered, with lower particle coverage requiring less time. The stirrer was turned off once a bubble was coated to the required fraction of surface coverage for each experiment.

Photographs were taken for detailed analysis in MATLAB as described in the next chapter. A settling time of 1 min was allowed for the liquid in the rig to become clear, after which additional air was injected to the capillary pinned bubble at a constant air flow rate of 0.72 mL h^{-1} in order to release it from the tip of the capillary. The diameter of the released coated bubbles was 2.9-3.0 mm, a little larger than the diameter of the released uncoated bubbles. The reason to explain is that the diameter is calculated from the rising bubble-particle aggregates, which is relatively bigger if more particles or coarser particle were attached to the bubble surface.

It is important to point out that each experiment consists of one bubble and it is not a continuous bubble generation process. Therefore there will be no important hydrodynamic effects such as those observed when multiple bubbles are present. Besides, the particles were settled down before repeating the full experiment, so there is no impact from the oscillation of the free surface nor effect from the particles. Moreover, since the maximum bubble diameter in the present experiment was less than 4 mm, the capillary was placed in the middle of the rig, the chamber size was large enough to make the wall effect on the motion and shape of a bubble

negligible. The rising bubble behavior was recorded and analyzed over a distance of 30 mm from the tip of the capillary. Footage of the rising bubble for each experiment was processed using ImageJ to obtain the position and dimensions of the bubbles. The tip of the needle was also photographed and used as a reference length to calculate the magnification of the optical system.

In this work, we refer to capillary pinned bubbles as those that were generated in the capillary and coated with particles, which become rising bubbles once detached from the capillary. For the experiments of investigating the influence of particle coverage on the behavior of rising bubbles, only the finest particles, meanwhile particles of size 1 with d_{50}=39 μm (d_{90}=64 μm) were used. The comparison of the influence of particles on the bubble velocity and shape change was carried out for the initial time period when the angle (θ) between the bubble's minor axis and its vertical moving direction was lower than 10°, which usually holds for the first 80 ms.

3.3.2 Assessing the influence of particle size

For the experiments of the influence of particle size on the behavior of rising bubbles, all the five particle types were used. The experiments were performed at a temperature of 20 °C under natural pH condition. The capillary pinned bubbles (2.8-2.9 mm in diameter) as well as the rising bubbles (diameter of 3.2-3.6 mm) were relatively larger compared to their counterparts which were used for the study of the influence of particle coverage. For attachment tests, particle coverage of capillary pinned bubbles at different times was investigated. For the experiments of rising bubbles, the bubbles in the capillary were initially half or fully coated and the settling time varied depending on the particle size. These experiments were carried out in triplicate. Further details were the same as described in the previous section.

Chapter 4 Image processing method for uncoated bubbles and particle-laden bubbles

This chapter introduces the procedure of image processing method in MATLAB and Image J. The rising behavior of uncoated bubbles and particle-laden bubbles are also compared.

4.1 Pendant drop method to calculate the particle coverage

The images of bubbles were analyzed for dimensional measurements first. The value of the pressure difference based on the shape of the bubble was calculated using the Young-Laplace equation [150], which relates the radii of curvature $R_1$and R_2, the surface tension σ, and the pressure difference ΔP across the curved liquid/gas interface:

$$\Delta P = (P_{int} - P_{ext}) = \sigma\left(\frac{1}{R_1} + \frac{1}{R_2}\right), \tag{4.1}$$

where P_{int} and P_{ext} represent the internal and external pressure, respectively. σ is the surface tension coefficient. This is shown schematically in Figure 4.1.

The exact fractions of bubble surface covered by particles in each experiment were calculated in this work using the pendant drop method [151,152], the equation of which was derived according to the Young-Laplace equation. Following the method of Yang et al. [152], the Equation (4.1) was converted to a set of three first-order differential equations formed by the spatial positions x and z and turning angle Φ of the bubble interface as a function of the arc length s of the bubble shape. With three boundary values $x(s = 0) = 0, z(s = 0) = 0, \Phi(s = 0) = 0$, the equations were solved numerically, assuming $R = R_1 = R_2$:

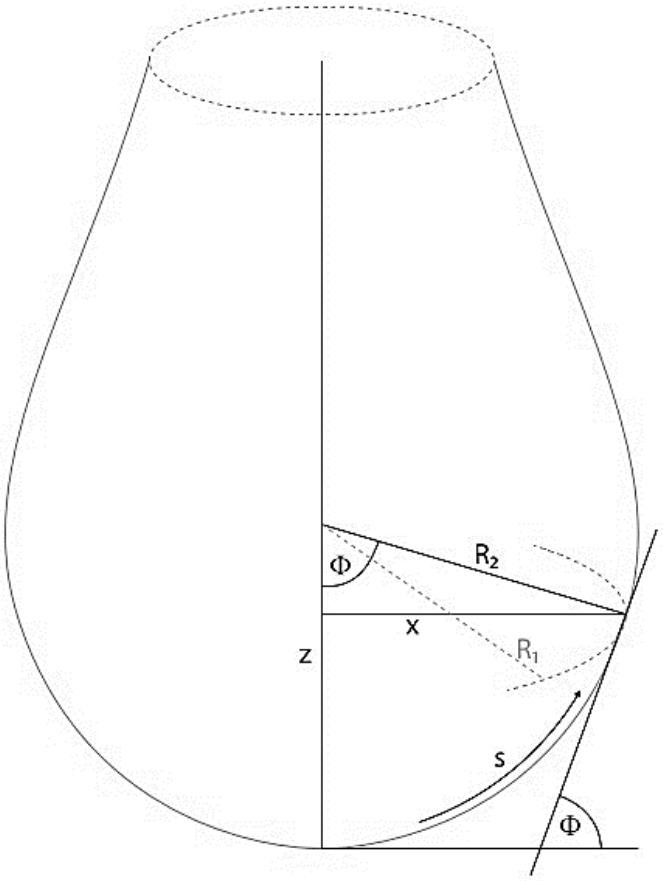

Figure 4.1. Schematic for the derivation of the Young-Laplace equation to obtain a fit to a bubble edge.

$$\frac{d\Phi}{ds} = -\frac{sin\Phi}{x} + \frac{2}{R} - \frac{\Delta\rho g z}{\sigma}, \tag{4.2}$$

$$\frac{dx}{ds} = cos\Phi, \tag{4.3}$$

$$\frac{dz}{ds} = sin\Phi. \tag{4.4}$$

First of all, the bubble was assumed symmetrical, and the images were rotated for the analysis. A series of the edge points on the right half of the rotated bubble was then detected. After that, the pendant drop equation model was fitted with the location of the edge points. The numerical fit of the bubble shape can yield the surface tension and the radii *R* of the bubbles.

By integrating the fitted pendant drop equation model, a 3-D representation of the bubble can be obtained, and according to the height of particles covering the bubble surface, the surface area of bubbles covered by particles can be calculated.

Figure 4.2 shows the bubble edge detection before and after coating with particles. Figure 4.3 compares the edge points of a bubble with the fitted pendant drop models. Firstly, the pendant drop model was fitted to the edge points of a bubble prior to (Model-uncoated) and after (Model-coated) it was covered with particles. However, the model fitted well with the edge points of the uncoated bubble but not with the coated one. Therefore, the diameter of the coated particles can not be neglected. In order to solve this problem, the point from which particle coating occurred was detected, as can be seen from Figure 4.3 (a) (blue circle). Afterwards, the edge points of the bubble coated with particles (Figure 4.3 (a) red dot line) were moved inside the bubble by a length equal to the diameter of the particles, and then a new fitting curve of the coated bubble was generated, as was shown in Figure 4.3 (b). The surface area of the bubbles was calculated by rotating the fitting model around the vertical axis. The covered area was determined by the average of the integrals of different heights of the particles covering the bubble, and particles being regarded as one layer evenly distributed onto the bubble surface without any aggregation.

It is important to note that once a bubble is released from the capillary, its surface area becomes larger and therefore the actual percentage of particle coverage has to be reassessed. Dividing the particle coverage obtained originally using the pendant drop method by the surface area of the released bubble yields the actual percentage of the surface area of the bubble that is covered by particles. During this process, the detachment of particles is negligible.

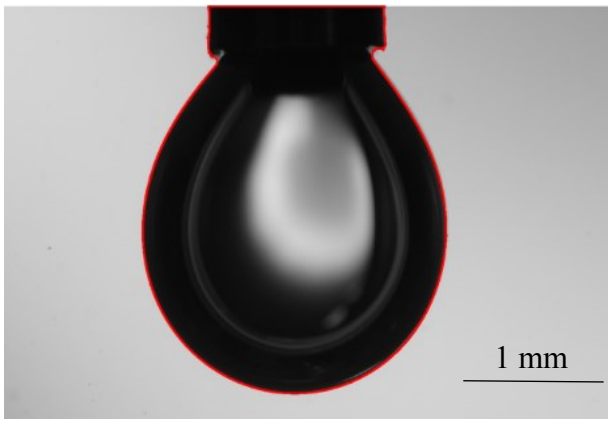

(a)

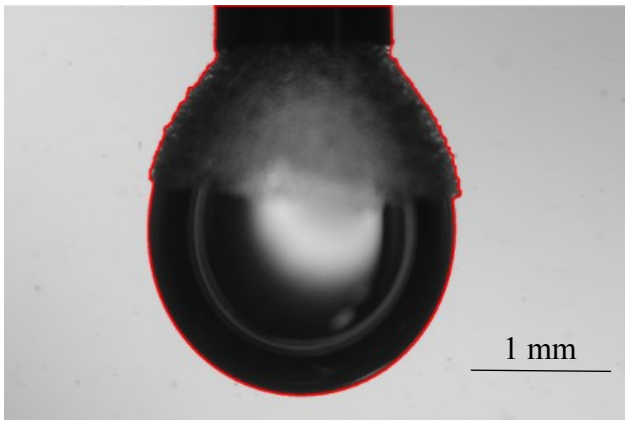

(b)

Figure 4.2. Images rotated for edge detection of a bubble (a) before and (b) after being coated with particles. The red line shows the detected edge points.

4.2 Sessile drop method to calculate the particle coverage

The Young-Laplace equation was also modified to adapt to the bubbles generated from capillaries at the top, and the fractions of bubble surface covered by particles can be calculated using a sessile drop method [152]. This image processing method combined with particle attachment tests can be used as a simple way of gaining additional information not currently available from typical collector performance tests. The detailed information about the experiments and the results are given in Appendix B. The theoretical bubble shape was also

governed by the same Young-Laplace equation. Further details can be referred to the previous section of pendant drop method. The equation is shown schematically in Figure 4.4.

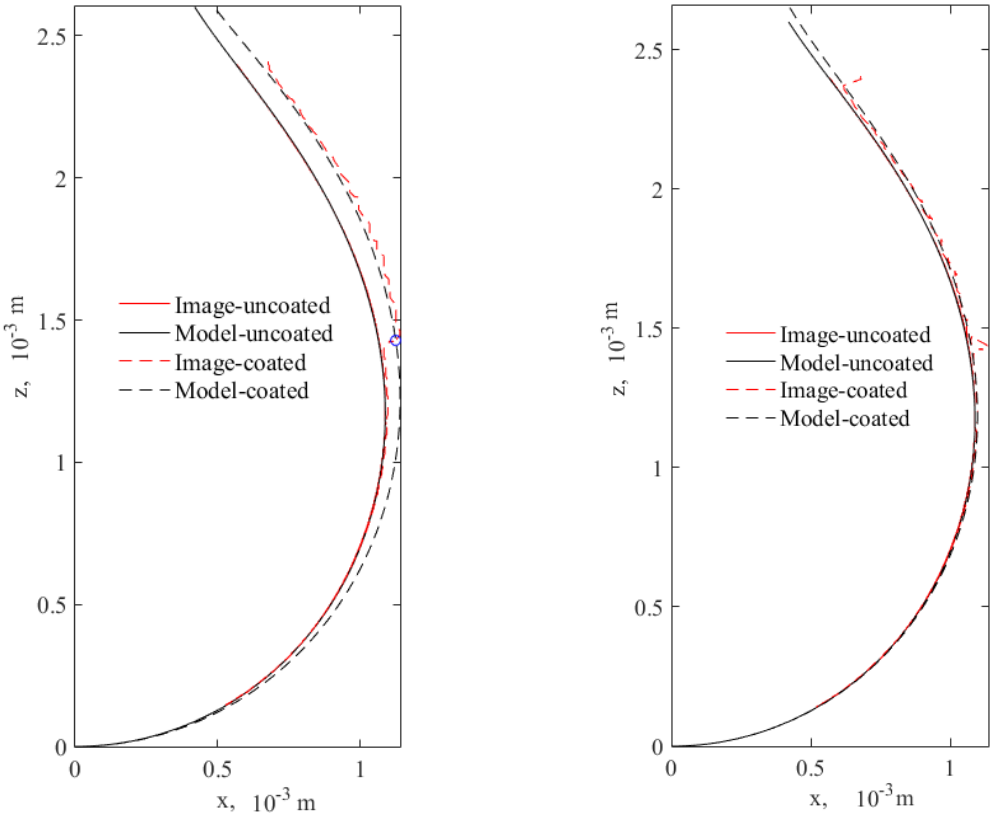

(a) (b)

Figure 4.3. Curve fitting to the uncoated and coated bubble edge points: (a) detection of the point where particles begin to coat the bubble, marked here with a blue circle; (b) fitting after the particle diameter is reduced.

Equation (4.1) can be recast to a group of three first order sessile drop differential equations [153]:

$$\frac{d\Phi}{ds} = -\frac{sin\Phi}{x} + \frac{2}{R} + \frac{\Delta\rho g z}{\sigma}, \tag{4.5}$$

$$\frac{dx}{ds} = cos\Phi\,, \tag{4.6}$$

$$\frac{dz}{ds} = sin\Phi\,. \tag{4.7}$$

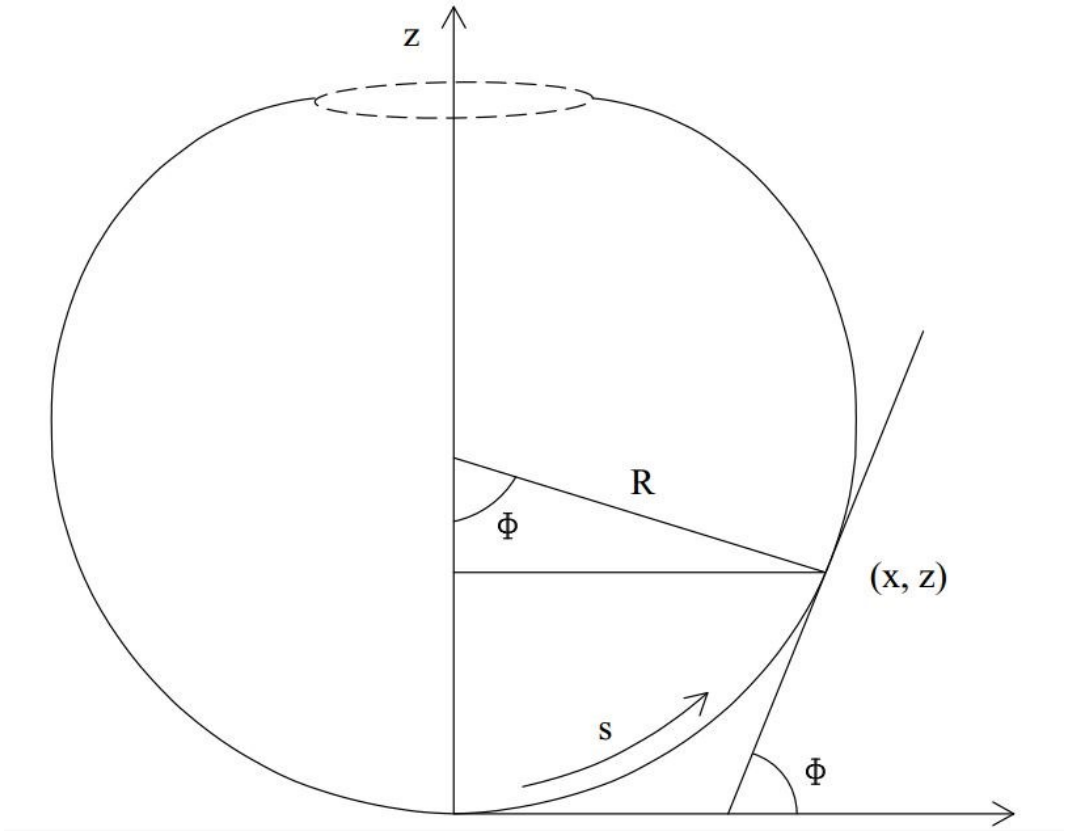

Figure 4.4. Schematic for the derivation of the Young-Laplace equation to obtain a fit to a bubble edge.

The relevant parameters are similar to those of the pendant drop method. Gravity tends to elongate a pendant drop or bubble but flatten a sessile drop or bubble, therefore the only difference of sessile drop method from pendant drop method is the value of z, as can be seen from Equation (4.5). For the calculation of the bubble surface area covered by particles, the bubble was assumed as symmetry, and a series of the edge points on the right half of the bubble were detected. After that, the sessile drop equation was fitted with the bubble edge points. The surface tension and the radii of the bubbles can thus be obtained from the numerical fit. Figure

4.5 Figure 4.5 illustrates the bubble edge points detected before and after the attachment of chalcopyrite. Figure 4.6 shows the sessile drop equation models fitted to the extracted bubble edge points. Firstly, the fitting model was rotated around the vertical axis, to achieve a 3D representation of the bubble. The surface area of the uncoated bubbles was calculated. For the coated bubble, to take into account the influence of particle diameter on the calculation, an average of the coated model and the corresponding uncoated model was used for the calculation of the surface area. The surface area covered by particles was determined taking into account the 3D shape of the bubble and also according to the boundary of the particles covering the bubble (so that the assumption of a straight boundary is not needed). Surface coverage, i.e. the percentage of the surface area covered by particles, was then obtained by dividing the covered area by the total surface area of the bubble.

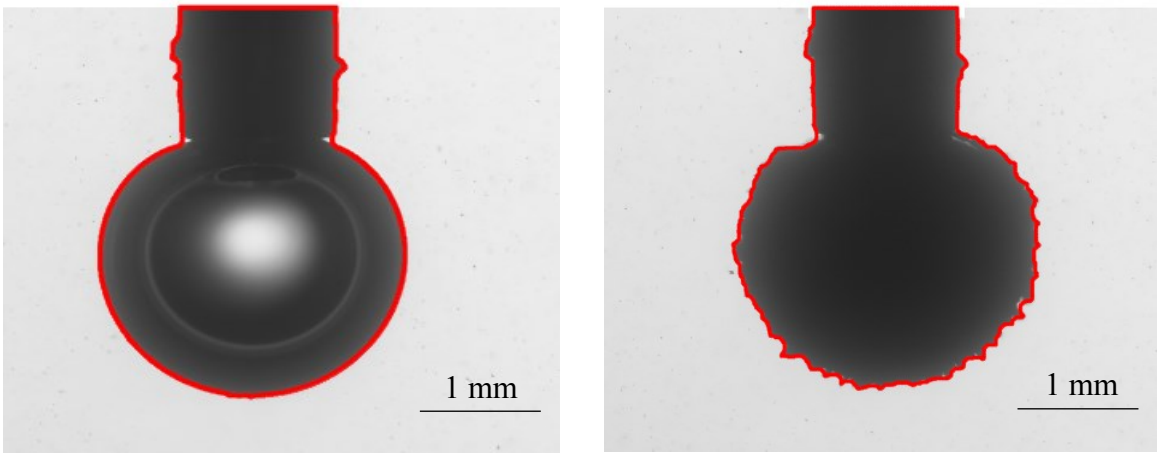

(a) (b)

Figure 4.5. Images for edge detection of a bubble (a) before and (b) after being coated with particles. The red line shows the detected edge points.

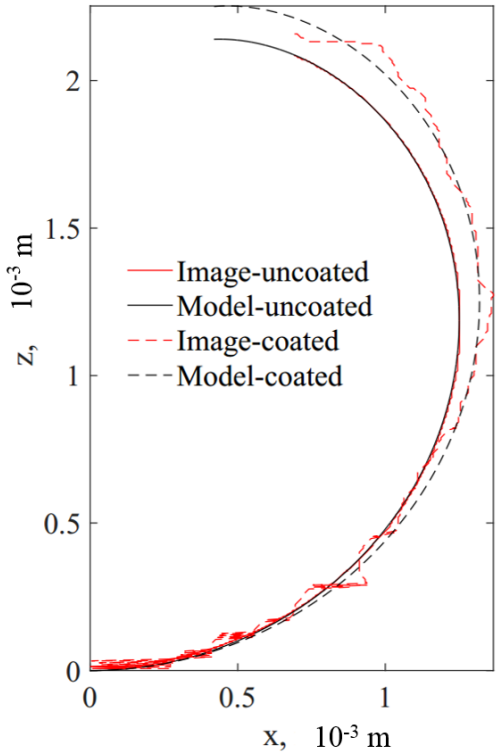

Figure 4.6. Curve fitting to the uncoated and coated bubble edge points; the solid lines correspond to the uncoated bubble edge from the image (red) and the model (black) and the dotted lines to the coated bubble edge from the image (red) and the model (black).

4.3 Bubble velocity and aspect ratio calculation

Figure 4.7 shows a schematic illustration of the bubble image analysis procedure and how the diameters a and b of the bubble are determined. Assuming the bubble was an oblate spheroid (symmetrical about the rising direction), the bubble equivalent diameter, d, was calculated from the diameters a and b, the bubble diameters parallel and perpendicular to its vertical moving direction, respectively:

$$d = \sqrt[3]{ab^2}\,. \tag{4.8}$$

The aspect ratio (AR), a parameter that reflects the dynamic behavior of rising bubbles, was calculated as the ratio between the diameters b and a [120]:

$$AR = \frac{b}{a}. \tag{4.9}$$

It has been reported that with an increase in the concentration of frother, bubbles tend to be more spherical and bubble rise velocity decreases. Oscillations in aspect ratio and velocity for uncoated rising bubbles have been found to be inversely related [121].

Here, only the vertical direction of the bubble motion was considered. The rise velocity (u) was calculated from the vertical central position of the bubble over two consecutive frames ($i+1, i$) as:

$$u = \frac{y_{i+1} - y_i}{\Delta t}, \tag{4.10}$$

where Δt is the time interval between two frames (1ms for the recorded data).

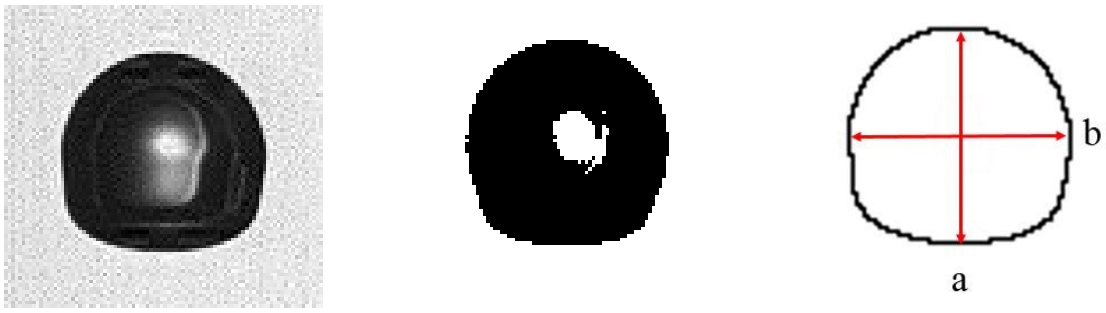

(a) (b) (c)

Figure 4.7. Image analysis procedure: (a) bubble image, (b) image after threshold applied, (c) edge detected and diameters a and b that are used to determine the aspect ratio.

The bubble releasing point was 30 mm below the air and liquid interface. The zero time point was taken to be the point one frame prior to the release of a bubble. The acceleration ($\bar{a}$) was calculated from the velocity change of the bubble over two consecutive frames ($i+1, i$) as:

$$\bar{a} = \frac{u_{i+1} - u_i}{\Delta t}. \tag{4.11}$$

4.4 Comparing the behavior of uncoated bubbles with particle-laden bubbles

This section investigates the behavior of rising bubbles which were initially uncoated or initially fully coated when they were attached to the capillaries. The finest particles (Size 1) were used for the experiments.

4.4.1 Velocity and aspect ratio (change) of uncoated bubbles and particle-laden bubbles

Figure 4.8 (a) and Figure 4.8 (b) show the aspect ratio of an uncoated bubble and a coated bubble (with 59.9% surface coverage), respectively. It is clearly seen that after being released from the capillary, the oscillation patterns of both bubbles were similar over the first 30 ms, afterwards, particles exerted a significant effect on the shape stability of the coated bubble. Apart from some minor decrease due to oscillations, the aspect ratio of the uncoated bubble rose steadily until it reached the maximum value of 2.82 at 66 ms, after which the bubble aspect ratio began to decrease due to the rotation of the bubble. For the coated bubble, the aspect ratio firstly increased to 1.29 over the first 11 ms, and then decreased to 1.13 at 18 ms prior to reaching the peak value of 1.39 at 30 ms. After that, the aspect ratio experienced a minor decrease and then changed slowly afterwards. In terms of velocity, as is shown in Figure 4.9, there are more data point frames for the coated bubble than for the uncoated bubble within the same viewing area, due to the rising velocity of the former being lower. For the uncoated bubble, its velocity rose to 0.212 mm/ms at 17 ms and then oscillated within a range of 0.166 mm/ms to 0.251 mm/ms until 86 ms, after which the velocity decreased. The coated bubble, on the other hand, firstly rose to a velocity of 0.162 mm/ms at 20 ms, it then experienced a minor decrease prior to rise again to 0.183 mm/ms at 34ms. After that, although with small

variation, the velocity showed an overall stable tendency until 95 ms, after which it decreased due to the rotation of the bubble.

The current set up does not permit tracking of the bubble motion beyond 180 ms. According to the literature [120], bubble velocity and aspect ratio periodically reach top stable values and then slow down, the reason is mainly due to the bubble rotation (i.e., a > b). The overall amplitude of the velocity is mainly determined by the overall hydrodynamic forces. The comparison of the influence of particles on the bubble velocity and shape change was carried out for the initial time period when the angle (θ) between the bubble's minor axis and its vertical moving direction was lower than 10°, normally during the first 80 ms. In terms of the bubble motion being well developed, we can observe in Figure 4.9 that the velocity of the bubble already reached the periodic top stable value. Overall, the coated bubble showed a lower aspect ratio and velocity compared to the uncoated bubble. Without particles, bubble shape and velocity pulsated more strongly.

To explore the relationship between the parameters discussed above, the rising velocity (both for the uncoated bubble and the coated bubble) is plotted against its corresponding aspect ratio, as shown in Figure 4.10. The graph of the coated bubbles was zoomed in to make the results more visible. Overall, the rising bubble velocity was directly correlated to its aspect ratio, i.e., when the bubble shape becomes more spherical, the bubble slows down and vice versa. This has been shown before for uncoated bubbles [120], but had not been explored for particle-laden bubbles. The results confirm that the overall behavior is similar although the distribution of aspect ratio values for the uncoated bubble was wider than that of the coated bubble.

Having high velocities for the high aspect ratios and vice versa is counterintuitive as high aspect ratios are associated with high drag configurations. The reason for this apparent contradiction is because this is a dynamic situation in which bubbles are oscillating in terms of aspect ratio. At the maximum aspect ratio, the bubble will be experiencing a deceleration and

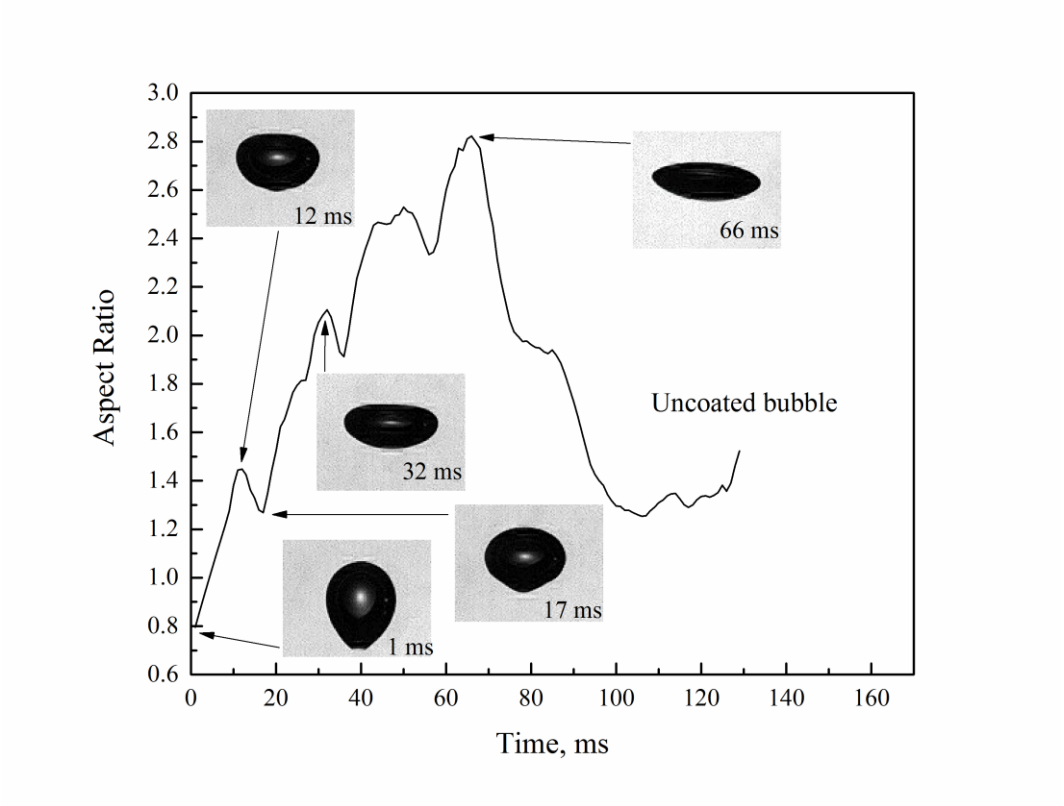

(a)

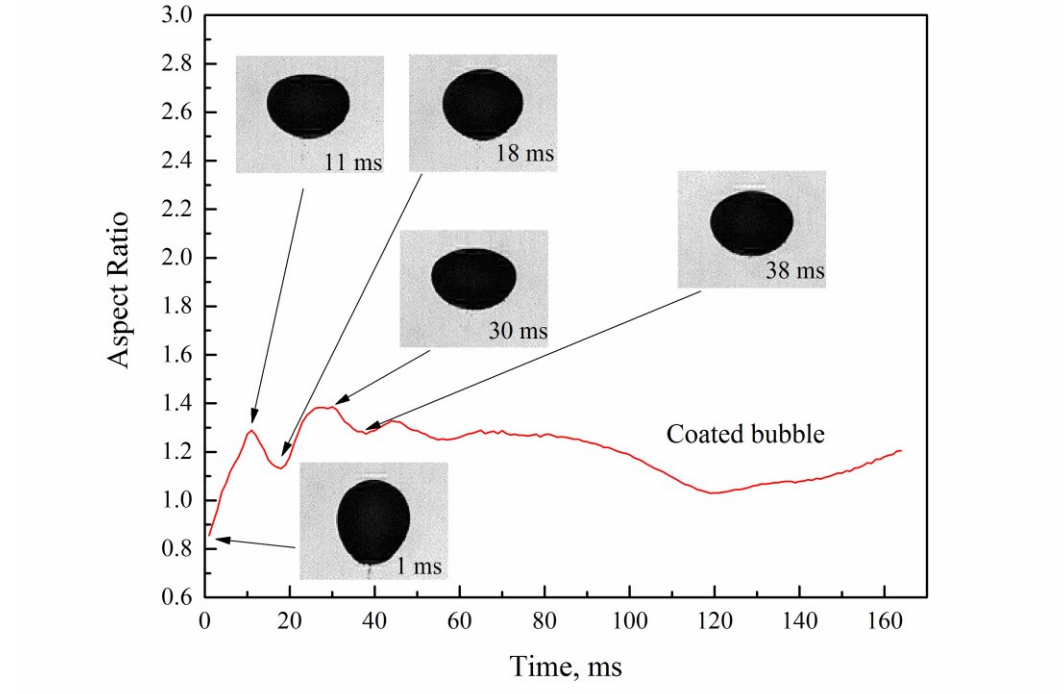

(b)

Figure 4.8. Evaluation of the aspect ratio of (a) uncoated bubble and (b) coated bubble with time.

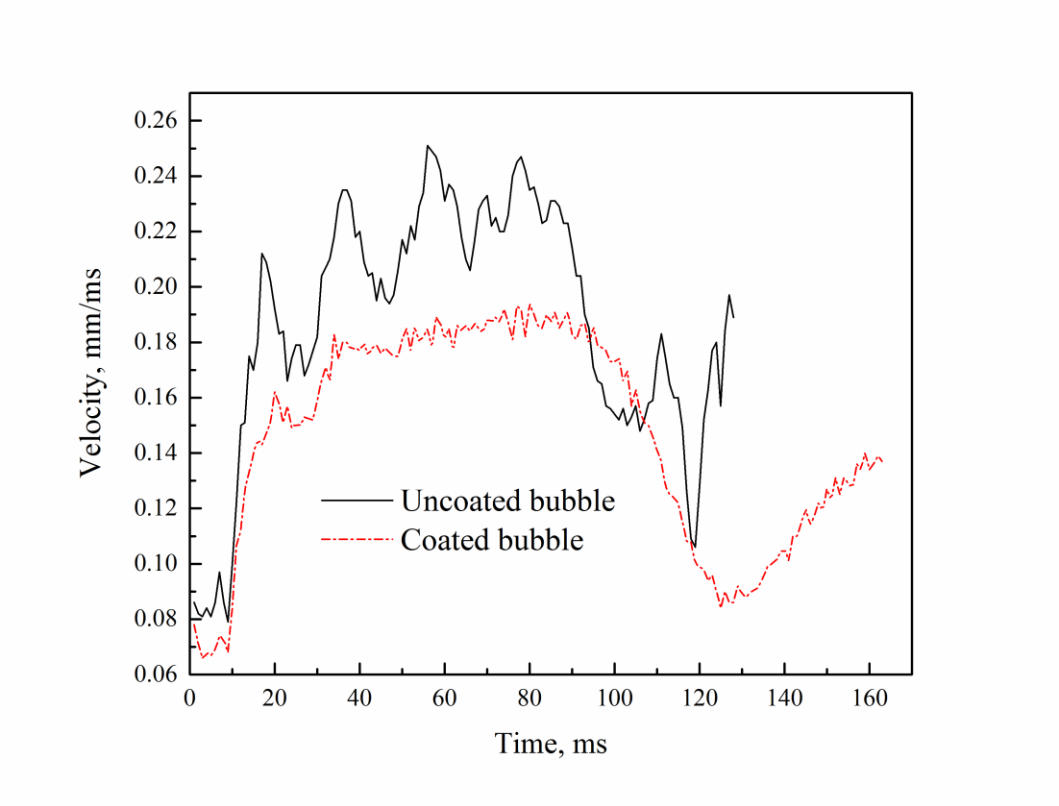

Figure 4.9. Evaluation of the velocity of uncoated bubble and coated bubble with time.

will return to a round shape and lower drag, with this oscillation then repeating itself. These will be explained in more detail later.

4.4.2 Comparing the acceleration of uncoated bubbles with particle-laden bubbles

The acceleration of the rising bubbles was calculated and the results are shown in Figure 4.11 (a). The noise and the high frequency of the acceleration variation in the raw data makes it difficult to analyze, the acceleration difference between the uncoated bubble and the coated bubble can be seen more clearly after applying a moving-average filter. This is done in Figure 4.11 (b), in which the averages of each six continuous acceleration data points (window size 6) are shown. As can be seen, the acceleration amplitude of the uncoated bubble was higher than that of the coated bubble, which indicated that the velocity variation of the coated bubble was dampened due to the attached particles.

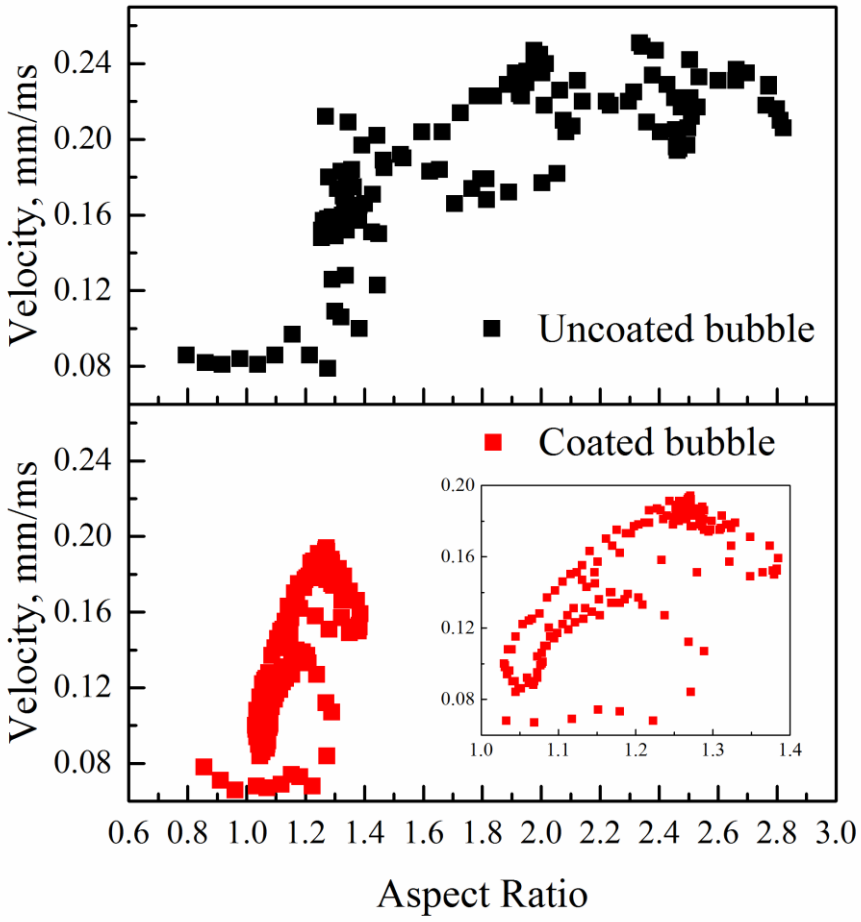

Figure 4.10. Velocity vs. Aspect ratio of the uncoated bubble and coated bubble.

Further to the previous discussion. The acceleration and aspect ratio of the uncoated bubble and coated bubble are plotted and shown in Figure 4.12 (a) and Figure 4.12 (b), respectively, after applying a moving-average filter for the acceleration (window size 6). Overall, the acceleration and the aspect ratio were inversely correlated: a local peak value of acceleration corresponded to a local minima of aspect ratio. It can be concluded that high aspect ratio causes high drag which will decelerate the bubble motion and vice versa.

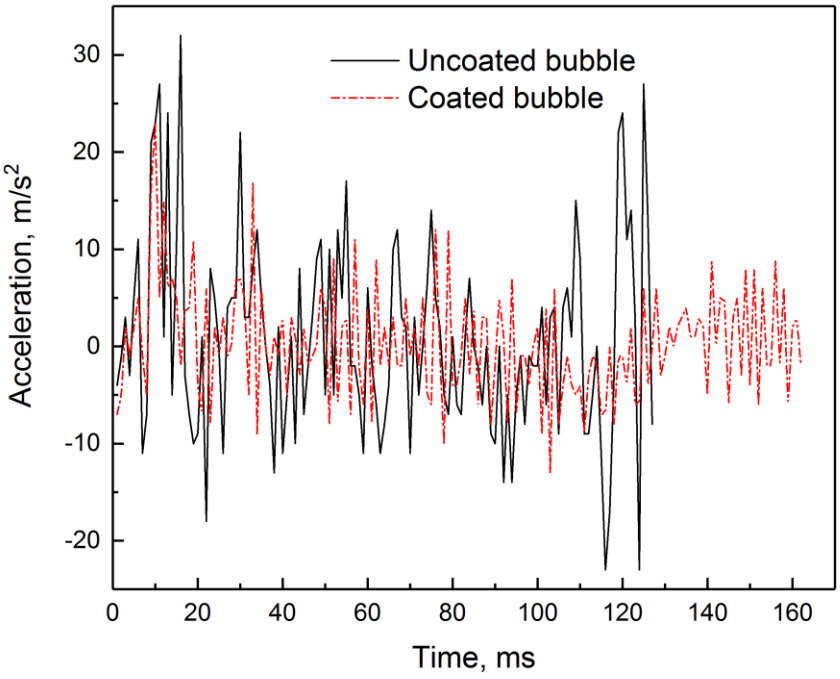

(a)

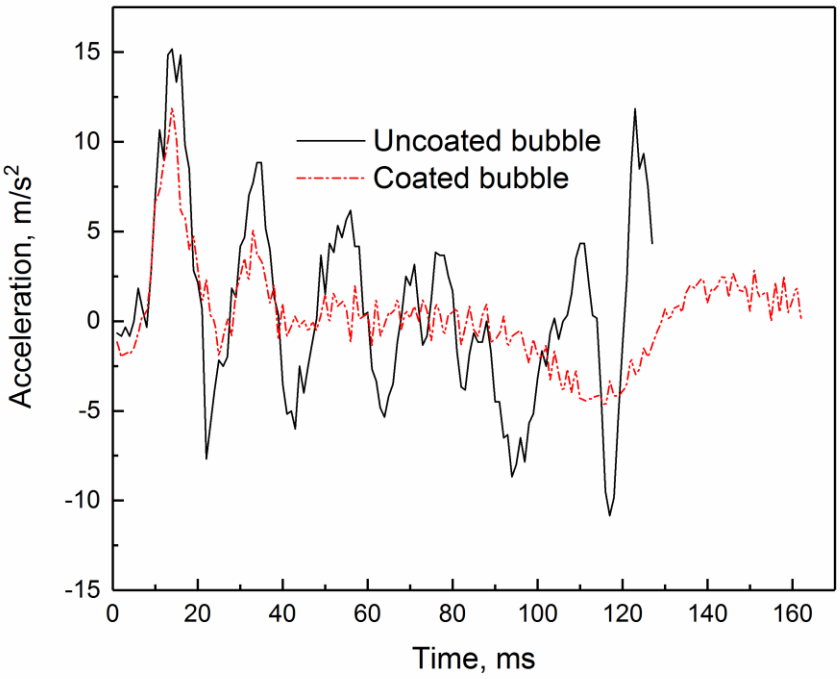

(b)

Figure 4.11. Acceleration of the uncoated and coated bubbles: (a) raw data, (b) data processed with a moving-average filter (window size 6).

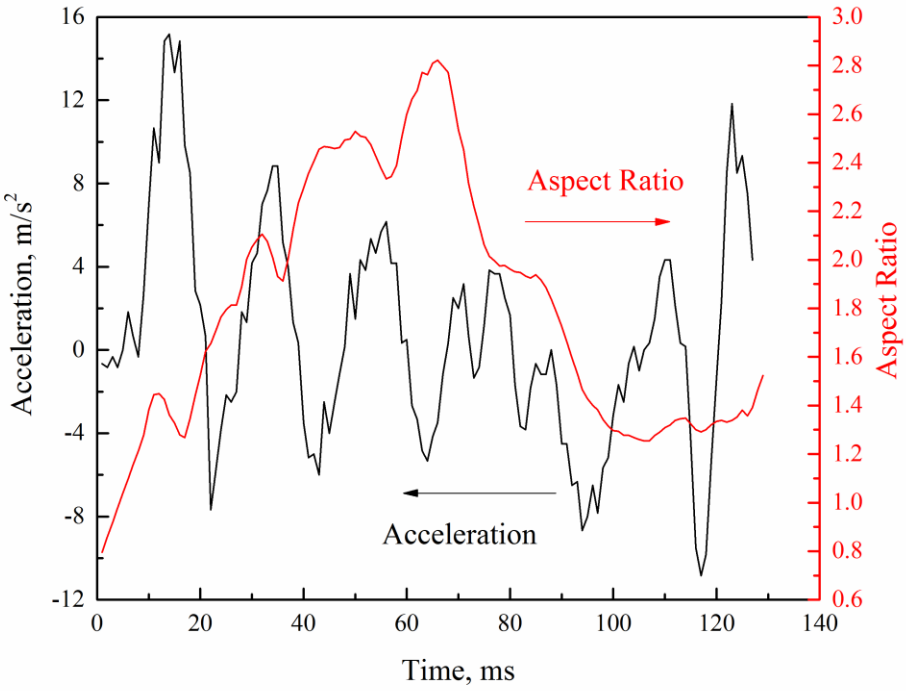

(a)

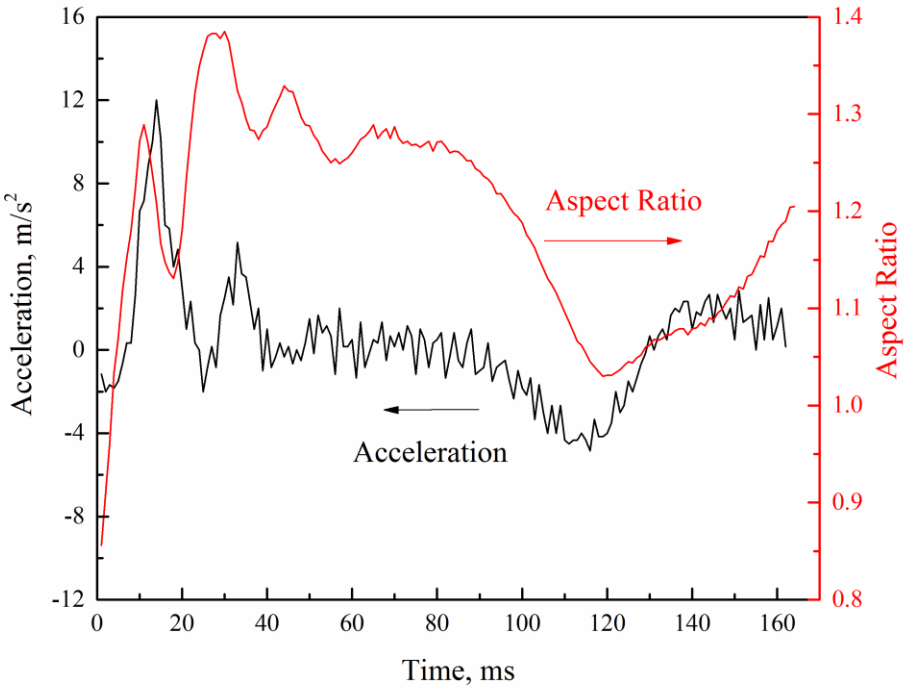

(b)

Figure 4.12. Acceleration and aspect ratio of the (a) uncoated bubble and (b) coated bubble. Original data of acceleration processed with a moving-average filter (window size 6).

For more in-depth analysis, the acceleration and the aspect ratio change (aspect ratio variation over two consecutive frames) of the uncoated bubble are also compared and shown in Figure 4.13 (a), after applying a moving-average filter for both data (window size 6). As can be seen, the acceleration and the aspect ratio change were also inversely correlated: each peak value of acceleration corresponded to a local minima of aspect ratio change. The same trend can be seen for the coated bubble, as shown in Figure 4.13 (b). Both the acceleration and the aspect ratio change of the coated bubble were smaller compared to those of the uncoated bubble.

4.5 Summary

The image processing methods based on MATLAB and Image J are introduced in this chapter. The pendant drop model is used and fitted to the edge points of the bubbles to calculate their particle surface coverage. Similarly, sessile drop method is used for the calculation of chalcopyrite coverage on the bubbles, the results of which are shown in the Appendix B. The bubble velocity, aspect ratio as well as the acceleration for rising bubbles which are initially uncoated and fully coated are also compared. It is shown that both the velocity and the aspect ratio of bubbles decrease when the bubble surface is covered by particles. The particles exert a strong damping effect on the amplitude of the oscillation observed in bubble velocity, acceleration and aspect ratio. In general, the rising bubble velocity is directly correlated to its aspect ratio, regardless of whether the bubble is coated or not. The acceleration and the aspect ratio and its change are found to be inversely correlated: each peak value of acceleration corresponds to a local minimum value of the aspect ratio (change) and vice versa. The more comprehensive study and detailed information with regard to bubbles coated with different levels of particles and the relevant forces analysis will be discussed in the next chapter.

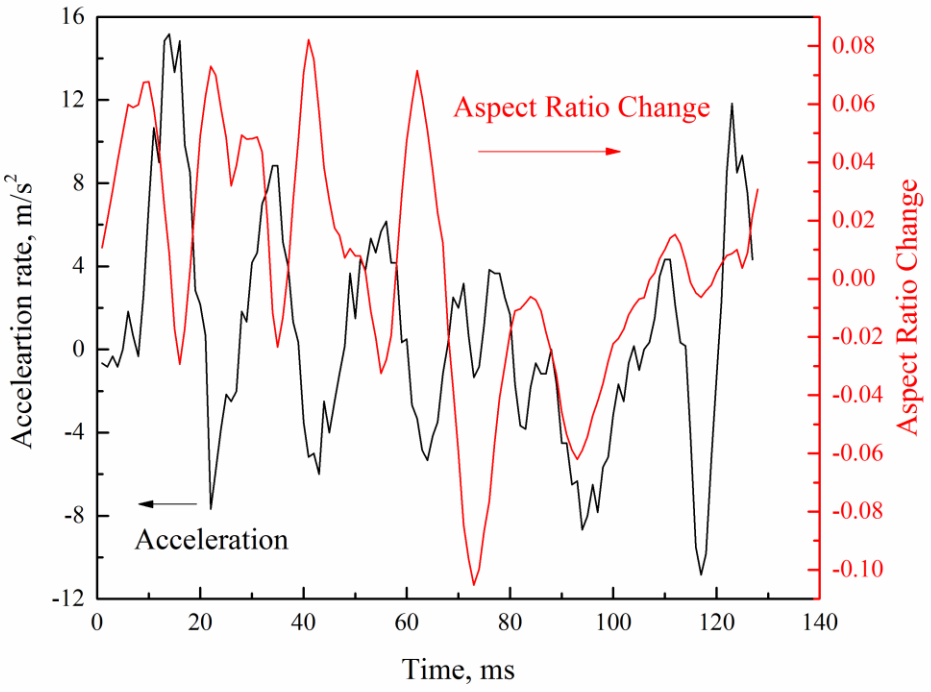

(a)

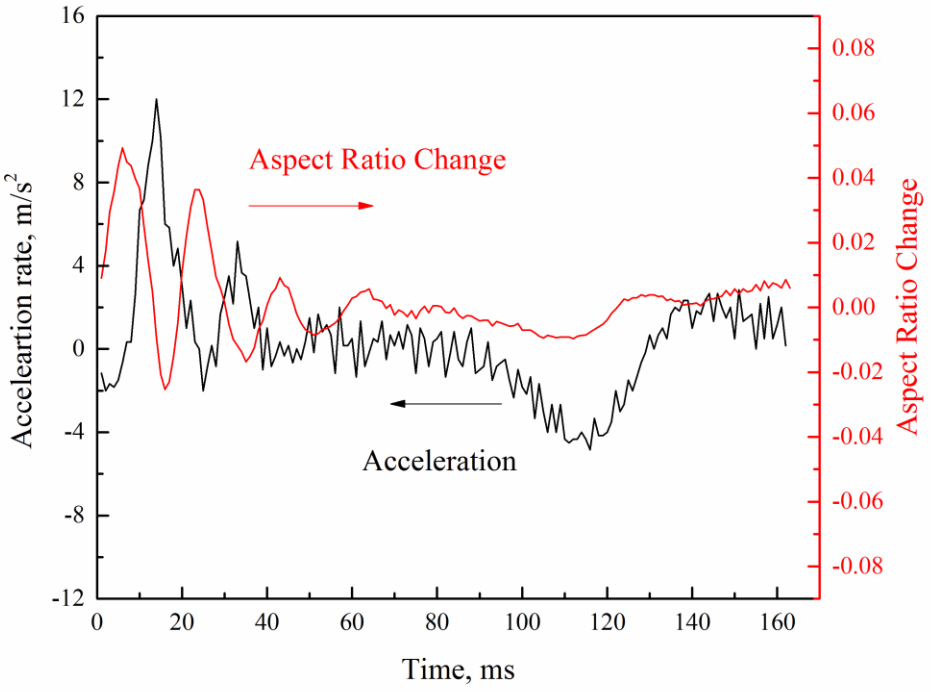

(b)

Figure 4.13. Acceleration and aspect ratio change of the (a) uncoated bubble and (b) coated bubble. Original data processed with a moving-average filter (window size 6).

Chapter 5 Influence of surface coverage of particles on rising particle-laden bubbles

This chapter investigates the influence of different particle coverages on the rising behavior of uncoated bubbles and particle-laden bubbles.

5.1 The reliability of experimental data

In order to evaluate the reliability of the experiment results, the rising behavior of the uncoated bubble and initially fully coated bubble were conducted in triplicate. The shooting frequency was 1000 fps and the time interval between two consecutive frames was 1 ms. Note that for intermediate levels of coverage, achieving exact values in repeats is challenging. However, it would be expected that the repeatability shown for the uncoated and initially fully coated bubbles would be representative of all the other intermediate levels. The velocity and the aspect ratio of uncoated and coated bubbles were evaluated and summarized in Figure 5.1 and Figure 5.2, respectively. It is clear that all the data show good repeatability, particularly for data before 80 ms, which is the range of interest for this study. This means that the data obtained for bubbles with intermediate levels of coverage can adequately represent the actual experimental results.

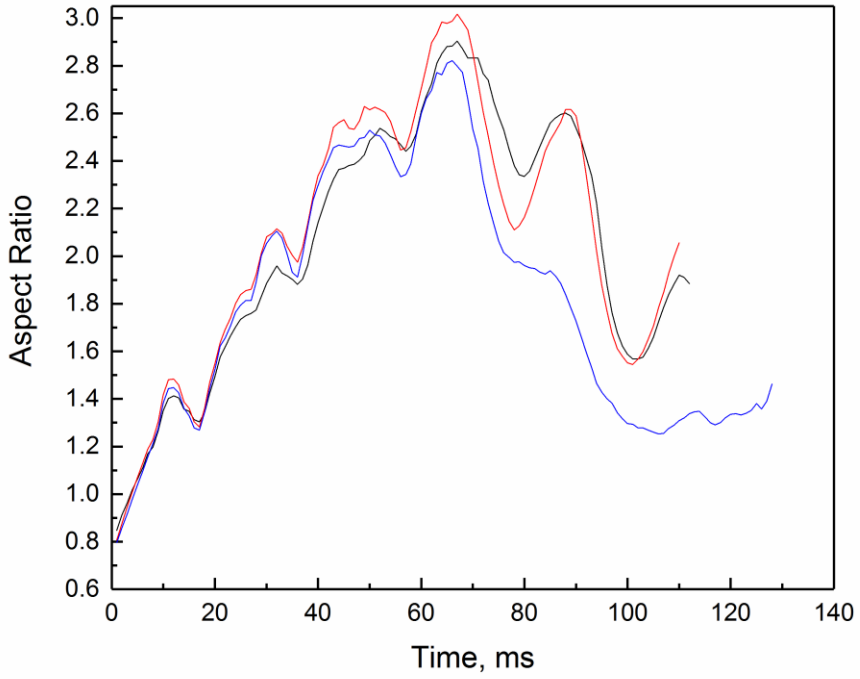

(a)

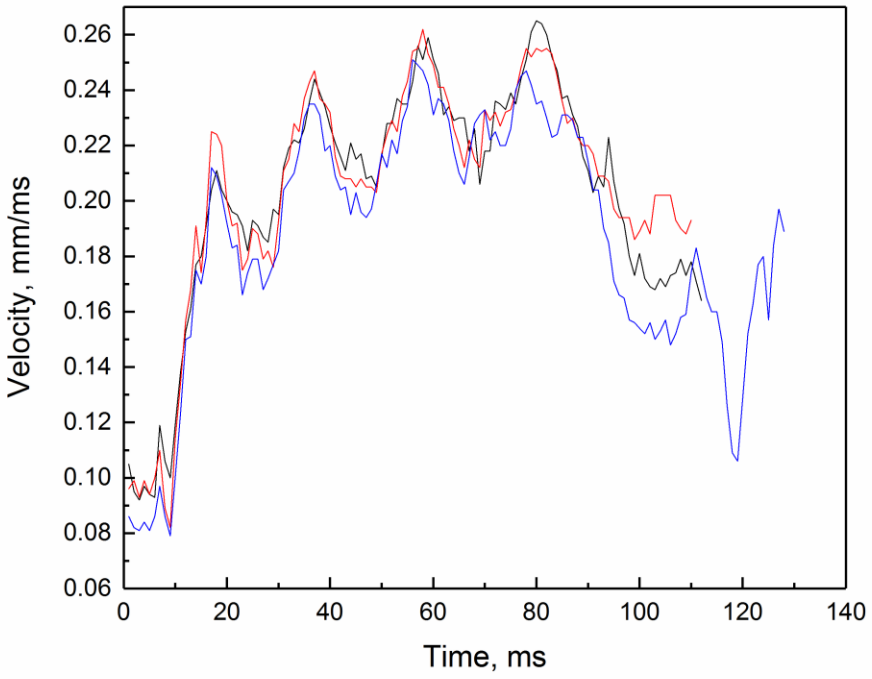

(b)

Figure 5.1. (a) Aspect ratio and (b) velocity of uncoated bubbles after release (from three measurements).

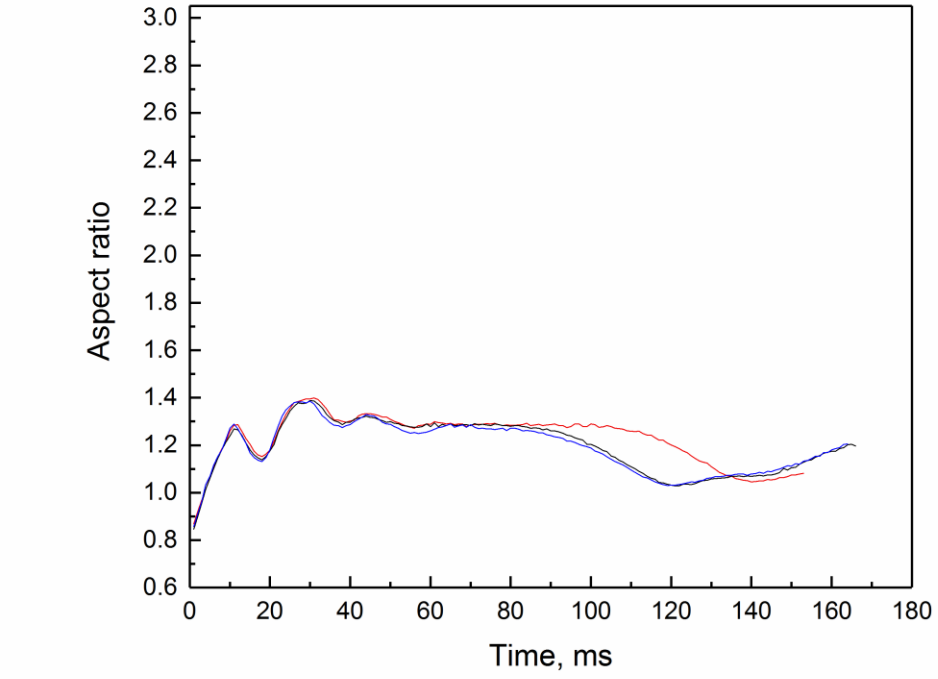

(a)

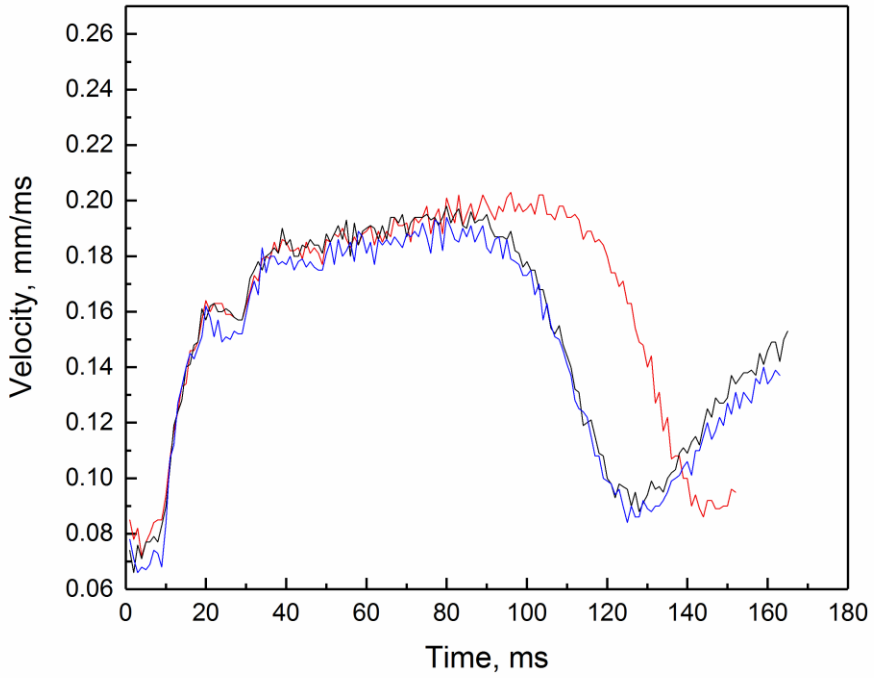

(b)

Figure 5.2. (a) Aspect ratio and (b) velocity of coated bubbles after release (from three measurements).

5.2 Influence of particle coverage on the velocity and aspect ratio change of rising particle-laden bubbles

To explore the effect of particle surface coverage on bubble behavior, bubbles with seven different levels of particle coverage were produced. As explained in Section 4.1, to achieve a quoted level of coverage the bubbles are initially "fully" coated at a size smaller than the desired size. Additional air is then added to both increase the bubble size and decrease the percentage of particle coating. This additional air also induces bubble release. Figure 5.3 shows those bubbles attached to the capillary, which once released resulted in the following percentages of surface coverage: 0.0%, 17.9%, 26.5%, 31.9%, 48.0%, 57.9% and 59.9%. Values for bubble aspect ratio and rising bubble velocity are compared in Figure 5.4 and Figure 5.5, respectively. The diameter of the released uncoated bubbles was 2.8-2.9 mm, and the diameter of the released coated bubbles was 2.9-3.0 mm. It should be noted that the diameter is calculated from the rising bubble-particle aggregates, which is relatively bigger if more particles were attached to the bubble surface.

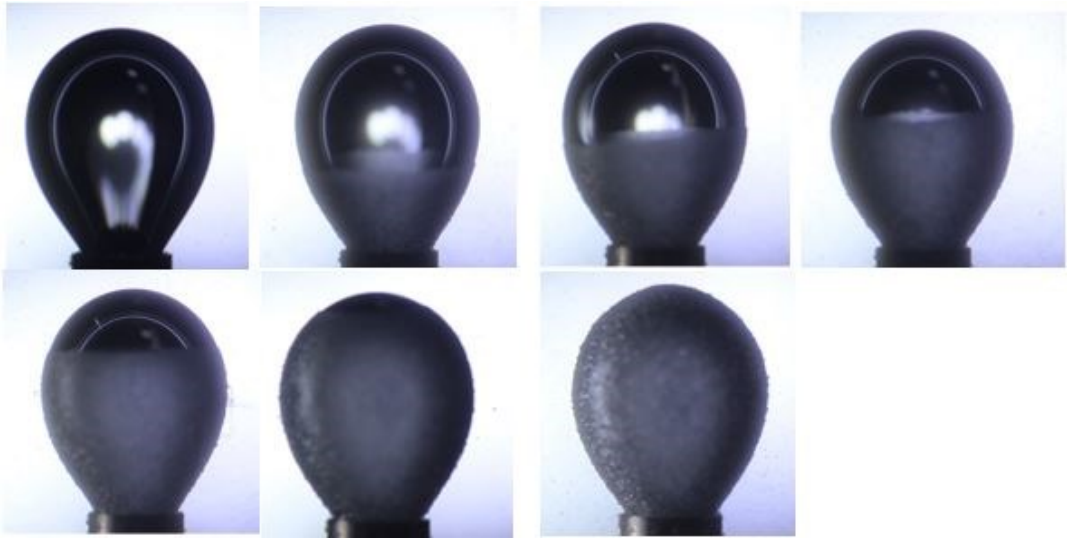

Figure 5.3. Different fractions of bubbles covered by particles.

As can be seen from Figure 5.4, there are no observable difference of the oscillation period of bubbles coated with different levels of particles. For values of surface coverage below 50%, the oscillation trend, shown in Figure 5.4, appeared to be similar in frequency but different in amplitude over the first 85 ms. The uncoated bubble showed larger values of aspect ratio (from 0.80 to 2.82) than particle-laden bubbles. The presence of particles clearly stabilized the bubble shape, particularly dampening the shape oscillation amplitude. This damping effect was more obvious when the particle surface coverage was higher (i.e., surface coverage higher than 50%).

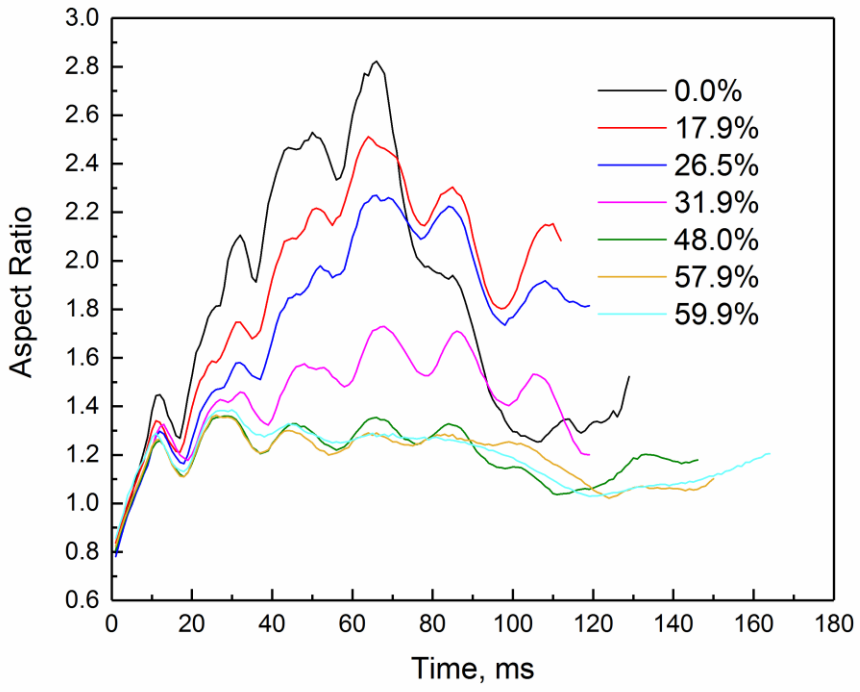

Figure 5.4. Aspect ratio as a function of different fractions of bubbles covered by particles.

Figure 5.5 quantifies how the bubble velocity changed as the bubble rose at different levels of particle coverage. Overall, the bubble velocity decreased with the increase in surface coverage. The velocities of bubbles with the three lowest levels of surface coverage followed the same oscillation trend over the first 85 ms. Oscillation amplitude of the velocity was more noticeably damped for surface coverages of 48.0%, 57.9% and 59.9%. Nevertheless,

comparing Figure 5.4 and Figure 5.5, the overall correlation between aspect ratio and velocity oscillation was maintained: with a higher proportion of particles coating the surface of a bubble, the bubbles tended to have lower aspect ratio and velocity. These results thus extend previous findings for uncoated bubble dynamics [120,121] to different levels of particle coverage.

Bubble dynamics is an important research area of fluid dynamics which has been widely studied. For uncoated bubble rising in a solution with surfactant, the surfactant moves off the bubble top and accumulates at the bottom part of the bubble, which induces a Marangoni tangential shear stress or shear force on the bubble surface. This force induces a less mobile bubble surface, and therefore, the drag force on the bubble due to this reduced mobility increases, which finally dampens bubble deformation and slows down the bubble rising velocity [4,154]. For coated bubbles in this study, the bubble oscillation amplitude decreases with increased particle coverage, although the oscillation pattern is similar. Particles also move around the bubble and accumulate at the bubble rear, making the bubble less deformed and retarding its motion. This implies that the influence of particles on the bubble motion is not only from the bubble mass force, but also from the increased drag force. This drag force is related to the particles shear stress, which makes the bubble less mobile.

The drag force, buoyancy force and the added mass force are components of the hydrodynamic force on the bubble, which determines the longer oscillations of both bubble velocity and aspect ratio. On the other hand, super-imposed on these longer overall oscillations were small amplitude and high frequency vibrations caused by the capillary force [137]. Both of these oscillations will be analyzed in further detail in the following chapters.

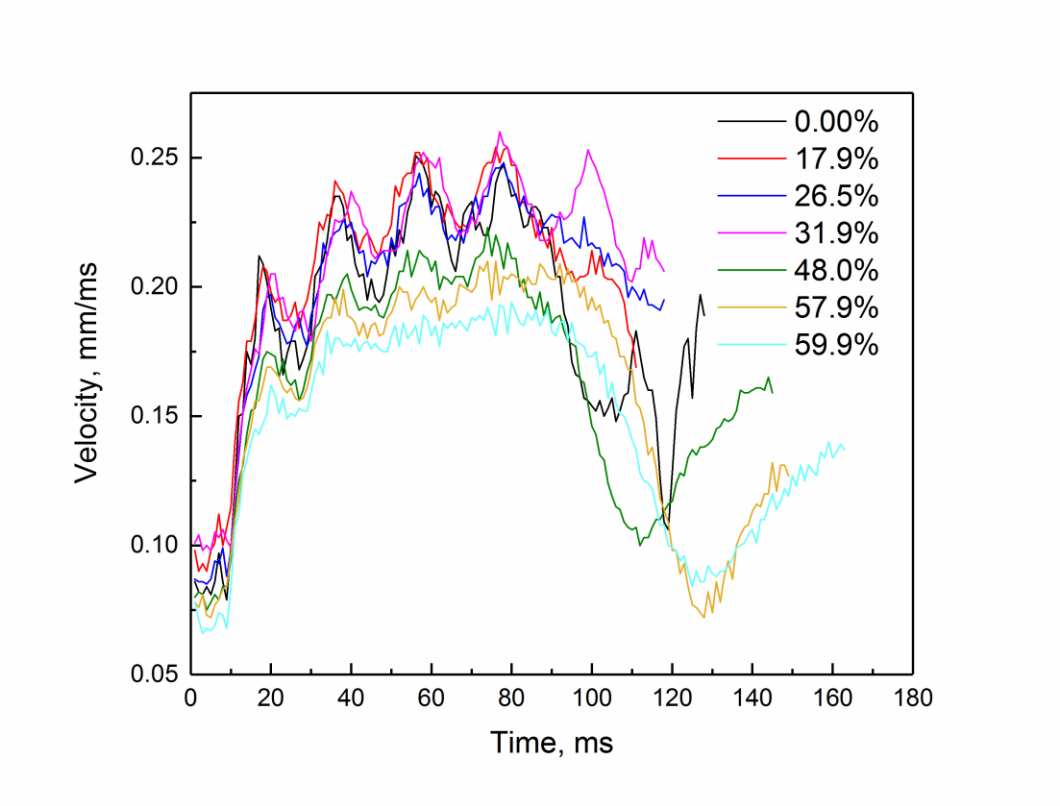

Figure 5.5. Velocity as a function of different fractions of bubbles covered by particles.

5.3 Oscillation period analysis

As described in the previous section, the rise of a bubble is accompanied by a fluctuation of both velocity and aspect ratio. In order to better understand the influence of the particles on the bubble shape change, the capillary oscillation periods, T, were calculated using Equation (5.1) [155–157] and compared with the experimental data.

$$T = 2\pi\sqrt{\frac{\Delta\rho R^3}{6\sigma}}, \tag{5.1}$$

where the bubble radius (R) is 1.45 mm, the density difference ($\Delta\rho$) of gas phase and liquid phase is 1000 kg m^{-3}, and the coefficient of surface tension (σ) is 74 mN/m. Table 5.1 shows the times at which aspect ratio peaks occurred for different levels of particle coverage. Only one bubble is considered for each coverage but five different aspect ratio peaks for the same

bubble can be analyzed, which allows the calculation of confidence intervals for the average oscillation period. It can be concluded that the oscillation periods were within a range of 13-21 ms from Table 5.1, which is in good agreement with the theoretically calculated value of 17 ms from Equation (5.1) [158,159].

Table 5.1. Average oscillation period of bubbles with different levels of particle coverage over the first five oscillations (95% confidence interval included).

Percentage of Coverage	0	17.9%	26.5%	31.9%	48.0%	57.9%	59.9%
Average Period (ms)	18.25 ±1.50	18.50 ±3.32	18.25 ±2.52	18.25 ±1.50	18.00 ±1.24	17.75 ±1.95	16.50 ±3.10

The oscillation of bubble aspect ratio was found to follow a similar pattern under the action of capillary forces; since capillary forces are related to surface tension, it can be concluded that the surface tension does not change significantly when bubbles are covered by particles. Moreover, the mass of particles on the bubble is much lower than the total mass of the bubble (the added mass and the gas mass), and according to Equations (2.4) and (2.5), for the underdamped mechanical vibration, it can be concluded that the presence of particles will not significantly influence the oscillation period of the bubble. Relevant calculations of the mass of particles and the added mass of the bubble will be given in Section 6.5. Note that the added mass of the bubble can be roughly calculated as a half of the buoyancy force on the bubble and the gas mass is negligible. The hydrodynamic forces, include the mass force of the particles as well as the drag force due to the shear stress, play a major role in the phenomena observed and need to be analyzed in further detail.

5.4 Force calculation and analysis

For an ideal bubble, to simplify the calculation, it is assumed that the bubble is rigid and only influenced by the buoyancy and drag forces after it is released from the capillary. The drag force includes both viscous and pressure drag on the body in the direction of the slip velocity [160]. For the bubble-water interface, the drag force can be adapted from Equation (2.7) and written as:

$$F_D = \frac{C_D \rho u^2 A}{2\cos\theta}, \tag{5.2}$$

where θ is the angle between the bubble's minor axis and its vertical moving direction. Since the drag force is the force acting opposite to the relative motion of the bubble moving with respect to a surrounding fluid, the angle is used here to account for the vertical component of the drag force. As mentioned before, we restrict the data analysis to the period when this angle is less than 10°, so the effect is not dramatic but adds accuracy. The widely used Schiller-Naumann drag coefficient from Equation (2.8) is used to calculate the drag force, and the Reynolds number is modified from Equation (2.9) and given as:

$$Re = \frac{\rho d u}{\mu \cos\theta}. \tag{5.3}$$

In a flotation system, Reynolds numbers are high and the flow is considered turbulent. However, the turbulence intensity varies in different parts of the flotation machine. The turbulence intensity is high in the vicinity of the impeller, while in the upper regions of the cell, the turbulence intensity tends to be lower, therefore it is often labelled the quiescent zone, [161].

The added mass force of the bubble can be expressed as:

$$F = m^* \times \frac{du}{dt} = F_B - F_D \ , \tag{5.4}$$

and it characterizes the additional force required to accelerate a bubble when immersed in the water. Here m^* is the added mass [162,163], and the buoyancy force F_B, similar to Equation (2.6), is defined as:

$$F_B = \frac{1}{6}\pi d^3 \Delta\rho g \ . \tag{5.5}$$

It should be noted that the aspect ratio of the bubble is closest to 1 immediately after the bubble is released (in the first 5ms). The corresponding diameter of the bubble at this point is the only one used for the calculation of Equation (5.5). This is due to the fact that the effect of bubble rotation is minimum at the beginning of the rising process. The images used for volume determination are therefore of bubbles with little deformation and so the assumption of an oblate spheroidal shape is appropriate. During the experiment, the residence time is not sufficient for any significant diffusion of the bubble (this sort of effect would be significant with micron scale bubbles, but these are of the millimeter scale). It would not be appropriate for volume determination later in the bubble's life, but the bubble's volume is assumed to remain constant (this is an appropriate assumption given the small rise distance considered). The added mass is:

$$m^* = C_m \times \frac{1}{6}\pi d^3 \rho \ . \tag{5.6}$$

The added mass coefficient (C_m) is a function of the bubble-deformation ratio, i.e., the aspect ratio (AR):

$$C_m = 0.62 \times AR - 0.12 \ . \tag{5.7}$$

Using Equation (4.8) and Equation (4.9), we can express a and b in terms of d and AR as follows:

$$a = d \times AR^{-\frac{2}{3}}, \tag{5.8}$$

$$b = d \times AR^{\frac{1}{3}}. \tag{5.9}$$

Therefore the cross section area can be defined as:

$$A = \pi\left(\frac{b}{2}\right)^2 = \frac{\pi d^2}{4} AR^{\frac{2}{3}}, \tag{5.10}$$

and the acceleration of the bubble can be expressed as:

$$\frac{du}{dt} = \frac{1}{m^*}(F_B - F_D) = \frac{1}{C_m}\left(g - \frac{3C_D u^2}{4dcos\theta} AR^{\frac{2}{3}}\right). \tag{5.11}$$

In this calculation, the gravity acting on the gas was regarded as negligible. The Schiller–Naumann drag coefficient was developed for rigid solid spherical particles and also it was extended to various shapes of particles, drops and bubbles [138,148,163,164]. Since the bubble shape oscillates during the rising period, the drag coefficient of a real bubble is lower than the one of a spherical bubble [104,137,165]. In order to fit the calculated velocity to the experimental one, the value of C_D has to be adjusted.

A drag modification parameter, $\eta_{B,}$ is added to adjust the drag coefficient for the uncoated bubble, so Equation (5.11) can be changed to

$$\frac{du}{dt} = \frac{1}{m^*}(F_B - F_D) = \frac{1}{C_m}\left(g - \frac{3C_D' u^2}{4dcos\theta} AR^{\frac{2}{3}}\right), \tag{5.12}$$

where C_D' is the modified drag coefficient of the uncoated bubble according to the experimental results:

$$C_D' = \eta_B C_D \ . \tag{5.13}$$

The calculated velocity on the left side of Equation (5.12) was fitted to the experimental velocity data of the uncoated bubble, using least squares regression analysis, and thus the value of η_B can be determined. The existence of adsorbed reagents on the bubble surface can exert a significant influence on the surface forces and the drag coefficient, which finally affect the bubble velocity [164].

For the calculation of the coated bubble, the overall force that the particles exert on the bubble, F_i, must be taken into account. Since particles move together with the bubble, and to simplify the process, the drag force F_{Dp} from the particles can be regarded as a force that makes the bubble less mobile, which can be expressed as:

$$F_{Dp} = \eta_p F_D \ , \tag{5.14}$$

$$m_p \frac{du}{dt} = F_i + F_{Bp} - m_p g - F_{Dp} \ , \tag{5.15}$$

where F_{Bp} denotes the buoyancy force on the particles, m_p is the mass of the particles (calculated from the particle coverage and with particles being regarded as a monolayer evenly distributed onto the bubble surface without any aggregation). η_p is a drag modification factor corresponding to different levels of particle surface coverage, and Equation (5.4) can therefore be changed to

$$\frac{du}{dt} = \frac{1}{m^*} \left(F_B - F_D - F_i\right) . \tag{5.16}$$

Substituting F_i from Equation (5.15) leads to

$$\frac{du}{dt} = \frac{1}{m_p + m^*}\left(F_B + F_{Bp} - F_D - F_{Dp} - m_p g\right). \tag{5.17}$$

Substituting F_D and F_{Dp} from Equations (5.12) and (5.14) into Equation (5.17) gives:

$$\frac{du}{dt} = \frac{1}{m_p + m^*}\left(F_B + F_{Bp} - m_p g - \frac{C_D \rho u^2 \eta_B \pi d^2 A R^{\frac{2}{3}}}{8\cos\theta}(1 + \eta_p)\right), \tag{5.18}$$

$$C_{D-Bp=} C_D'\left(1 + \eta_p\right), \tag{5.19}$$

where C_{D-Bp} represents the modified drag coefficient of the particle-laden bubbles. The calculated velocity on the left side of Equation (5.18) was fitted to the experimental velocity data of the coated bubble, using least squares regression analysis, and thus the value of η_p can be determined. As the bubble detaches from the capillary, its velocity fluctuates for the first 10 ms, after which the velocity increases before further fluctuation. For the purposes of these calculations, the first 10 ms were not taken into account. Similarly to the previous section, data is only considered for the initial period during which the angles between the bubble's minor axis and its vertical moving direction do not exceed 10°.

5.5 The drag modification factor and modified drag coefficient

From the data in Figure 5.1(b) and Figure 5.5, η_B can be calculated using the velocity of the uncoated bubble, which results in a value of 0.81 ± 0.04 (with 95% confidence interval). From the data in Figure 5.2 (b) and Figure 5.5, η_p can be calculated using the velocity of the initially fully coated bubbles, and the result is 1.05 ± 0.05 (with 95% confidence interval).

For bubbles coated at different particle coverages, given η_B of 0.81, the corresponding values of η_p can be calculated from Equations (5.18) and (5.19). These are shown in Figure 5.6, from which it can be observed that the drag modification factor η_p increases from 0.13 to 1.05 as the

surface coverage of particles increases from 0.0% to 59.9%. There are two reasons for this increase, one is the drag due to roughness, since the surface of the particle-bubble aggregate is less smooth than that of the uncoated bubble; the other is the drag due to reduced mobility of the bubble interface, as particles move around the bubble surface will add shear force to the bubble and dampen its aspect ratio oscillation.

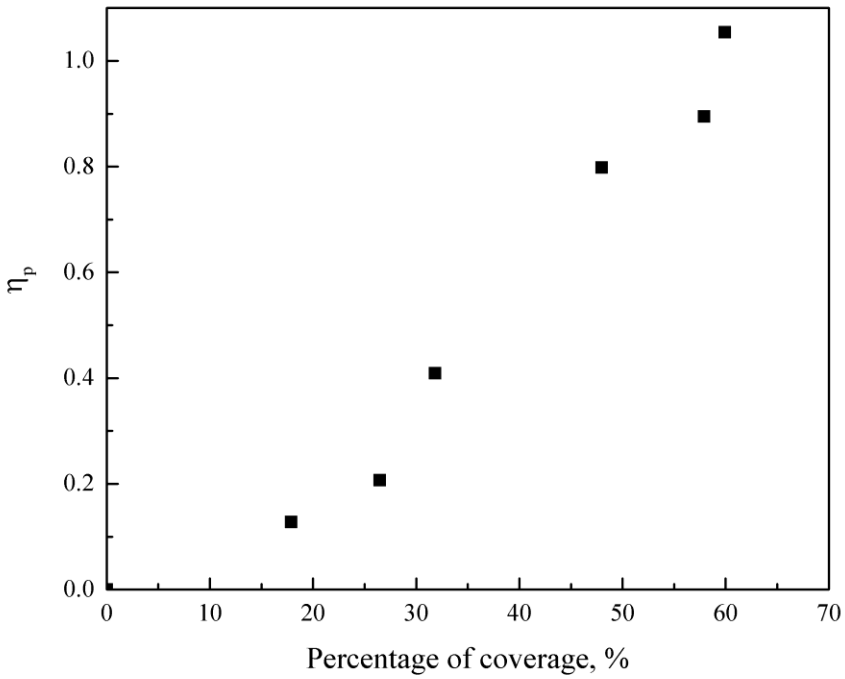

Figure 5.6. Particle influence on the drag coefficient according to different fractions of bubbles covered by particles.

The drag coefficient is a function of Reynolds number, and this Reynolds number is influenced by the bubble velocity. As bubble velocity changes during the rising period, therefore the relevant drag coefficient also changes correspondingly. In Figure 5.7, the experimental data (C'_{Dr}) as well as the modified drag coefficient (C'_D) from the least-squares fit to the experimental data are compared and illustrated. Here we should note that both C'_D and C'_{Dr} are calculated from Equations (2.8), (5.3) and (5.13), the only difference is the former is

calculated using the velocity from the experimental data, while C_D' is calculated using the fitting velocity from the left side of Equation (5.12). As can be seen, the modified drag coefficient fits well with the experimental one. The bubble rising velocity varies with time, and its drag coefficient also changes correspondingly.

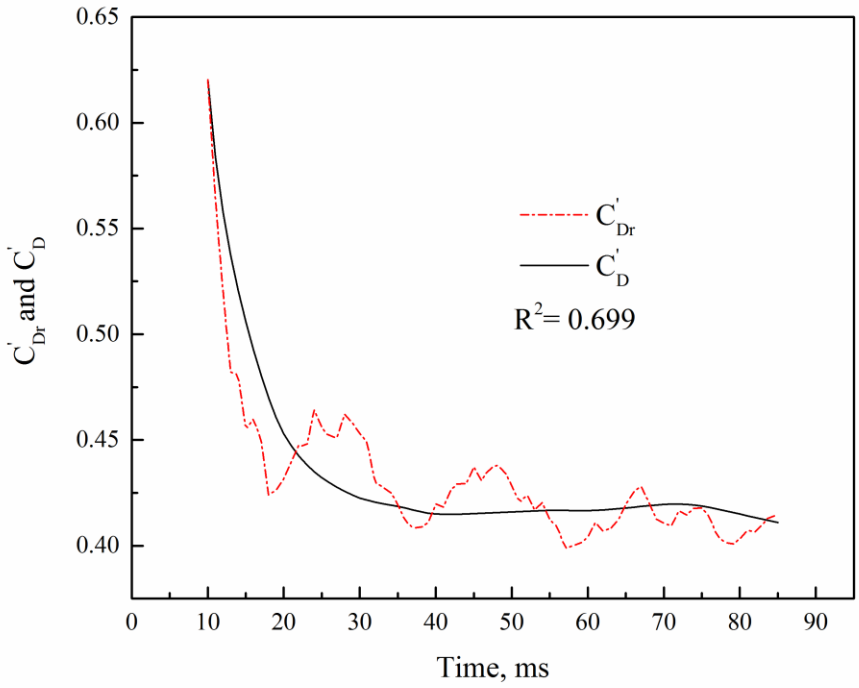

Figure 5.7. Modified drag coefficient compared with the drag coefficient calculated from the experimental data for an uncoated bubble as a function of the time.

For the uncoated bubble, the ideal drag coefficient from the Schiller-Naumann model as well as the modified drag coefficient from the least-squares fit to the experimental data as a function of Reynolds number are displayed in Figure 5.8 (a). It was found that both the drag coefficient predicted by the Schiller-Naumann model and that from the fitting to the data decrease with Reynolds number. It is because Reynolds number is the ratio of inertial forces to viscous forces within a fluid, when the Reynolds number is lower, the viscous force is higher, and therefore the drag coefficient is higher. It can also be observed that the Schiller-Naumann model over-predicts the real drag coefficients for the rising uncoated bubble. The modified drag coefficient

of bubbles covered with different levels of particles as a function of Re are summarized in Figure 5.8 (b). It is clear that with the increase of particle surface coverage, the modified drag coefficient of particle-laden bubbles increases.

5.6 Summary

The behavior of bubbles after being released from a capillary tip was investigated as a function of seven different particle surface coverages, i.e., from initially bare bubble to the capillary pinned bubble which is fully coated.

The oscillation of bubbles coated with different levels of particles followed a similar pattern, indicating the surface tension was not significantly affected by a bubble being coated or not. A drag modification factor η_p, which quantifies the drag influence of particles on the bubble velocity, was identified from force analysis.

It has been shown that the drag modification factor follows an increasing trend rising from 0.13 to 1.05 as the surface coverage of particles increases from 0.0% to 59.9%. This drag modification has allowed a modified drag coefficient to be attained for particle-laden bubbles for the first time. It is shown that the modified drag coefficient of particle-laden bubbles increases with the increase of particle surface coverage and decreases with the increase in the Reynolds number.

Coarse and fine particles are often not recovered during the flotation process, or are recovered poorly. The change of particle size wil also change the behavior of bubble-particle aggregates when they are released and rise in the liquid. For the following chapter, the influence of particle size will be investigated and analyzed.

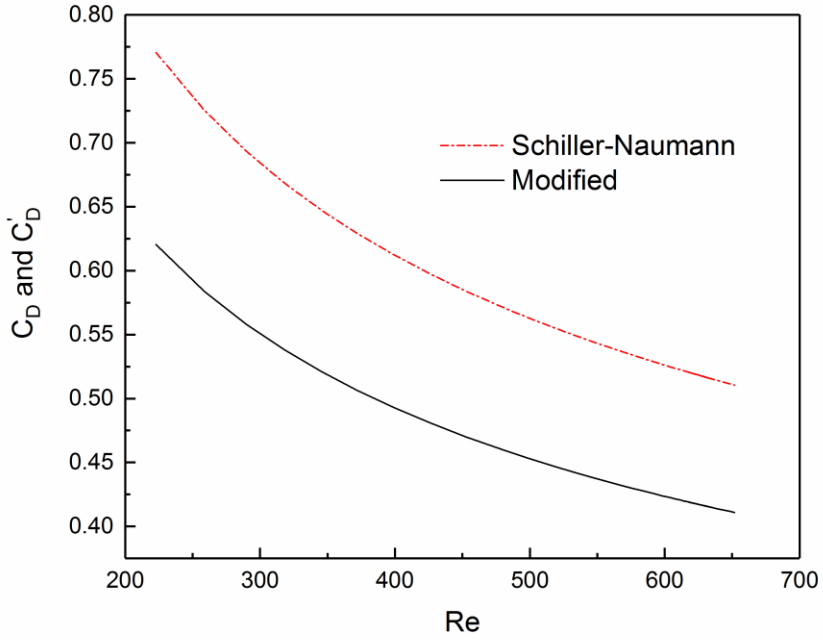

(a)

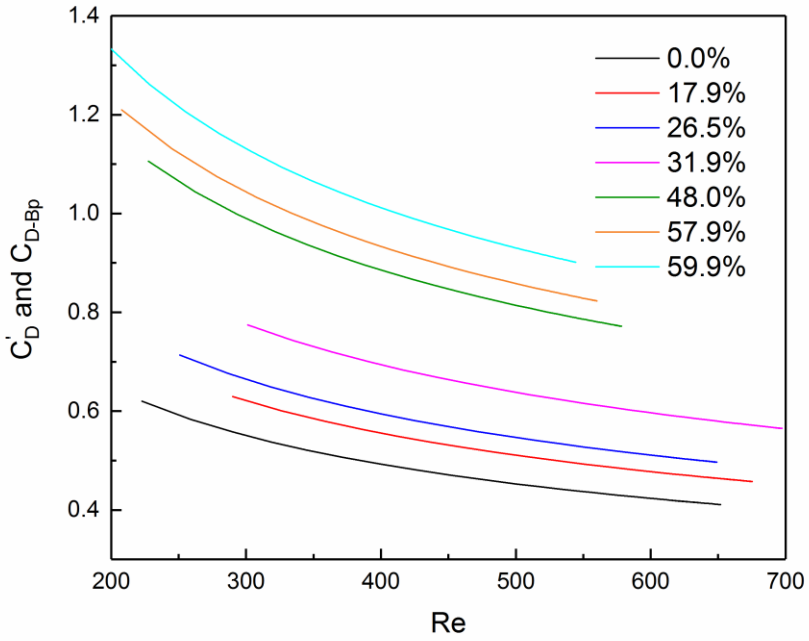

(b)

Figure 5.8. (a) Modified drag coefficient compared with the drag coefficient predicted from Schiller-Naumann for an uncoated bubble as a function of the Reynolds number. (b) Modified drag coefficients of the uncoated bubble and bubbles loaded at different levels of particle coverage as a function of the Reynolds number.

Chapter 6 Influence of particle size on rising particle-laden bubbles

6.1 Particle coverage as a function of time in the attachment experiments

The flotation rate of hydrophobic particles is determined by the interactions between particles and bubbles, i.e., the collision-attachment efficiency, which is highly dependent on particle size. The experimental setup in this work allowed us to study the influence of particle size on the speed at which particles attached to capillary pinned bubbles. An example of the change in particle coverage on bubbles at different times, for the sample of size d_{90}=156 μm, is shown in Figure 6.1. As can be seen, the coverage increased from 9.0 mm^2 after 10 s to 23 mm^2 (fully coated) at 97 s.

Table 6.1 presents the average time that was required to achieve a fully coated bubble for each of the particle size classes investigated. In general, a decrease in attachment speed with particle size is observed, with the coarsest particle class requiring substantially more times for full surface coverage.

6.2 The influence of particle size on the velocity and aspect ratio change of rising particle-laden bubbles

Particle size is one of the most significant components governing the overall performance of industrial processes, such as froth flotation kinetics, therefore the influence of particle size on the velocity and aspect ratio of particle-laden bubbles is worthy of being investigated. As can be observed from Figure 6.2, the aspect ratio

oscillations of rising bubbles, initially half coated with particles of different sizes, followed a similar pattern, with both a lag observed in the time at which the periodic peaks occur and aspect ratio values decreasing with increasing size of the particles covering the bubbles. The temporal evolution of the velocity of the rising particle-laden bubbles (initially half coated) is shown in Figure 6.3. Similar to what it is observed for aspect ratio, velocities oscillated and exhibited a lag in local maxima with increasing particle size, which is particularly clear at earlier times. In general, velocity magnitudes also decreased with increased particulate size. Interestingly, from Figure 6.2 and Figure 6.3, it can be seen that the periodic peaks in velocity coincided with local minima in aspect ratio.

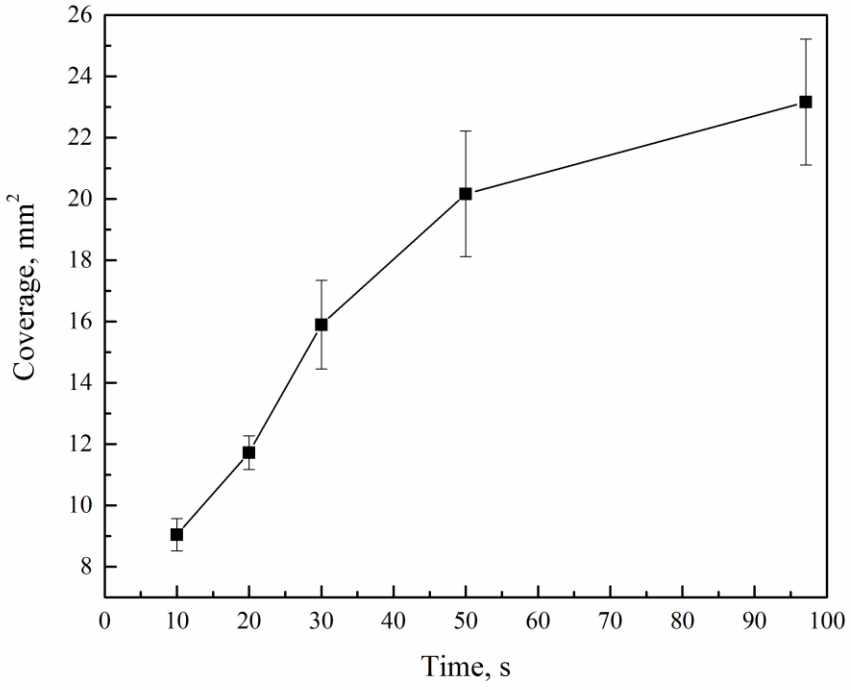

Figure 6.1. Particle coverage on capillary pinned bubbles as a function of time for particles of size d_{90}=156 μm. The data are shown with 95% confidence intervals.

Table 6.1. Average time needed for the bubbles to be fully coated with particles (95% confidence interval included).

Particle	Average time/s	Bubbles
Size 1	29.9±4.3	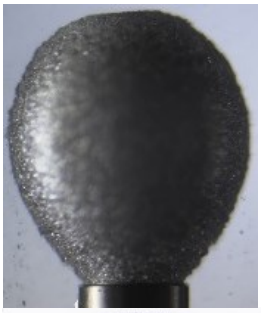
Size 2	59.8±4.1	
Size 3	93.3±8.7	
Size 4	97.1±8.6	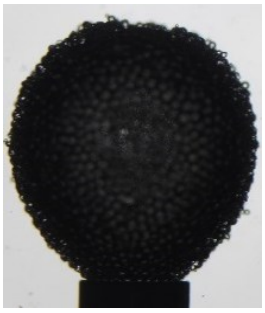
Size 5	>600	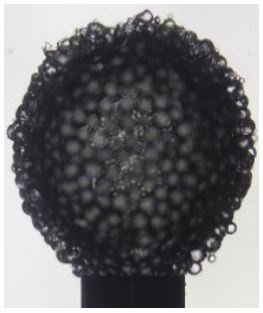

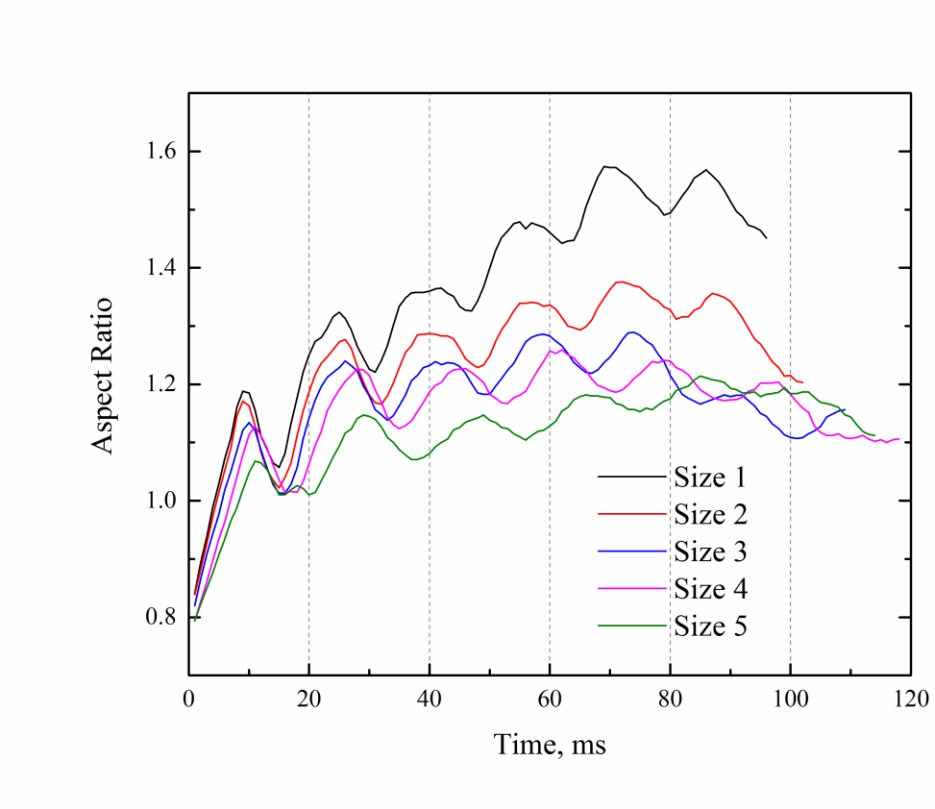

Figure 6.2. Aspect ratio of rising bubbles (initially half coated) as a function of particle size.

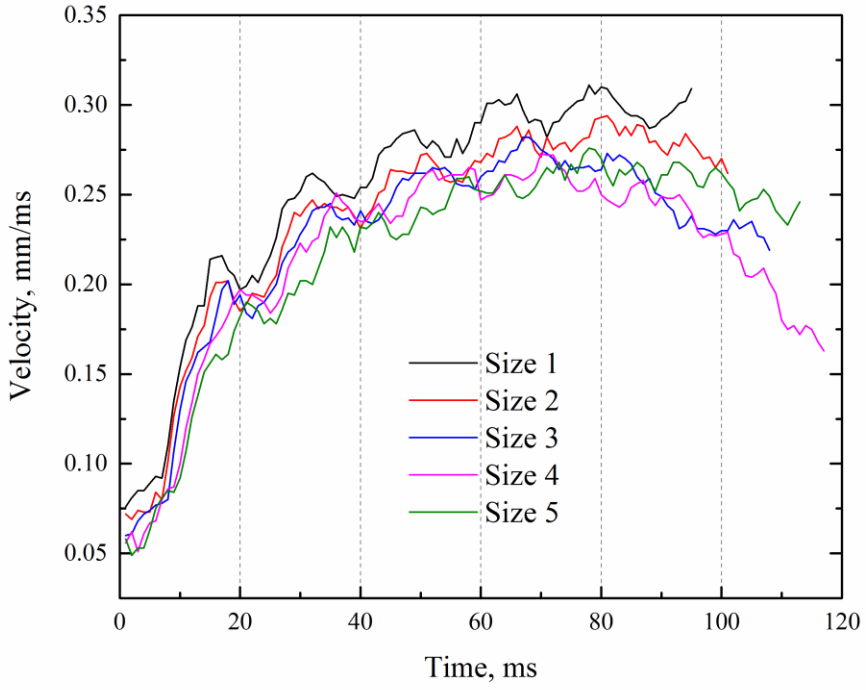

Figure 6.3. Velocity of rising bubbles (initially half coated) as a function of particle size.

The aspect ratio and velocity data from experiments in which the bubbles were initially fully coated can be seen in Figure 6.4 and Figure 6.5, respectively. Similar to what was observed for initially half coated bubbles, there is a lag in the oscillations and a reduction in both aspect ratios and velocity values with increasing particle size. It is noticed, however, that the oscillation of aspect ratio for initially fully coated bubbles were no longer measureable after 50 ms, with only relatively small changes after that point. The higher level of particle coverage also resulted in a reduction in the maximum values researched for both aspect ratio and velocity. From Figure 6.4 and Figure 6.5, we can deduce that bubble velocity is constant when the aspect ratio is constant, irrespective of the attached particle size.

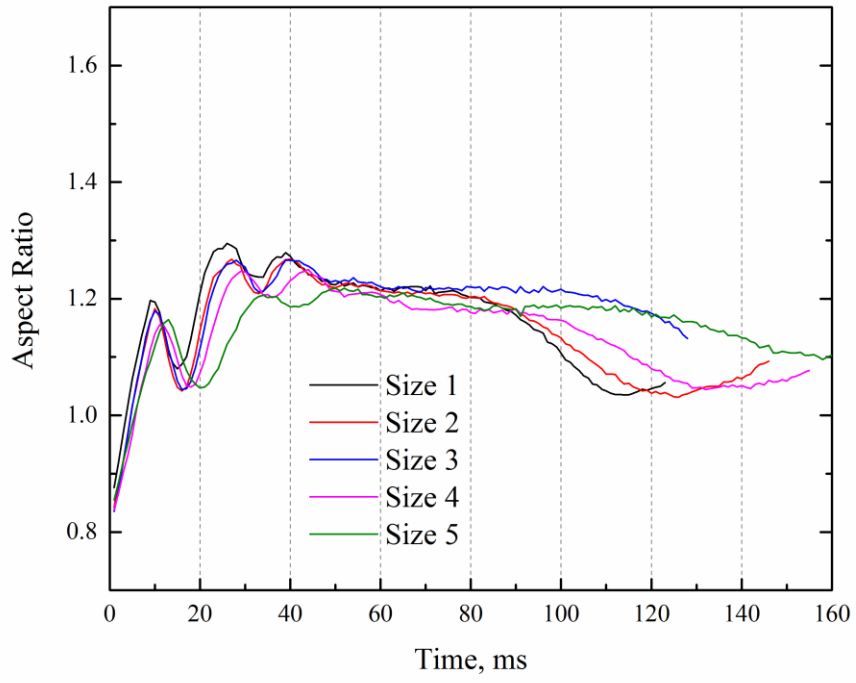

Figure 6.4. Aspect ratio of rising bubbles (initially fully coated) as a function of particle size.

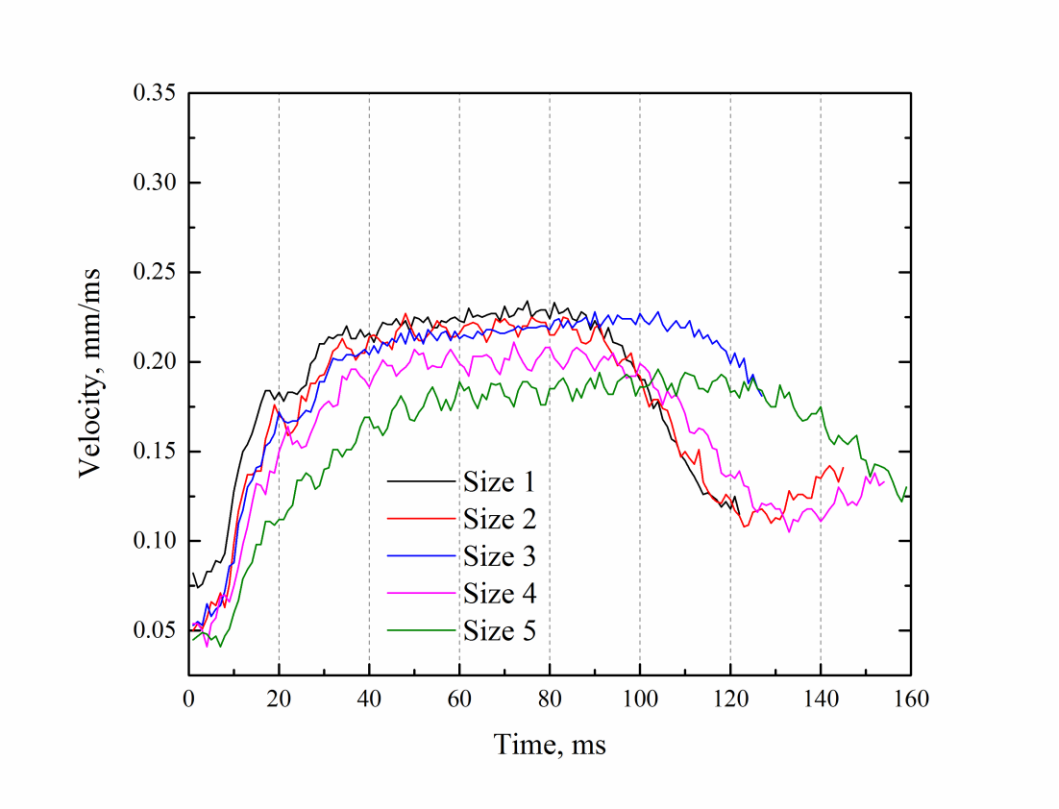

Figure 6.5. Velocity of rising bubbles (initially fully coated) as a function of particle size.

6.3 Oscillation period analysis

To analyze the effect of particles on the aspect ratio change, the theoretically derived oscillation period (T) of a rising uncoated bubble of radius 1.60 mm (R) was calculated using Equation (5.1) and the calculation results were compared to the experimental data of particle-laden bubbles.

The measured oscillation periods of the aspect ratio of particle-laden bubbles are about 0.020 s, which are in good agreement with the calculated value of 0.019 s. The capillary force causes the shorter period oscillation in aspect ratio while the overall longer period oscillation in aspect ratio is determined by hydrodynamic forces. This implies that the high frequency oscillations observed in Figure 6.2 and Figure 6.4 are therefore capillary oscillations rather than hydrodynamic oscillations. Moreover, since

capillary forces are related to surface tension, and bubbles coated with different size of particles follow a similar pattern according to the experiment results, it can be concluded that the surface tension of the bubbles is not significantly influenced by the particles attached to their surfaces. The hydrodynamic forces thus play a major role in the phenomena observed and need to be analyzed in detail.

The times when periodic aspect ratio peaks occur for rising particle-laden bubbles, both initially half and fully coated, are shown in Figure 6.6 and Figure 6.7, respectively. The bubble aspect ratio peaks were minor delayed when the bubble was coated with coarser particles. The number of aspect ratio peaks decreased with higher particle coverage, indicating a more strongly damped bubble oscillation.

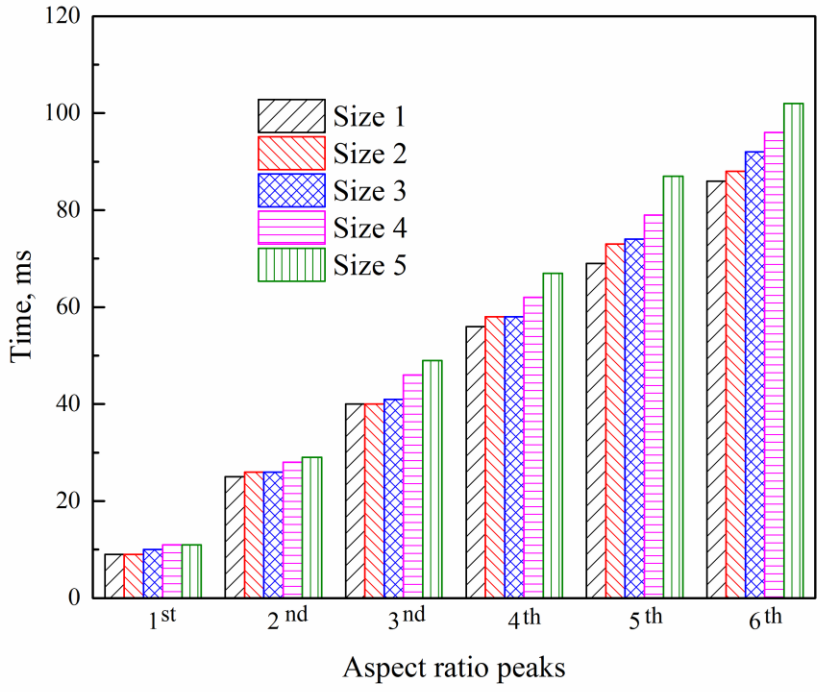

Figure 6.6. Times when aspect ratio peaks occur for rising bubbles (initially half coated).

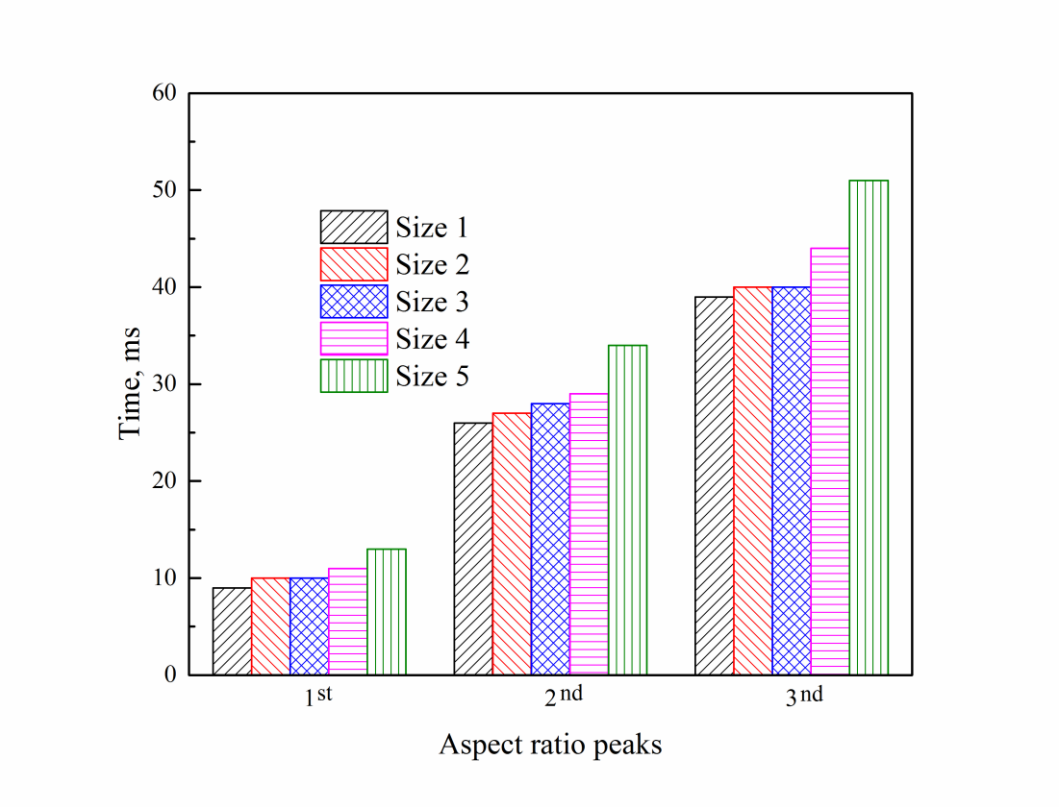

Figure 6.7. Times when aspect ratio peaks occur for rising bubbles (initially fully coated).

6.4 The drag modification factor analysis

In this study, the surface tension of the liquid is nearly equal to that of pure water, due to the low concentration of TTAB used. The diameter of the bubbles, produced from the same capillary, can be roughly predicted using equation [152,166] (6.1):

$$d = \sqrt[3]{\frac{6D\sigma}{g\Delta\rho}}, \tag{6.1}$$

where d is the bubble equivalent diameter, D is the capillary inner diameter and g is the gravitational acceleration (9.8 m/s^2). The calculated bubble diameter is 3.36 mm, which is in good agreement with the experimental results shown in Table 6.2 and Table 6.3. It should be noted that the diameter is calculated from the bubble-particle

aggregate, which is slightly larger if coarser particles (or more particles) were attached to the bubble surface.

Unlike a rigid particle, the shape of a rising bubble deforms from spherical to ellipsoidal. Moreover, their shape can be subject to dynamical changes such as periodic oscillations [104]. On the basis of our previous calculation model, the rise velocity of particle-laden bubbles is mainly influenced by the hydrodynamic forces. For initially half coated bubbles, the bubble drag modification factor was 0.63, calculated from a released uncoated bubble with a diameter of 3.11 mm. For initially fully coated bubbles, the bubble drag modification factor was 0.65, which was calculated from a released bubble with a diameter of 3.31 mm. The covered area, bubble-particle aggregates diameter, percentage of particle coverage and average particle drag modification factor (η_p) for rising bubbles which were initially half and fully coated are shown in Table 6.2 and Table 6.3, respectively. The particle drag modification factors are the average values from the experiments, with 95% confidence intervals, which are also shown in Figure 6.8.

As can be seen from Figure 6.8, for initially half coated bubbles, the particle drag modification factors increased with an increase in particle size, rising from 0.53 to 1.45. For initially fully coated bubbles, the particle drag modification factors followed a similar pattern, rising steadily from 1.31 to 1.98 as the particle size increased. Overall, a higher fraction of particle coverage induced a higher particle drag modification factor on rising particle-laden bubbles. This is in line with what is observed from Figure 6.3 and Figure 6.5 that the rising bubble velocity decreased when more particles were attached to the bubbles.

Table 6.2. Particles drag modification factors for initially half coated bubbles (95% confidence interval included).

Particle size	Covered area/ mm^2	Diameter/ mm	Coverage percentage/%	Drag modification factor (average)
Size 1	10.66	3.22	32.8	0.53±0.02
Size 2	11.31	3.21	34.9	0.61±0.05
Size 3	12.36	3.26	37.2	0.71±0.14
Size 4	10.68	3.34	30.5	0.78±0.05
Size 5	10.13	3.48	26.6	1.45±0.14

Table 6.3. Particle drag modification factors for initially fully coated bubbles (95% confidence interval included).

Particle size	Covered area/ mm^2	Diameter/ mm	Coverage percentage/%	Drag modification factor (average)
Size 1	26.31	3.37	73.7	1.31±0.04
Size 2	24.59	3.41	67.4	1.38±0.05
Size 3	25.30	3.45	67.8	1.43±0.06
Size 4	25.11	3.47	66.5	1.66±0.02
Size 5	23.99	3.56	60.3	1.98±0.09

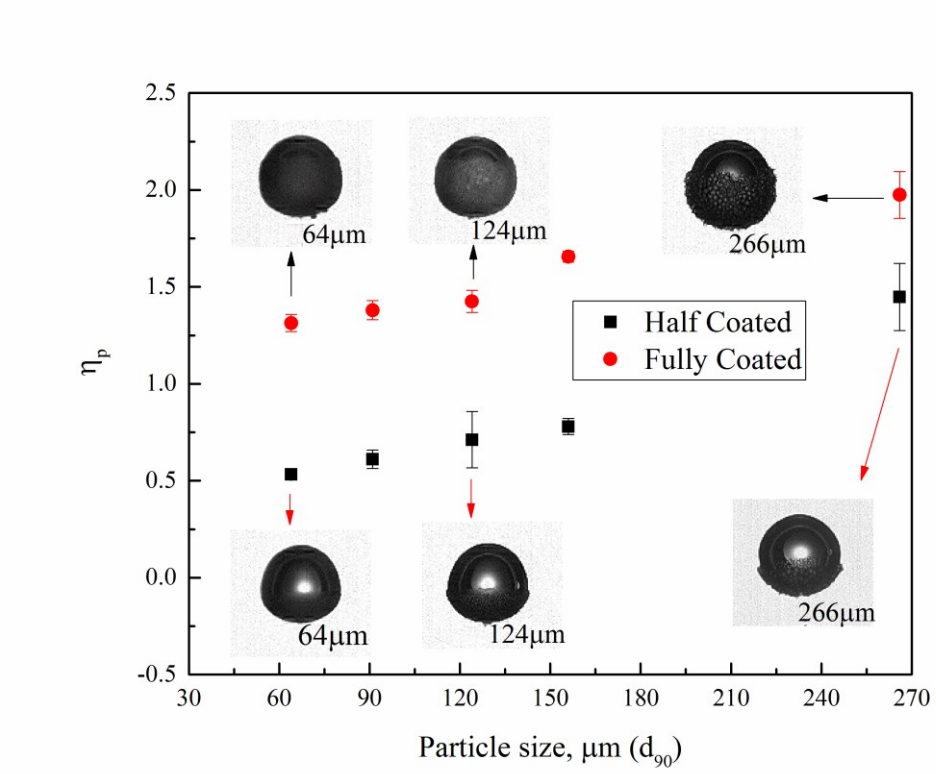

Figure 6.8. The particle drag modification factors for rising particle-laden bubbles as a function of particle size. For initially half and fully coated bubbles, 95% confidence intervals are shown.

6.5 The modified drag coefficient and forces analysis of particle-laden bubbles

The modified drag coefficient of particle-laden bubbles as a function of the Reynolds number is summarized in Figure 6.9, and these bubbles were initially fully coated with different sizes of particles. The modified drag coefficient of particle-laden bubbles decreased with the increase in the Reynolds number, independently of particle size. When the particle size (d_{90}) was increased from 64 μm to 124 μm, the modified drag coefficient showed only a minor increase. However when particle size (d_{90}) was increased further to 156 μm and subsequently to 266 μm, the modified drag coefficient increased sharply. The likely reason is that when the attached particles are small, the mass force and drag force on particles are small, and these forces are mostly balanced

by the reduced drag force on the bubble part. The reduced drag force on the bubble is caused by the decreased bubble frontal area (due to the bubble being more spherical). However, as the particle size increases, the mass force and drag force on particles are comparatively large, and they begin to play a more dominant role in dampening the shape oscillations and decreasing the velocity of particle-laden bubbles. This modified drag coefficient is useful for predicting the behavior of rising bubble-particle aggregates in three-phase systems.

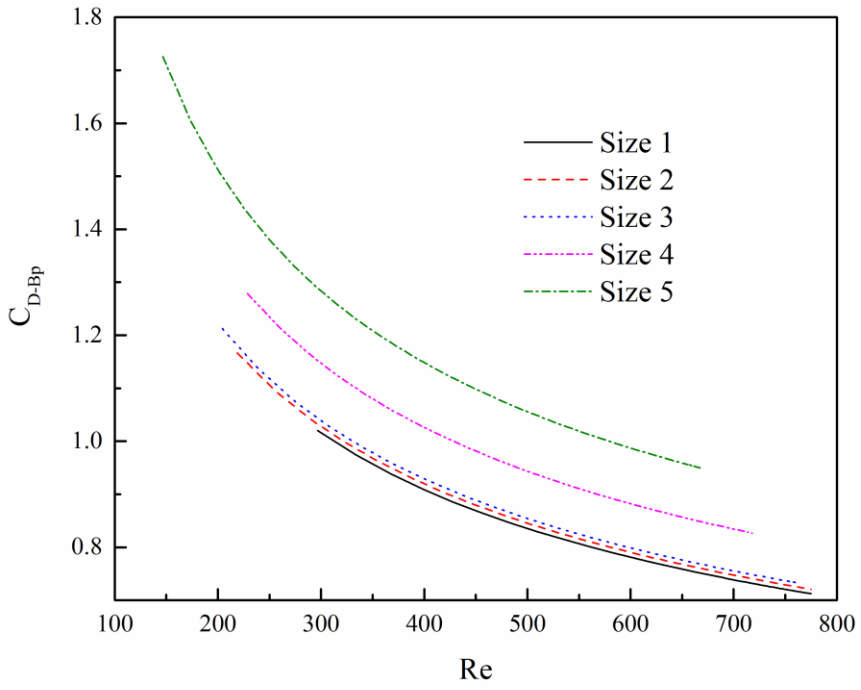

Figure 6.9. The modified drag coefficient of particle-laden bubbles with different sizes of particles as a function of the Reynolds number (initially fully coated).

To further explore the influence of particle size on the motion of particle-laden bubbles, the forces exerted on the bubbles and particles were calculated and compared for the case of initially fully coated bubbles. These include the bubble drag force, the particle drag force, the bubble buoyancy force, and the difference between the particle buoyancy and gravity forces.

The forces on the rising bubbles coated with finer particles (size 1) and coarser particles (size 5) from Table 6.3 are shown in Figure 6.10 (a) and Figure 6.10 (b), respectively. As can be observed, the buoyancy force of the bubble was significantly larger than the other forces. Both the drag forces from the particles and the bubbles increased initially and remained constant thereafter. In response to the oscillation period analysis in Section 5.3, the relevant forces on the bubble with fine particles were calculated. The buoyancy force of the bubble is about 196.8 μN, and therefore the added mass force of the bubble is about 98.4 μN when the bubble is spherical, which is way higher than the mass force of attached particles (16.0 μN). This can help to explain why the presence of particles has minor influence on the bubble capillary oscillation period.

For the bubble coated with finer particles, the difference between the particle buoyancy and gravity forces was relatively small, and the particle drag force was only slightly higher than that of the bubble. For the bubble coated with coarser particles, the particle buoyancy and gravity force difference was larger than for finer particles.

The drag force on the bubble was smaller when coated with coarser particles, mainly due to a more spherical bubble formed with coarser particles attached. The drag force from coarser particles was twice that exerted on the bubble, and also higher than that from finer particles.

It can be concluded that particles decrease the bubble motion, not only due to the added mass force but more so due to the added drag force. When bubbles are coated with coarser particles, the particle drag force plays a more significant role in reducing the rising velocity of particle-laden bubbles.

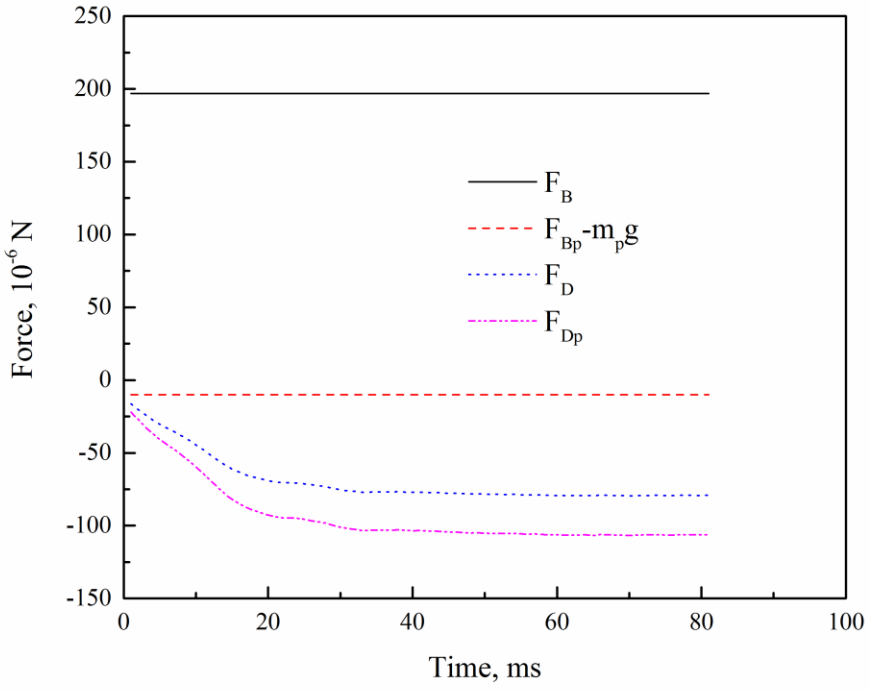

(a)

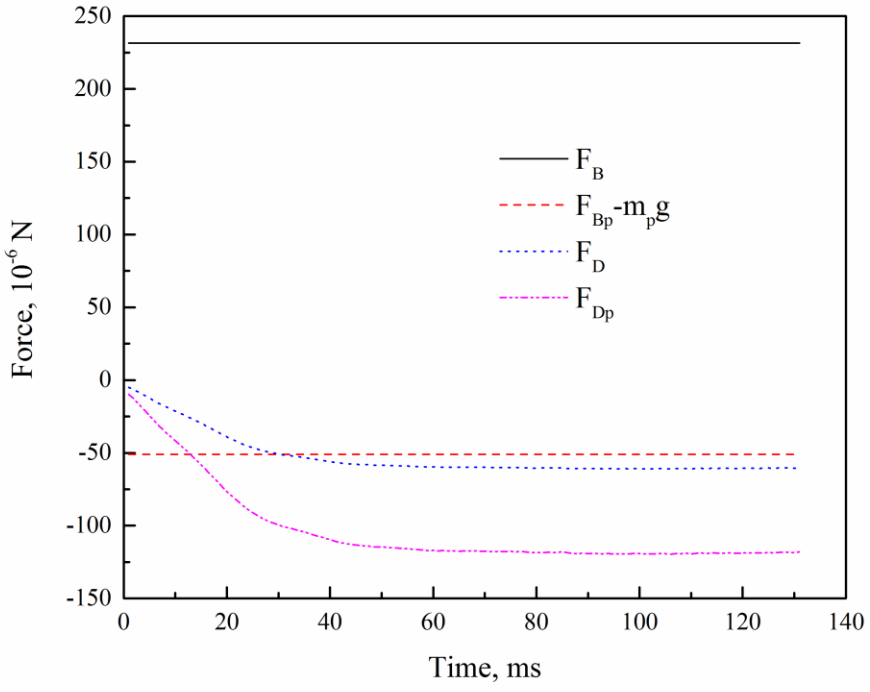

(b)

Figure 6.10. Forces acting on rising particle-laden bubbles which are initially fully coated (a) Particle size d_{90}=64μm. (b) Particle size d_{90}=266μm.

6.6 Summary

The behavior of rising particle-laden bubbles was investigated as a function of particle size. A series of experiments combined with theoretical analyses of forces acting on the bubbles were used to propose a drag modification factor. This drag modification factor allows for the quantification of the effect which particles of different sizes exert on the rising bubbles.

It is shown that more time is needed for a capillary pinned bubble to be fully coated with coarser particles. After the bubbles are released and as they rise, their aspect ratio oscillations follow a similar pattern regardless of the size of the attached particles. An increase in the particle size, however, results in both a delay in the periodic peaks in the aspect ratio and lower aspect ratio oscillation amplitudes. The increase in the particle size also lowered the velocity of the rising bubbles. It is noted that all peak velocities correspond to valleys of aspect ratio, independent of the particle size. Another interesting finding is that for initially fully coated bubbles, their shape oscillation is more strongly dampened and presents fewer aspect ratio peaks than those initially half coated bubbles.

A force analysis showed that the particle drag modification factor increases as either particle size or particle coverage increases. The modified drag coefficient, calculated from the particle drag modification factor, increases with the particle size, although it decreases with Reynolds number independent of the particle size. This analysis also shows that as the particle size increases, the particle drag force plays a more dominant role in decreasing the velocity of particle-laden bubbles, rather than the bubble aspect ratio.

Chapter 7 Conclusions and recommendations for future research

7.1 Conclusions

This thesis presents the influence of particles on the rising behavior of particle-laden bubbles. The conclusions are summarized as below:

(1) An increase in the particle coverage or particle size dampens the aspect ratio oscillation amplitudes and lowers the velocity of the rising particle-laden bubbles. The peak velocities correspond to valleys of aspect ratio, independent of the particle size or coverage. A higher level of particle coverage induces a lower bubble acceleration and this acceleration is inversely correlated to the aspect ratio and its change.

(2) Aspect ratio follows a similar oscillation pattern regardless of particle coverage or size, although a delay in the periodic peaks in the aspect ratio was observed for coarse particles, and fewer aspect ratio peaks of shape oscillation were presented for initially fully coated bubbles than those initially half coated ones. This indicates that the surface tension is not significantly affected, and it is mainly the hydrodynamic forces that cause the difference of the bubble behavior.

(3) From force analysis, a drag modification factor, which quantifies the drag influence of particles on the bubble velocity, was identified; a modified drag coefficient for particle-laden bubbles was also obtained for the first time. Both of the above parameters increases as either particle size or coverage increases, whereas the modified drag coefficient decreases with increased Reynolds number. As the particle

size increases, the particle drag force plays a more dominant role in decreasing the velocity of particle-laden bubbles, rather than the bubble aspect ratio.

This work contributes to a comprehensive understanding of the behavior of particle-laden bubbles, in particular, with regards to the increase in the modified drag coefficient experienced by the bubble-particle aggregate with an increase in particle coverage and particle size. Particles attached to the surface of bubbles not only induce an additional drag force, but also dampen the bubble shape dynamics, both of which influence the bubble velocity.

Understanding and being able to predict the bubble hydrodynamics in these complex three-phase systems is essential to improve the performance of industrial processes, such as mineral froth flotation, that rely on particle-laden bubbles.

7.2 Recommendations for future research

Based on the main findings of this research, further studies could advance the understanding of rising particle-laden bubbles as well as other relevant processes. Several topics worth investigation are identified in the following categories.

(1) Laboratory investigations initially make use of glass bead particles with different sizes, while other mineral particles with different densities can be considered. It is worth comparing the behavior of bubbles coated with particles of same size but different densities. The drag coefficient change with different particle densities can be explored.

(2) The current experimental system uses bubbles of similar size which is close to 3mm in diameter. However, in real flotation, bubble size is influenced by different mechanical and chemical conditions of the operational environment. Therefore, the influence of bubble sizes on the behavior of particle-laden bubbles is another aspect

that needs to be investigated. The drag coefficient change with different bubble sizes can also be explored.

(3) The experimental findings and correlations developed in this work for rising particle-laden bubbles can be implemented to develop an analytical equation to formulate drag coefficient as a function of particle size and surface coverage of particles, it can also be implemented to into Computational Fluid Dynamics models, relating the bubble velocity to influential factors including the attached particle size and particle coverage.

(4) The current study is conducted with air bubbles, it is suggested that this investigation can be expanded to study bubbles with different gases such as CO_2 bubble in mass transfer and chemical reaction. Moreover, it can be adapted to study drop motion in soft dispersed systems, as well as oil droplets with applications in oil extraction.

References

[1] H. Li, Z. Liu, J. Chen, B. Sun, Y. Guo, H. He, Correlation of aspect ratio and drag coefficient for hydrate-film-covered methane bubbles in water, Exp. Therm. Fluid Sci. 88 (2017) 554–565.

[2] C. Boyer, A.M. Duquenne, G. Wild, Measuring techniques in gas-liquid and gas-liquid-solid reactors, Chem. Eng. Sci. 57 (2002) 3185–3215.

[3] J. Huang, T. Saito, Influence of Bubble-Surface Contamination on Instantaneous Mass Transfer, Chem. Eng. Technol. 38 (2015) 1947–1954.

[4] Y. Zhao, Y. Li, J. Huang, J. Liu, W. Wang, Rebound and attachment involving single bubble and particle in the separation of plastics by froth flotation, Sep. Purif. Technol. 144 (2015) 123–132.

[5] Z. Huang, C. Cheng, Z. Liu, W. Luo, H. Zhong, G. He, C. Liang, L. Li, L. Deng, W. Fu, Gemini surfactant: A novel flotation collector for harvesting of microalgae by froth flotation, Bioresour. Technol. 275 (2019) 421–424.

[6] A. Eskanlou, M.R. Khalesi, M. Mirmogaddam, M. Hemmati Chegeni, B. Vaziri Hassas, Investigation of trajectory and rise velocity of loaded and bare single bubbles in flotation process using video processing technique, Sep. Sci. Technol. 53 (2018) 1–8.

[7] P.M. Ireland, G.J. Jameson, Collision of a rising bubble-particle aggregatewith a gas-liquid interface, Int. J. Miner. Process. 130 (2014) 1–7.

[8] B.A. Wills, T.J. Napier-Munn, Mineral Processing Technology. Seventh

Edition, Elsevier Science & Technology, Oxford, 2006.

[9] A. Shemi, J.S. Hsieh, Electroflotation combined with flotation deinking of flexographic newsprint, Ind. Eng. Chem. Res. 49 (2010) 2380–2387.

[10] J. Rubio, M.L. Souza, R.W. Smith, Overview of flotation as a wastewater treatment technique, Miner. Eng. 15 (2002) 139–155.

[11] D. Mesa, P.R. Brito-Parada, Scale-up in froth flotation: A state-of-the-art review, Sep. Purif. Technol. 210 (2019) 950–962.

[12] A. V. Nguyen, H.J. Schulze, Colloidal Science of Flotation, CRC Press, New York, 2003.

[13] P.G. Smith, L.J. Warren, Entrainment of particles into flotation froths, Miner. Process. Extr. Metall. Rev. 5 (1989) 123–145.

[14] J. Ralston, D. Fornasiero, R. Hayes, Bubble-particle attachment and detachment in flotation, Int. J. Miner. Process. 56 (1999) 133–164.

[15] H.J. Schulze, K.W. Stöckelhuber, A. Wenger, The influence of acting forces on the rupture mechanism of wetting films-nucleation or capillary waves, Colloids Surfaces A Physicochem. Eng. Asp. 192 (2001) 61–72.

[16] G.K.N. Subasinghe, B. Albijanic, Influence of the propagation of three phase contact line on flotation recovery, Miner. Eng. 57 (2014) 43–49.

[17] M. Krasowska, K. Malysa, Wetting films in attachment of the colliding bubble, Adv. Colloid Interface Sci. 134–135 (2007) 138–150.

[18] A. V. Nguyen, J. Ralston, H.J. Schulze, On modelling of bubble-particle attachment probability in flotation, Int. J. Miner. Process. 53 (1998) 225–249.

[19] A.V. Nguyen, H.J. Schulze, J. Ralston, Elementary steps in particle–bubble attachment, Int. J. Miner. Process. 51 (1997) 183–195.

[20] T.W. Cheng, P.N. Holtham, The particle detachment process in flotation, Miner. Eng. 8 (1995) 883–891.

[21] O. Pitois, X. Chateau, Small particle at a fluid interface: Effect of contact angle hysteresis on force and work of detachment, Langmuir. 18 (2002) 9751–9756.

[22] G. Wang, J.B. Joshi, M. Sathe, G.J. Jameson, S. Zhou, G.M. Evans, Bubble detachment from a steel ball in turbulent field: Application to mineral flotation systems, Procedia Eng. 102 (2015) 1046–1055.

[23] G. Wang, S. Zhou, J.B. Joshi, G.J. Jameson, G.M. Evans, An energy model on particle detachment in the turbulent field, Miner. Eng. 69 (2014) 165–169.

[24] H.J. Schulze, Dimensionless number and approximate calculation of the upper particle size of floatability in flotation machines, Int. J. Miner. Process. 9 (1982) 321–328.

[25] A. V. Nguyen, New method and equations for determining attachment tenacity and particle size limit in flotation, Int. J. Miner. Process. 68 (2003) 167–182.

[26] R. Crawford, J. Ralston, The influence of particle size and contact angle in mineral flotation, Int. J. Miner. Process. 23 (1988) 1–24.

[27] C.D.F. Gontijo, D. Fornasiero, J. Ralston, The limits of fine and coarse particle flotation, Can. J. Chem. Eng. 85 (2007) 739–747.

[28] T. Miettinen, J. Ralston, D. Fornasiero, The limits of fine particle flotation, Miner. Eng. 23 (2010) 420–437.

[29] Z. Dai, D. Fornasiero, J. Ralston, Particle-bubble collision models-a review, Adv. Colloid Interface Sci. 85 (2000) 231–256.

[30] P.T.L. Koh, L.K. Smith, The effect of stirring speed and induction time on flotation, Miner. Eng. 24 (2011) 442–448.

[31] R.M. Rahman, S. Ata, G.J. Jameson, The effect of flotation variables on the recovery of different particle size fractions in the froth and the pulp, Int. J. Miner. Process. 106–109 (2012) 70–77.

[32] J.J. Bikerman, Formation and Structure, Springer, Berlin, 1973.

[33] I. Mackay, E. Mendez, I. Molina, A.R. Videla, J.J. Cilliers, P.R. Brito-Parada, Dynamic froth stability of copper flotation tailings, Miner. Eng. 124 (2018) 103–107.

[34] I. Achaye, Effect of particle properties on froth stability, University of Cape Town, 2017.

[35] A. Norori-McCormac, P.R. Brito-Parada, K. Hadler, K. Cole, J.J. Cilliers, The effect of particle size distribution on froth stability in flotation, Sep. Purif. Technol. 184 (2017) 240–247.

[36] X. Qu, L. Wang, A. V. Nguyen, Correlation of air recovery with froth stability and separation efficiency in coal flotation, Miner. Eng. 41 (2013) 25–30.

[37] F. Dehghani, M. Rahimi, B. Rezai, Influece of particle shape on the flotation of magretite, alone and in the presence of quartz particles, J. South. African Inst. Min. Metall. 113 (2013) 905–911.

[38] D.I. Verrelli, W.J. Bruckard, P.T.L. Koh, M.P. Schwarz, B. Follink, Particle shape effects in flotation. Part 1: Microscale experimental observations, Miner.

Eng. 58 (2014) 80–89.

[39] B. Vaziri Hassas, H. Caliskan, O. Guven, F. Karakas, M. Cinar, M.S. Celik, Effect of roughness and shape factor on flotation characteristics of glass beads, Colloids Surfaces A Physicochem. Eng. Asp. 492 (2016) 88–99.

[40] T.T. Chau, A review of techniques for measurement of contact angles and their applicability on mineral surfaces, Miner. Eng. 22 (2009) 213–219.

[41] D. Feng, A. V. Nguyen, Effect of contact angle and contact angle hysteresis on the floatability of spheres at the air-water interface, Adv. Colloid Interface Sci. 248 (2017) 69–84.

[42] S. Muganda, M. Zanin, S.R. Grano, Influence of particle size and contact angle on the flotation of chalcopyrite in a laboratory batch flotation cell, Int. J. Miner. Process. 98 (2011) 150–162.

[43] D. Chipfunhu, M. Zanin, S. Grano, The dependency of the critical contact angle for flotation on particle size - Modelling the limits of fine particle flotation, Miner. Eng. 24 (2011) 50–57.

[44] C.A. Acuña, J.A. Finch, Tracking velocity of multiple bubbles in a swarm, Int. J. Miner. Process. 94 (2010) 147–158.

[45] Y.H. Tan, A.A. Rafiei, A. Elmahdy, J.A. Finch, Bubble size, gas holdup and bubble velocity profile of some alcohols and commercial frothers, Int. J. Miner. Process. 119 (2013) 1–5.

[46] A.M. Elmahdy, J.A. Finch, Effect of frother blends on hydrodynamic properties, Int. J. Miner. Process. 123 (2013) 60–63.

[47] Z. Chen, S. Ata, G.J. Jameson, Behaviour of bubble clusters in a turbulent

flotation cell, Powder Technol. 269 (2015) 337–344.

[48] J. Quinn, Bubble behaviour in frother and inorganic salt solutions, McGill University, 2014.

[49] R. Araya, M. Maldonado, C.O. Gomez, J.A. Finch, Measuring gas dispersion parameters: Selection of sampling points, Miner. Eng. 65 (2014) 172–177.

[50] J.J. Quinn, J.A. Finch, Passive acoustic emission monitoring to detect bubble coalescence in the presence of solid particles, Miner. Eng. 108 (2017) 25–30.

[51] J.P. Tucker, D.A. Deglon, J.P. Franzidis, M.C. Harris, C.T. O'Connor, An evaluation of a direct method of bubble size distribution measurement in a laboratory batch flotation cell, Miner. Eng. 7 (1994) 667–680.

[52] P. Chu, K.E. Waters, J.A. Finch, Break-up in formation of small bubbles: Comparison between low and high frother concentrations, Miner. Eng. 96–97 (2016) 15–19.

[53] M. Firouzi, T. Howes, A. V. Nguyen, A quantitative review of the transition salt concentration for inhibiting bubble coalescence, Adv. Colloid Interface Sci. 222 (2014) 305–318.

[54] J.J. Quinn, J.M. Sovechles, J.A. Finch, K.E. Waters, Critical coalescence concentration of inorganic salt solutions, Miner. Eng. 58 (2014) 1–6.

[55] S. Castro, C. Miranda, P. Toledo, J.S. Laskowski, Effect of frothers on bubble coalescence and foaming in electrolyte solutions and seawater, Int. J. Miner. Process. 124 (2013) 8–14.

[56] S.N. Tan, R.J. Pugh, D. Fornasiero, R. Sedev, J. Ralston, Foaming of polypropylene glycols and glycol/MIBC mixtures, Miner. Eng. 18 (2005) 179–

188.

[57] S. Farrokhpay, The significance of froth stability in mineral flotation – A review, Adv. Colloid Interface Sci. 166 (2011) 1–7.

[58] S. Ata, N. Ahmed, G.J. Jameson, A study of bubble coalescence in flotation froths, Int. J. Miner. Process. 72 (2003) 255–266.

[59] N. Barbian, K. Hadler, E. Ventura-Medina, J.J. Cilliers, The froth stability column: Linking froth stability and flotation performance, Miner. Eng. 18 (2005) 317–324.

[60] B. Wang, Y. Peng, The behaviour of mineral matter in fine coal flotation using saline water, Fuel. 109 (2013) 309–315.

[61] Y. Xing, X. Gui, Y. Cao, Effect of bubble size on bubble-particle attachment and film drainage kinetics – A theoretical study, Powder Technol. 322 (2017) 140–146.

[62] L. Ren, Y. Zhang, W. Qin, S. Bao, P. Wang, C. Yang, Investigation of condition-induced bubble size and distribution in electroflotation using a high-speed camera, 2014.

[63] L. Ren, Y. Zhang, W. Qin, S. Bao, J. Wang, Collision and attachment behavior between fine cassiterite particles and H_2 bubbles, Trans. Nonferrous Met. Soc. China. 24 (2014) 520–527.

[64] W. Qin, L. Ren, P. Wang, C. Yang, Y. Zhang, Electro-flotation and collision-attachment mechanism of fine cassiterite, Trans. Nonferrous Met. Soc. China. 22 (2012) 917–924.

[65] H. Schubert, On the turbulence-controlled microprocesses in flotation machines,

Int. J. Miner. Process. 56 (1999) 257–276.

[66] G. Bournival, R.J. Pugh, S. Ata, Examination of NaCl and MIBC as bubble coalescence inhibitor in relation to froth flotation, Miner. Eng. 25 (2012) 47–53.

[67] P. Conil, G. Morizot, Measurements of selectivity due to coalescence between two mineralized bubbles and characterization of MIBC action on froth flotation, Int. J. Miner. Process. 51 (1997) 197–208.

[68] S. Ata, The detachment of particles from coalescing bubble pairs, J. Colloid Interface Sci. 338 (2009) 558–565.

[69] L. He, F. Lin, X. Li, Z. Xu, H. Sui, Effect of solvent addition on bitumen-air bubble attachment in process water, Chem. Eng. Sci. 137 (2015) 31–39.

[70] S. Ata, Coalescence of bubbles covered by particles, Langmuir. 24 (2008) 6085–6091.

[71] D. Xu, I. Ametov, S.R. Grano, Detachment of coarse particles from oscillating bubbles-The effect of particle contact angle, shape and medium viscosity, Int. J. Miner. Process. 101 (2011) 50–57.

[72] J. Wang, A. V Nguyen, Foam drainage in the presence of solid particles, Soft Matter. 12 (2016) 3004–3012.

[73] A. Dippenaar, The destabilization of froth by solids. I. The mechanism of film rupture, Int. J. Miner. Process. 9 (1982) 1–14.

[74] B.K. Rana, A.K. Das, P.K. Das, Towards the understanding of bubble-bubble interaction upon formation at submerged orifices: A numerical approach, Chem. Eng. Sci. 161 (2017) 316–328.

[75] G. Bournival, L. de Oliveira e Souza, S. Ata, E.J. Wanless, Effect of alcohol frothing agents on the coalescence of bubbles coated with hydrophobized silica particles, Chem. Eng. Sci. 131 (2015) 1–11.

[76] G. Kaptay, Interfacial criteria for stabilization of liquid foams by solid particles, Colloids Surfaces A Physicochem. Eng. Asp. 230 (2003) 67–80.

[77] G. Morris, S.J. Neethling, J.J. Cilliers, Predicting the failure of a thin liquid film loaded with spherical particles, Langmuir. 30 (2014) 995–1003.

[78] G. Morris, Particle stabilised thin films, (2010).

[79] G.D.M. Morris, S.J. Neethling, J.J. Cilliers, The stability of a thin liquid film supported by a double layer of spherical particles, Colloids Surfaces A Physicochem. Eng. Asp. 443 (2014) 44–51.

[80] G.D.M. Morris, S.J. Neethling, J.J. Cilliers, A model for the stability of films stabilized by randomly packed spherical particles, Langmuir. 27 (2011) 11475–11480.

[81] G. Morris, M.R. Pursell, S.J. Neethling, J.J. Cilliers, The effect of particle hydrophobicity, separation distance and packing patterns on the stability of a thin film, J. Colloid Interface Sci. 327 (2008) 138–144.

[82] G. Bournival, S. Ata, S.I. Karakashev, G.J. Jameson, An investigation of bubble coalescence and post-rupture oscillation in non-ionic surfactant solutions using high-speed cinematography, J. Colloid Interface Sci. 414 (2014) 50–58.

[83] S.S. Rao, Mechanical Vibrations, 5th Edition, Pearson Eduction, Hoboken, 2010.

[84] S.J. Corkery, H. Babinsky, W.R. Graham, Quantification of added-mass effects

using particle image velocimetry data for a translating and rotating flat plate, J. Fluid Mech. 870 (2019) 492–518.

[85] G. Bournival, S. Ata, E.J. Wanless, Behavior of Bubble Interfaces Stabilized by Particles of Different Densities, Langmuir. 32 (2016) 6226–6238.

[86] S. Ata, E.S. Davis, D. Dupin, S.P. Armes, E.J. Wanless, Direct observation of ph-induced coalescence of latex-stabilized bubbles using high-speed video imaging, Langmuir. 26 (2010) 7865–7874.

[87] Z.J. Ang, G. Bournival, S. Ata, Influence of frothers on the detachment of galena particles from bubbles, Int. J. Miner. Process. 121 (2013) 59–64.

[88] S. Ata, The role of frother on the detachment of particles from bubbles, Miner. Eng. 24 (2011) 476–478.

[89] S. Zhao, Y. Ding, R. Chen, Q. Liao, X. Zhu, Dynamic behaviors of CO2 bubbles coalescing at two parallel capillary orifices in microalgae suspension, Int. J. Heat Mass Transf. 90 (2015) 1001–1008.

[90] K. Ueno, G. Bournival, E.J. Wanless, S. Nakayama, E.C. Giakoumatos, Y. Nakamura, S. Fujii, Liquid marble and water droplet interactions and stability, Soft Matter. 11 (2015) 7728–7738.

[91] A.J. Morse, E.C. Giakoumatos, S.Y. Tan, G.B. Webber, S.P. Armes, S. Ata, E.J. Wanless, Giant pH-responsive microgel colloidosomes: Preparation, interaction dynamics and stability, Soft Matter. 12 (2015) 1477–1486.

[92] S. Ata, R.J. Pugh, G.J. Jameson, The influence of interfacial ageing and temperature on the coalescence of oil droplets in water, Colloids Surfaces A Physicochem. Eng. Asp. 374 (2011) 96–101.

[93] B. Albijanic, G.K. Nimal Subasinghe, D.J. Bradshaw, A. V. Nguyen, Influence of liberation on bubble-particle attachment time in flotation, Miner. Eng. 74 (2014) 156–162.

[94] D.W. Fuerstenau, R. Jia, The adsorption of alkylpyridinium chlorides and their effect on the interfacial behavior of quartz, Colloids Surfaces A Physicochem. Eng. Asp. 250 (2004) 223–231.

[95] B. Albijanic, O. Ozdemir, A. V. Nguyen, D. Bradshaw, A review of induction and attachment times of wetting thin films between air bubbles and particles and its relevance in the separation of particles by flotation, Adv. Colloid Interface Sci. 159 (2010) 1–21.

[96] G. Gu, Z. Xu, K. Nandakumar, J. Masliyah, Effects of physical environment on induction time of air-bitumen attachment, Int. J. Miner. Process. 69 (2003) 235–250.

[97] D.I. Verrelli, W.J. Bruckard, P.T.L. Koh, M.P. Schwarz, B. Follink, Influence of Particle Shape and Roughness on the Induction Period for Particle – Bubble Attachment, XXVI Int. Miner. Process. Congr. (2012) 5665–5676.

[98] L. Wang, A study of interactions between an air bubble and a solid surface in a liquid, University of Alberta, 2013.

[99] L. Wang, D. Sharp, J. Masliyah, Z. Xu, Measurement of interactions between solid particles, liquid droplets, and/or gas bubbles in a liquid using an integrated thin film drainage apparatus, Langmuir. 29 (2013) 3594–3603.

[100] M. Zhang, G. Wang, G.M. Evans, Flow visualizations around a bubble detaching from a particle in turbulent flows, 92 (2016) 176–188.

[101] G. Wang, D. Feng, A. Nguyen, G.M. Evans, The dynamic contact angle of a bubble with an immersed-in-water particle and its implications for bubble-particle detachment, Int. J. Miner. Process. 151 (2016) 22–32.

[102] J.J. Quinn, M. Maldonado, C.O. Gomez, J.A. Finch, Experimental study on the shape-velocity relationship of an ellipsoidal bubble in inorganic salt solutions, Miner. Eng. 55 (2014) 5–10.

[103] S. Ata, K.Y. Ng, E. Law, M. Lim, Influence of particles on the formation of bubbles from a submerged capillary, Miner. Eng. 66–68 (2014) 47–53.

[104] R. Clift, J.R. Grace, M.E. Weber, Bubbles, Drops, and Particles, Academic Press, New York, 1978.

[105] M.A.R. Talaia, Terminal Velocity of a Bubble Rise in a Liquid Column, Int. J. Phys. Math. Sci. 1 (2007) 220–224.

[106] L. Amaya-Bower, T. Lee, Single bubble rising dynamics for moderate Reynolds number using Lattice Boltzmann Method, Comput. Fluids. 39 (2010) 1191–1207.

[107] I.U. Vakarelski, R. Manica, E.Q. Li, E.S. Basheva, D.Y.C. Chan, S.T. Thoroddsen, Coalescence Dynamics of Mobile and Immobile Fluid Interfaces, Langmuir. 34 (2018) 2096–2108.

[108] M. Martín, F.J. Montes, M.A. Galán, Mass transfer from oscillating bubbles in bubble column reactors, Chem. Eng. J. 151 (2009) 79–88.

[109] L.C. Mutharasu, D. V. Kalaga, M. Sathe, D.E. Turney, D. Griffin, X. Li, M. Kawaji, K. Nandakumar, J.B. Joshi, Experimental study and CFD simulation of the multiphase flow conditions encountered in a Novel Down-flow bubble

column, Chem. Eng. J. 350 (2018) 507–522.

[110] Y. Li, M. Liu, X. Li, Single bubble behavior in gas-liquid-solid mini-fluidized beds, Chem. Eng. J. 286 (2016) 497–507.

[111] F. Gao, Y.Y. Peng, C. Li, W. Cui, Z.H. Yang, G.M. Zeng, Coupled nutrient removal from secondary effluent and algal biomass production in membrane photobioreactor (MPBR): Effect of HRT and long-term operation, Chem. Eng. J. 335 (2018) 169–175.

[112] M. Khalid, E. Johnson, A. Vij, E.J. Bouwer, H.A. Janjua, M.J. Betenbaugh, Anaerobic digestion restricted to phase I for nutrient release and energy production using waste-water grown Chlorella vulgaris, Chem. Eng. J. 352 (2018) 756–764.

[113] B. Lewandowski, M. Fertig, M. Ulbricht, G. Krekel, Relationship between bubble characteristics and hydrodynamic parameters for single bubbles in presence of surface active agents, Chem. Eng. Sci. 199 (2019) 179–198.

[114] X. Yu, Y. Wang, C. Huang, T. Du, Three stages of bubble formation on submerged orifice under constant gas flow rate, J. Phys. Conf. Ser. 656 (2015).

[115] A.A. Kulkarni, J.B. Joshi, Bubble formation and bubble rise velocity in gas-liquid systems: A review, Ind. Eng. Chem. Res. 44 (2005) 5873–5931.

[116] L. Liu, H. Yan, G. Zhao, J. Zhuang, Experimental studies on the terminal velocity of air bubbles in water and glycerol aqueous solution, Exp. Therm. Fluid Sci. 78 (2016) 254–265.

[117] T. Ziegenhein, D. Lucas, Observations on bubble shapes in bubble columns under different flow conditions, Exp. Therm. Fluid Sci. 85 (2017) 248–256.

[118] J. Zawala, Energy balance in viscous liquid containing a bubble: Rise due to buoyancy, Can. J. Chem. Eng. 94 (2016) 586–595.

[119] M. Krzan, K. Lunkenheimer, K. Malysa, Pulsation and bouncing of a bubble prior to rupture and/or foam film formation, Langmuir. 19 (2003) 6586–6589.

[120] W. Kracht, J.A. Finch, Effect of frother on initial bubble shape and velocity, Int. J. Miner. Process. 94 (2010) 115–120.

[121] M. Maldonado, J.J. Quinn, C.O. Gomez, J.A. Finch, An experimental study examining the relationship between bubble shape and rise velocity, Chem. Eng. Sci. 98 (2013) 7–11.

[122] T. Okawa, T. Tanaka, I. Kataoka, M. Mori, Temperature effect on single bubble rise characteristics in stagnant distilled water, Int. J. Heat Mass Transf. 46 (2003) 903–913.

[123] M. Wu, M. Gharib, Experimental studies on the shape and path of small air bubbles rising in clean water, Phys. Fluids. 14 (2002) L49-52.

[124] K. Ellingsen, F. Risso, On the rise of an ellipsoidal bubble in water: oscillatory paths and liquid-induced velocity, J. Fluid Mech. 440 (2001) 235–268.

[125] Y.H. Tan, J.A. Finch, Frother structure-property relationship: Effect of alkyl chain length in alcohols and polyglycol ethers on bubble rise velocity, Miner. Eng. 95 (2016) 14–20.

[126] Y.H. Tan, W. Zhang, J.A. Finch, Frother structure-property relationship: Effect of polyethylene glycols on bubble rise velocity, Miner. Eng. 116 (2018) 56–61.

[127] Y.H. Tan, J.A. Finch, Frother structure-property relationship: Aliphatic alcohols and bubble rise velocity, Miner. Eng. 96–97 (2016) 33–38.

[128] Y.H. Tan, J.A. Finch, Frother structure-property relationship: Effect of hydroxyl position in alcohols on bubble rise velocity, Miner. Eng. 92 (2016) 1–8.

[129] D. Kosior, J. Zawala, Initial degree of detaching bubble adsorption coverage and the kinetics of dynamic adsorption layer formation, Phys. Chem. Chem. Phys. 20 (2018) 2403–2412.

[130] K. Malysa, M. Krasowska, M. Krzan, Influence of surface active substances on bubble motion and collision with various interfaces, Adv. Colloid Interface Sci. 114–115 (2005) 205–225.

[131] H. Dong, X. Wang, L. Liu, X. Zhang, S. Zhang, The rise and deformation of a single bubble in ionic liquids, Chem. Eng. Sci. 65 (2010) 3240–3248.

[132] C. Huang, L. Wang, X. Chen, X. Wei, J. Liang, The rising behaviors of single bubbles in stagnant turpentine and pine resin solutions, Exp. Therm. Fluid Sci. 98 (2018) 170–180.

[133] L. Liu, H. Yan, G. Zhao, Experimental studies on the shape and motion of air bubbles in viscous liquids, Exp. Therm. Fluid Sci. 62 (2015) 109–121.

[134] S. Vafaei, D. Wen, Bubble formation in a quiescent pool of gold nanoparticle suspension, Adv. Colloid Interface Sci. 159 (2010) 72–93.

[135] S. Vafaei, D. Wen, Effect of gold nanoparticles on the dynamics of gas bubbles, Langmuir. 26 (2010) 6902–6907.

[136] J. Zawala, A. Niecikowska, "Bubble-on-demand "generator with precise adsorption time control, Rev. Sci. Instrum. 88 (2017) 095106.

[137] A. Tomiyama, I. Kataoka, I. Zun, T. Sakaguchi, Drag Coefficients of Single

Bubbles under Normal and Micro Gravity Conditions, JSME Int. J. Ser. B. 41 (1998) 472–479.

[138] X. Yan, Y. Jia, L. Wang, Y. Cao, K. Zheng, Y. Jia, Z. Miao, L. Wang, Y. Cao, J. Liu, Drag coefficient fluctuation prediction of a single bubble rising in water, Chem. Eng. J. 316 (2017) 553–562.

[139] M. Karimi, G. Akdogan, Comparison of different drag coefficient correlations in the CFD modelling of a Laboratory-Scale Rushton-Turbine Flotation Tank, in: Ninth Int. Conf. CFD Miner. Process Ind., 2012: pp. 1–7.

[140] L. Schiller, A. Naumann, Über die grundlegenden Berechnungen bei der Schwerkraftaufbereitung, Zeitschrift Des Vereines Dtsch. Ingenieure. 77 (1933) 318–320.

[141] S.H. Park, C. Park, J.Y. Lee, B. Lee, A Simple Parameterization for the Rising Velocity of Bubbles in a Liquid Pool, Nucl. Eng. Technol. 49 (2017) 692–699.

[142] P.C. Duineveld, Bouncing and coalescence of bubble pairs rising at high Reynolds number in pure water or aqueous surfactant solutions, Appl. Sci. Res. 58 (1998) 409–439.

[143] H.-K. Tsao, D.L. Koch, Observations of high Reynolds number bubbles interacting with a rigid wall, Phys. Fluids. 9 (1997) 44.

[144] H.D. Mendelson, The prediction of bubble terminal velocities from wave theory, AIChE J. 13 (1967) 250–253.

[145] X. Yan, Y. Jia, L. Wang, Y. Cao, Drag coefficient fluctuation prediction of a single bubble rising in water, Chem. Eng. J. 316 (2017) 553–562.

[146] X. Yan, K. Zheng, Y. Jia, Z. Miao, L. Wang, Y. Cao, J. Liu, Drag Coefficient

Prediction of a Single Bubble Rising in Liquids, Ind. Eng. Chem. Res. 57 (2018) 5385–5393.

[147] E. Klaseboer, R. Manica, M.H.W. Hendrix, C.D. Ohl, D.Y.C. Chan, A force balance model for the motion, impact, and bounce of bubbles, Phys. Fluids. 26 (2014) 1–12.

[148] S. Aoyama, K. Hayashi, S. Hosokawa, A. Tomiyama, Shapes of single bubbles in infinite stagnant liquids contaminated with surfactant, Exp. Therm. Fluid Sci. 96 (2018) 460–469.

[149] V. Poulichet, V. Garbin, Cooling particle-coated bubbles: Destabilization beyond dissolution arrest, Langmuir. 31 (2015) 12035–12042.

[150] M. Yang, H. Wei, S. Lin, A theoretical study on surfactant adsorption kinetics: Effect of bubble shape on dynamic surface tension, Langmuir. 23 (2007) 12606–12616.

[151] E.Y. Arashiro, N.R. Demarquette, Use of the pendant drop method to measure interfacial tension between molten polymers, Mater. Res. 2 (1999) 23–32.

[152] J. Yang, K. Yu, Y.Y. Zuo, Accuracy of Axisymmetric Drop Shape Analysis in Determining Surface and Interfacial Tensions, Langmuir. 33 (2017) 8914–8923.

[153] Y. Rotenberg, L. Boruvka, A.W. Neumann, Determination of surface tension and contact angle from the shapes of axisymmetric fluid interfaces without use of apex coordinates, J. Colloid Interface Sci. 93 (1983) 169–183.

[154] Y. Li, T. Zhu, Y. Liu, Y. Tian, H. Wang, Effects of surfactant on bubble hydrodynamic behavior under flotation-related conditions in wastewater, Water Sci. Technol. 65 (2012) 1060–1066.

[155] X.Y. Hu, N.A. Adams, An incompressible multi-phase SPH method, J. Comput. Phys. 227 (2007) 264–278.

[156] P. Nair, T. Pöschel, Dynamic capillary phenomena using Incompressible SPH, Chem. Eng. Sci. 176 (2018) 192–204.

[157] Lord Rayleigh, On the capillary phenomena of jets, Proc. R. Soc. London. 29 (1879) 71–97.

[158] X.Y. Hu, N.A. Adams, A multi-phase SPH method for macroscopic and mesoscopic flows, J. Comput. Phys. 213 (2006) 844–861.

[159] D.J. Barker, The application of smoothed particle hydrodynamics to the simulation of multiphase flows through packed beds, Imperial College London, 2015.

[160] G. Liger-Belair, R. Marchal, B. Robillard, T. Dambrouck, A. Maujean, M. Vignes-Adler, P. Jeandet, On the velocity of expanding spherical gas bubbles rising in line in supersaturated hydroalcoholic solutions: application to bubble trains in carbonated beverages, Langmuir. 16 (2000) 1889–1895.

[161] J. Meng, E. Tabosa, W. Xie, K. Runge, D. Bradshaw, E. Manlapig, A review of turbulence measurement techniques for flotation, Miner. Eng. 95 (2016) 79–95.

[162] R. Manica, E. Klaseboer, D.Y.C. Chan, Force Balance Model for Bubble Rise, Impact, and Bounce from Solid Surfaces, Langmuir. 31 (2015) 6763–6772.

[163] E. Klaseboer, J.P. Chevaillier, A. Mate, O. Masbernat, C. Gourdon, A. Maté, O. Masbernat, C. Gourdon, Model and experiments of a drop impinging on an immersed wall, Phys. Fluids. 13 (2001) 45–57.

[164] G.I. Kelbaliyev, Drag coefficients of variously shaped solid particles, drops, and

bubbles, Theor. Found. Chem. Eng. 45 (2011) 248–266.

[165] J.M. Coulson, J.F. Richardson, Chemical engineering, Bath Press, Bath, 2002.

[166] M. Hemmati Chegeni, M. Abdollahy, M.R. Khalesi, Bubble loading measurement in a continuous flotation column, Miner. Eng. 85 (2016) 49–54.

[167] P. Wang, W. Qin, L. Ren, Q. Wei, R. Liu, C. Yang, S. Zhong, Solution chemistry and utilization of alkyl hydroxamic acid in flotation of fine cassiterite, Trans. Nonferrous Met. Soc. China. 23 (2013) 1789–1796.

[168] P. Blake, J. Ralston, Particle size, Surface Coverage and Flotation Response, Colloids and Surfaces. 16 (1985) 41–53.

[169] D.I. Verrelli, B. Albijanic, A comparison of methods for measuring the induction time for bubble-particle attachment, Miner. Eng. 80 (2015) 8–13.

[170] P. Chu, M. Mirnezami, J.A. Finch, Quantifying particle pick up at a pendant bubble: A study of non-hydrophobic particle–bubble interaction, Miner. Eng. 55 (2014) 162–164.

[171] F. Omota, A.C. Dimian, A. Bliek, Adhesion of solid particles to gas bubbles. Part 2: Experimental, Chem. Eng. Sci. 61 (2006) 835–844.

[172] Y. Hung, Y. Chang, M. Wang, S. Lin, A simple method for measuring the superhydrophobic contact angle with high accuracy, Rev. Sci. Instrum. 81 (2010) 065105.

[173] B. McFadzean, D.G. Castelyn, C.T. O'Connor, The effect of mixed thiol collectors on the flotation of galena, Miner. Eng. 36–38 (2012) 211–218.

[174] B. McFadzean, C.T. O'Connor, A thermochemical study of thiol collector

surface reactions on galena, Miner. Eng. 78 (2015) 83–88.

[175] J. Taguta, C.T. O'Connor, B. McFadzean, The effect of the alkyl chain length and ligand type of thiol collectors on the heat of adsorption and floatability of sulphide minerals, Miner. Eng. 110 (2017) 145–152.

Appendices

Appendix A Influence of TTAB concentration on the rising behavior of particle-laden bubbles

The influence of TTAB concentration on the rising behavior of particle-laden bubbles has been studied. These bubbles were initially fully coated when they were attached on the capillary. The finest particles, with d_{50}=39 μm (d_{90}=64 μm) were used. The aspect ratio and velocity change with time are shown in Figure A.1 and Figure A.2, respectively. As can be seen, both the aspect ratio and the velocity have minor changes with the increase of TTAB concentration over the first 80 ms.

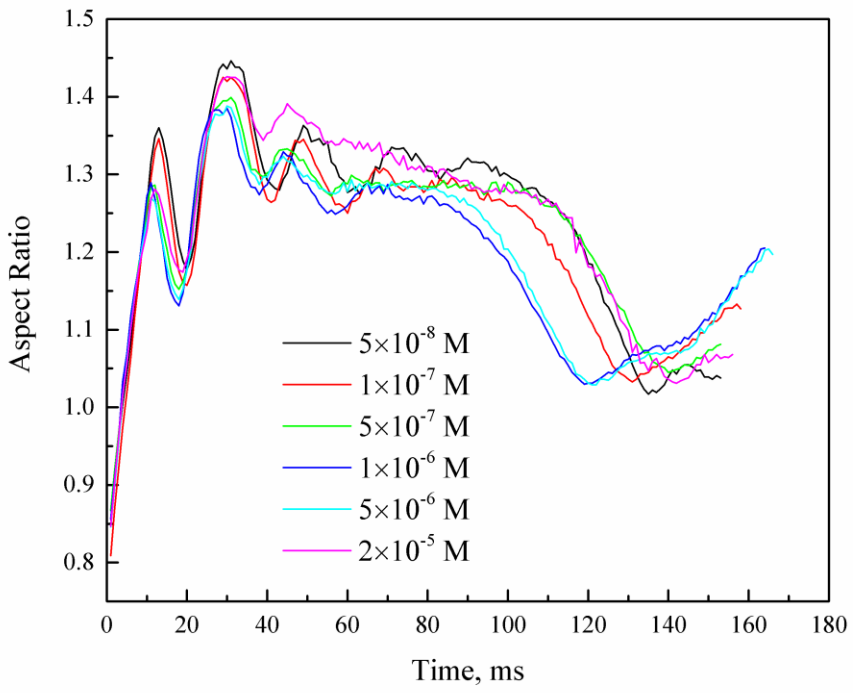

Figure A.1. The aspect ratio change of coated bubbles with different concentrations of TTAB.

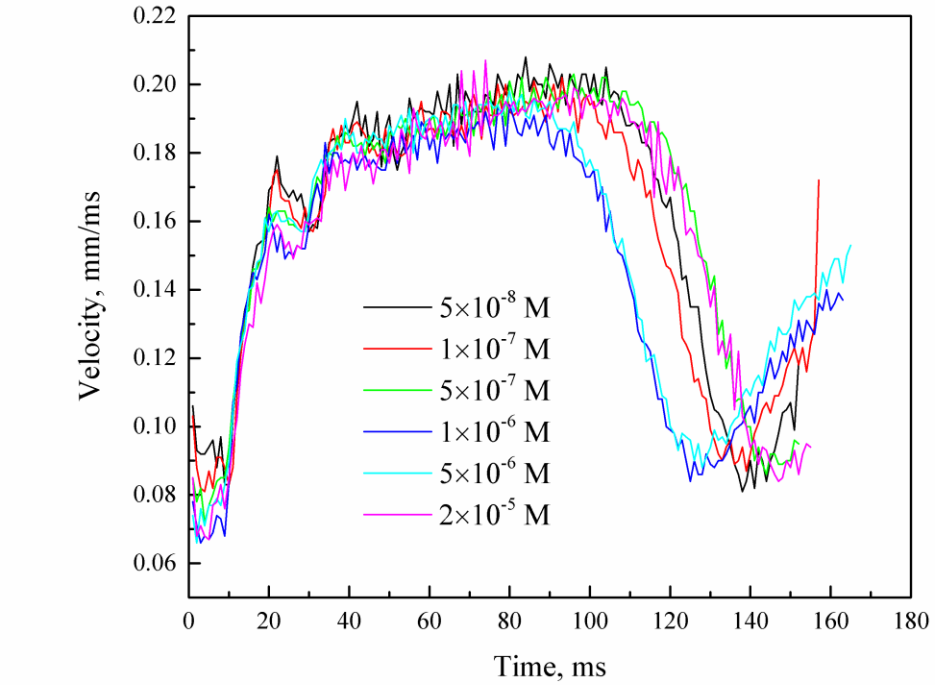

Figure A.2. The velocity change of coated bubbles with different concentrations of TTAB.

Appendix B Evaluating the performance of chalcopyrite collectors using the sessile drop method on individual bubbles

This appendix deals with the Image processing method based on the sessile drop fitting model to evaluate collector performance on individual bubbles. The collectors were provided by BASF, and the particles used were pure chalcopyrite particles. This appendix will be submitted for publication as a technical note.

ABSTRACT:

Particle attachment and detachment in froth flotation are complex processes and their measurement presents many challenges. Of particular interest is to study the effect that collectors have at the bubble-particle scale, in order to assess the strength

or collecting ability of these reagents. However, relevant studies of the effects of collectors on particle attachment at the aforementioned scale are scarce. In this work, we propose a methodology to characterize the performance of collectors that involves studying the attachment of particles to a capillary-pinned bubble. An image processing technique, based on the sessile drop method, was developed to quantify bubble surface coverage, which is then used to determine particle attachment kinetics. The methodology has been used to assess the collecting ability of three different collectors for chalcopyrite. Interestingly, contact angle measurements, typically used to obtain an indication of the collectors' ability, showed similar results for both the best performing collector and the second best performing one. This indicates that the methodology suggested here can be used as a simple way of gaining additional information not currently available from typical collector performance tests.

Graphic abstract:

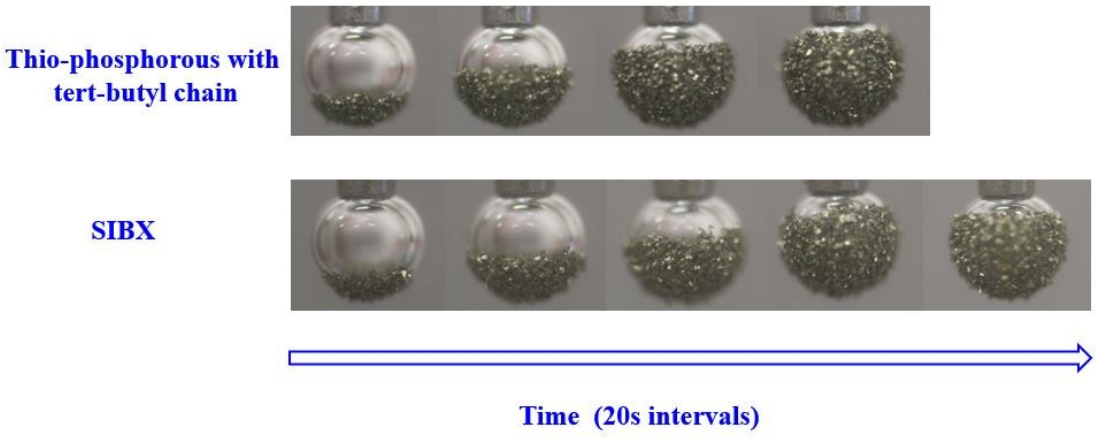

Keywords:

Flotation; Thio-phosphorous collectors; Sulfide mineral; Image analysis; Sessile drop method; Particle attachment; Contact angle.

1. Introduction

Collectors play a key role in froth flotation and evaluating its performance is thus of great importance. To characterize collector performance, a significant amount of approaches have been proposed: at the micro-flotation, mineral particles are collected and its recovery can be analyzed and correlated to collector performance [167]. However, it takes time for the particles to be dried to yield the results and substantial errors are caused for sulfide mineral particles which are easily oxidized. Collectors are usually added to render mineral particles more hydrophobic, and these particles are easily captured by bubbles. Contact angle provides a measurement for mineral hydrophobicity [40,168]. However, this measurement is based on a system at equilibrium that cannot reflect the dynamic environment. Induction time involves a bubble interact with one [99] or several particles [169], which represents a dynamic flotation system. The induction time is reduced when collectors are adsorbed on the particle surface. However, the individual particle interactions with a bubble is not an accurate representation of the real system as particles might influence each other when they are attached on bubbles.

Only a few studies at the bubble-particle scale include a turbulent environment, quantifying particle coverage on a capillary pinned bubble in an environment close to real flotation. Bubble/particle attachment angle (BPA) [170] has been proposed to reflect the extent of particle coverage on a bubble. The mass of attached particles was found to be linearly correlated with the angle formed by the particle bed on the bubble, showing that the BPA can substitute for direct weight. Similarly, the coverage angle [171], being the angle formed by the center of a particle, the center of a spherical bubble, and the lowest pole of the bubble, has also been put forward to characterize the particle coverage on a capillary-pinned bubble. It is shown that a higher particle

coverage is yielded with a higher angle with both aforementioned methods used. However, both these methods are only applicable when the particle coverage boundary is straight. Ata (2009) has developed a method to quantify the particles covered on a capillary pinned bubble. The bubble was assumed as half-sphere and half ellipsoid, the covered boundary of particles on bubbles was also considered so as to determine the bubble surface area covered by particles. However, this method is only based on geometric calculation. The pendant drop method and sessile drop method have been developed for the measurement of interfacial properties such as surface tension [151,152] and contact angle [171,172]. However, they have not been used in the calculation of the bubble's surface area, let alone the particle coverage on the bubble surface. Overall, none of these methodologies has combined the calculation of the particle coverage on capillary pinned bubbles with the property of the air-water interface.

In this work, the attachment of particles to bubbles under different reagent schemes was assessed through experiments involving bubbles generated in a submerged capillary. Individual bubbles of controlled size were coated with chalcopyrite particles, while image processing techniques based on the sessile drop fitting model were developed to quantify the degree of attachment at different agitation times. In terms of collectors, thiol collectors have been reported to produce a high recovery for sulfide minerals [173,174]. It has been reported that diethyl di-thiophosphate barely interacts with any of the sulfide minerals while it produces unexpectedly high chalcopyrite recoveries [175]. The experimental methods described above were used to evaluate the performance of two thio-phosphorous based sulfide mineral collectors against a commercially available alternative (SIBX). Contact angle measurements were also

performed to evaluate collector performance. It is proposed that this technique can serve as a simple yet precise way to evaluate collector performance.

2. Experimental section

This section describes the experimental methodology employed in this work. The data generated, their implications and the reasons for using these methods are discussed in detail.

2.1. Materials

For the particle attachment tests, samples of chalcopyrite were ground and screened to a size of -125μm+75μm, a typical particle size for froth flotation. Three collectors including SIBX, thio-phosphorous collectors with tert-butyl and nonyl chains were supplied by BASF. Both the latter two collectors were mixed (on a 1:1 ratio by weight) with 2-Ethylhexan-1-ol. All experiments were performed at a temperature of 19 °C under natural pH conditions.

2.2. Experimental setup

A schematic diagram of the setup is shown in Figure B.1. A stainless steel capillary (18 gauge needle), mounted on the syringe, was placed in a transparent rectangular chamber (5 ×5 ×12.5 cm) and bubbles were generated from the tip of the capillary. The syringe was connected to another syringe driven by a programmable micro-syringe pump, achieving a repeatable bubble generation by precisely controlling the air injection into the capillary. All the setup was placed on a vibration-free table to minimize disturbance. The bubbles prior and after they were coated with particles were recorded using a Canon EOS 600D camera at a resolution of 1.6 μm/pixel, with LED back-lighting for illumination.

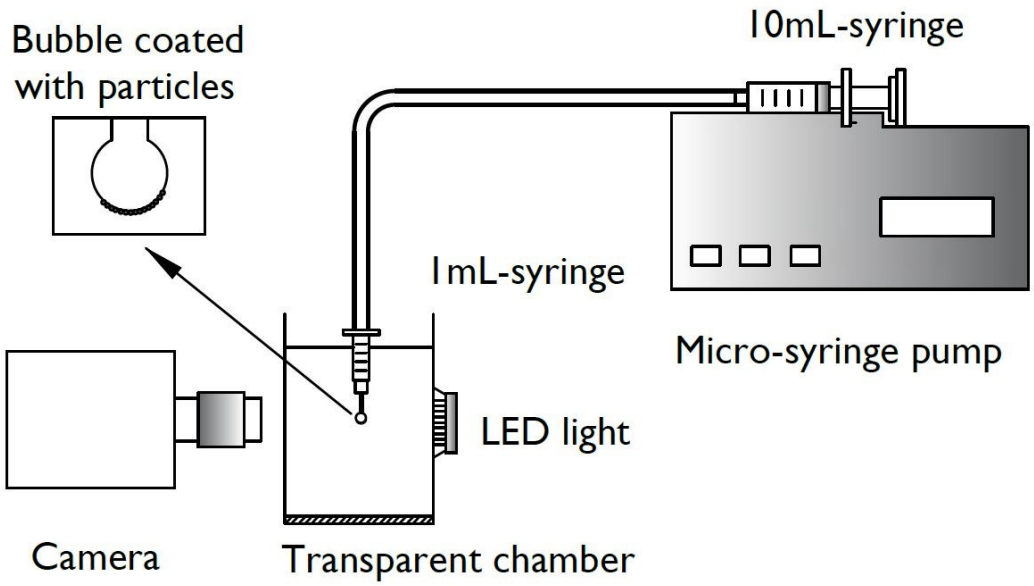

Figure B.1. Schematic diagram of the experimental setup to investigate the attachment of chalcopyrite particles to a capillary-generated bubble.

3. Methodology

3.1. Experiment procedure

One gram of chalcopyrite particles was added to the transparent chamber, which was filled with 250 mL deionized water. The collector was added to achieve a concentration of 0.08 mg/L and the solution was then mixed for 15 min using a magnetic stirrer. After the particles in suspension settled, a bubble of approximately 2.4 mm in diameter was generated at the tip of the capillary, and an image of the uncoated bubble was captured. The system was agitated again to promote particle attachment at a magnetic stirrer speed of 350 rpm for consecutive short periods of time. After the particles settled, an image of the particle-laden bubble was captured. The surface area of the bubbles and surface coverage of particles were analyzed using MATLAB. The tip of the capillary was also photographed to use it as a reference dimension during image processing. Each experiment was carried out in triplicate.

3.2. Image processing method

The detailed information of Image processing method can be seen in Chapter 4 Section 4.2.

3.3. Contact angle test

Contact angle tests were conducted using a Ramé-hart Model 500 Advanced Goniometer. Chalcopyrite sample plates (39 mm in diameter) were polished for 30 min with a paste of 8 μm silica particles, to obtain a fresh surface. The polished chalcopyrite plate was then washed with DI water, prior to ultrasonic cleaning in a pure ethanol solution for 5 min, to remove any debris or organic contamination. The plate was conditioned for 15 min in a collector solution with the same concentration as the attachment tests. Finally, it was washed with DI water and then excessive water was removed using filter papers. After polishing and cleaning, the contact angle tests were performed immediately. To guarantee the accuracy of the measurements, ten points on the plate surface were chosen randomly to conduct contact angle tests for each collector.

4. Results and discussion

4.1. Contact angle tests for chalcopyrite conditioned with different collectors

The attachment of particles to bubbles is influenced by the contact angle of mineral particles. The contact angles of chalcopyrite plates after being conditioned with different collectors are tested and shown in Table B.1. As can be seen, the chalcopyrite plates conditioned with SIBX and thio-phosphorous with tert-butyl chain showed a similar contact angle (114°), higher than the one conditioned with thio-phosphorous with nonyl chain (that yielded a contact angle of 94.4°).

Table B.1. Results from the contact angle tests of chalcopyrite conditioned with different collectors (95% confidence interval included).

Collector	SIBX	Thio-phosphorous with tert-butyl chain	Thio-phosphorous with nonyl chain
Contact angle (°)	114.0±3.0	114.3±1.7	94.4±3.9
Image	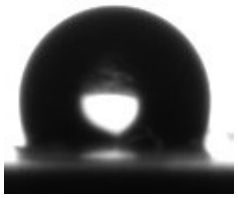	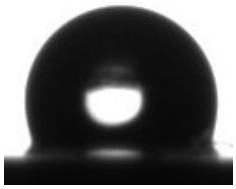	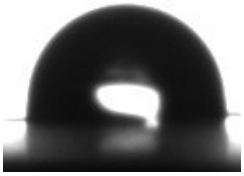

4.2. Surface coverage as a function of time in the chalcopyrite attachment experiments.

The rate at which particles attach to bubbles is a key parameter in flotation kinetics and is strongly influenced, among other variables, by the collector used. For the attachment experiments in this work at the bubble-particle scale, attachment speed can be measured in terms of the surface coverage of particles as a function of time, the results of which are shown in Figure B.2. Collector thio-phosphorous with tert-butyl chain exhibited a high collecting ability, rapidly reaching a high surface coverage value and performing better than SIBX and thio-phosphorous with nonyl chain. Thio-phosphorous with tert-butyl chain resulted in 92% surface coverage after 160 s, while within the same time period, only 71.6% and 59.5% surface coverage were obtained from particles conditioned with SIBX and thio-phosphorous with nonyl chain,

respectively. It should be noted that at very early times, i.e. 20 s, the results for thio-phosphorous with nonyl chain and SIBX were similar. Error bars show the 95% confidence interval, estimated using the three repeats performed for each experiment.

Comparing the contact angle tests, the attachment tests would add more information that cannot be obtained from contact angle tests alone. This technique can provide a convenient way to characterize the performance of collectors for a dynamic flotation system.

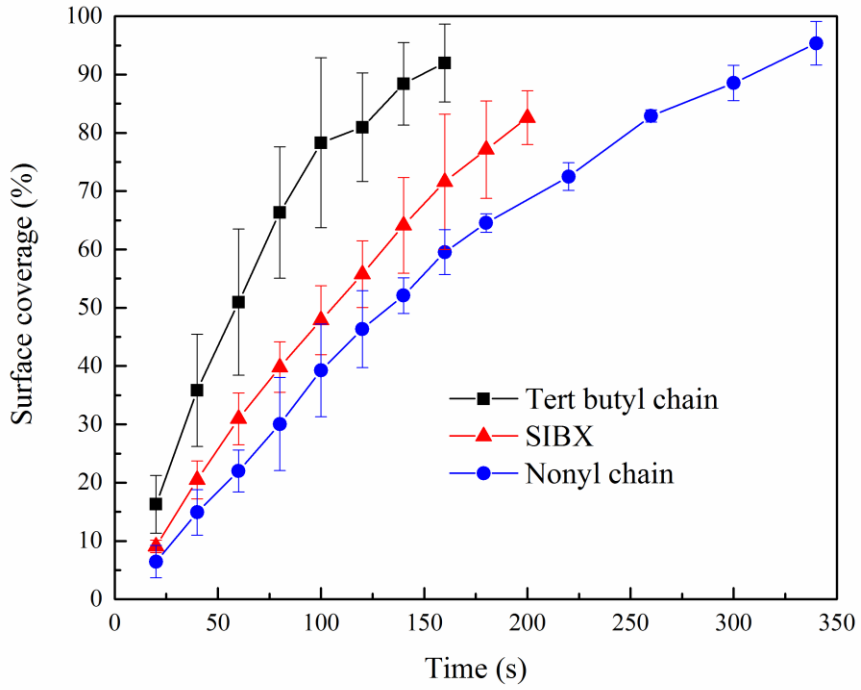

Figure B.2. Surface coverage as a function of time in the chalcopyrite attachment experiments, using SIBX and two novel thio-phosphorous based collectors with tert-butyl and nonyl chains. The data are shown with 95% confidence interval.

5. Conclusions

An image analysis technique to determine the surface area of bubbles covered by particles was developed as part of this work and used to study the rate at which

chalcopyrite particles attached to a bubble in a capillary. The surface coverage at different agitation times is proposed as a proxy for collector strength that can be useful to understand phenomena at the bubble-particle scale. This method was then used to assess three different collectors, including two thio-phosphorous based formulations.

The attachment results showed that the thio-phosphorous collector with tert-butyl chain promoted a more rapid rate of attachment of chalcopyrite particles to the bubble than the one with nonyl chain. This was in line with a higher contact angle observed for the former. Interestingly, the contact angle for SIBX was similar to that of the thio-phosphorous collector with tert-butyl chain despite the latter yielding a higher rate of attachment. This suggests that the kinetics of attachment play an important role in characterizing and comparing collectors, providing information that would not be obtained from contact angle tests alone. The technique presented in this work can thus be used to provide additional information to assess collector performance.

Acknowledgements

The authors would like to thank BASF for providing the collectors and chalcopyrite samples in this work.

Appendix C List of Publications

Peipei Wang, Jan J. Cilliers, Stephen J. Neethling and Pablo R. Brito-Parada. The behavior of rising bubbles covered by particles. Chemical Engineering Journal, 2019, 365:111-120.

Peipei Wang, Jan J. Cilliers, Stephen J. Neethling and Pablo R. Brito-Parada. Effect of particle size on the rising behavior of particle-laden bubbles. Langmuir, 2019, 35 (10), 3680-3687.

Outline

Highlights
Abstract
Graphical abstract
Keywords
1. Introduction
2. Experimental
3. Results and discussion
4. Conclusions
Acknowledgments
Appendix A. Supplementary data
References

Show full outline

Figures (17)

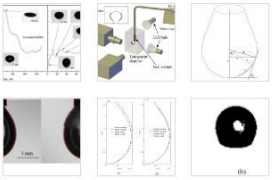

ELSEVIER

Chemical Engineering Journal
Volume 365, 1 June 2019, Pages 111-120

The behavior of rising bubbles covered by particles

Peipei Wang, Jan J. Cilliers, Stephen J. Neethling, Pablo R. Brito-Parada

Show more

https://doi.org/10.1016/j.cej.2019.02.005

Highlights

- The velocity and aspect ratio of rising particle-laden bubbles was investigated.
- The buoyancy force and drag force exerted on the bubbles and the effect of particles were calculated.
- Particles attached strongly dampen the oscillations observed in bubble velocity and aspect ratio.
- A drag modification factor was identified to quantify the drag influence of particles on bubble velocity

LANGMUIR

Search | Citatio

Enter search text / DO

Langmuir | All

Subsc

Browse the Journal | Articles ASAP | Current Issue | Submission & Review | Open Access | About the Journal

Article

Previous A

Effect of Particle Size on the Rising Behavior of Particle-Laden Bubbles

Peipei Wang*, Jan J. Cilliers, Stephen J. Neethling, and Pablo R. Brito-Parada*
Advanced Mineral Processing Research Group, Department of Earth Science and Engineering, Imperial College London, London SW7 2AZ, U.K.

Langmuir, **2019**, *35* (10), pp 3680–3687
DOI: 10.1021/acs.langmuir.8b04112
Publication Date (Web): February 20, 2019

*E-mail: pw415@imperial.ac.uk (P.W.)., *E-mail: p.brito-parada@imperial.ac.uk (P.R.B.P.).

Cite this: *Langmuir* 2019, 35, 10, 3680-3687

RIS Citation | GO

Abstract